Investigation of the Heat and Wear of Aircraft Landing Gear Tyres

Abdurrhman Atig Alroqi

A Thesis Submitted in Fulfillment of the

Requirements for the Degree of

Doctor of Philosophy

Department of Engineering and Design

May 2017

ABSTRACT

In aircraft, the main landing gear wheels skid on the runway at the moment of touchdown because of high slip. A slipping tyre generates enough heat to melt its rubber. Melted rubber is easily eroded by the friction force between the tyre and runway; and part of eroded rubber stays on the runway, and other is burnt off as smoke. Since the early days of airplane use, a number of ideas have been patented to improve tyre safety and decrease the substantial wear and smoke during every landing by spinning the gear wheels before touchdown. In this thesis, there are three parts of research work.

First part is to find the effectiveness of the technique of pre-spinning the wheel to reduce the tyre tread heat and wear, and then choosing the initial wheel rotation speed that prevent the tread rubber from melting temperature. For achieving this, a coupled structural – thermal transient analysis in ANSYS has been used to model a single wheel main landing gear as a mass-spring system. This model has been chosen to analyze the wheel's dynamic behaviour and tyre tread temperature and wear during the short period from static to a matching free-rolling velocity in which the wheel is forced to accelerate by the friction between the tyre and ground. The tyre contact surface temperature and wear have been calculated for both the initially static and pre-spun wheels in order to compare the temperature and wear levels for different initial rotation speeds.

In the second part, the required torque to spin the aircraft wheel to the required angular speed at approach speed has been calculated using ANSYS CFX, which is used to determine the wheel aerodynamic forces developed by simulation of fluid flows in a virtual environment. In the last part, several types of wind turbines have been simulated

using ANSYS CFX in order to optimize with regard to the geometry, target rotation speed, and required acceleration.

Acknowledgements

I would like to express my special appreciation and thanks to my supervisor Dr. Weiji William Wang for his continuous support of my PhD study, for his patience, motivation, and immense knowledge. Dr Wang was always there to steer me onto the right path and to answer my many questions. He was a source of inspiration that gave me the courage to continue with my thesis. I would also like to extend my thanks to Dr Zhiyin Yang who also gave me valuable advice and support.

My gratitude also goes to my family for their patience and understanding during my PhD. Thanks go to my wife, my daughters and my sons.

I would also like to dedicate this study to the memory of my parents.

Table of Contents

List of Tables

List of Figures

Nomenclature

A_f = wheel frontal area (m^2)

A_{side} = two side areas of the wheel (m^2)

A_s = turbine swept area (m^2)

c, c_t = shock absorber and tyre damping coefficients respectively (Ns/m)

c_v = material specific heat ($\frac{J}{Kg\ \mathrm{K}}$)

$C_{1,2,3,4}$ = runway surface types friction constants

C_{Dr} = rotational drag coefficient

C_{Dt} = translational drag coefficient

C_r = bearing friction coefficient

C_p = turbine power coefficient

C_t = turbine's mechanical torque coefficient

e = turbine overlap ratio

F_{ad}, F_{rt} = advance and return the drag forces of the turbine blade respectively (N)

F_D = total drag force (N)

F_{Dr} = rotational drag force (N)

F_{Dt} = translational drag force (N)

F_L = lift force (N)

F_R = reaction force reacted at tyre contact patch (N)

F_{req} = required force to spin the wheel (N)

F_{rol} = shaft rolling resistance (N)

F_{ts} = total force applied to the wheel shaft (N)

F_x = longitudinal friction force reacted on tyre contact patch (N)

F_y = downward force reacted by the landing gear structure (N)

G = vortex strength (m^2/sec)

h = turbine height (m)

H = hardness of the softer material (N/m^2)

I = wheel's moment of inertia ($kg\ m^2$)

k = thermal conductivity ($\frac{W}{m\,\mathrm{K}}$), k_t for tyre and k_r for runway

k, k_t = landing gear and tyre linear stiffness respectively (N/m)

K_e = Archard's abrasion factor

m, m_w = weight box and wheel mass respectively (kg)

P_w , P_t = power of the wind and turbine respectively (watt)

q = heat flux generated by friction power ($\frac{W}{m^2}$)

R, r_e = free and effective wheel radiuses respectively (m)

r_{rim} = mean radius of the rim (m)

R_b = turbine's blade radius (m)

R_t = turbine radius (m)

S_D = skid distance (m)

T = tyre tread temperature (˚C)

T_{net} = turbine net torque that causes the wheel rotation (N.m)

T_{req} = required torque to spin the wheel (N.m)

T_t = mechanical torque produced by the turbine (N.m)

TSR = turbine tip speed ratio

U = wind speed (m/sec)

v = aircraft's horizontal ground speed (m/s)

V = total volume of wear amount (m^3)

v_r = relative wheel speed at approach (m/sec)

v_s = wheel skidding speed (m/s)

W_m = wear amount (kg)

$y,\ \delta$ = lumped mass vertical displacement and tyre deflection respectively (m)

$\dot{y},\ \dot{\delta}$ = vehicle vertical velocity and tyre deflection rates respectively (m/s)

$\ddot{\delta},\ \ddot{y}$ = tyre deflection and vehicle vertical accelerations respectively (m/s^2)

α = thermal diffusivity ($\frac{m^2}{s}$), α_t for tyre and α_r for runway

λ = wheel slip ratio

$\rho,\ \rho_A$ = material and air densities respectively ($\frac{Kg}{m^3}$)

$\omega,\ \omega_i$ = wheel angular velocities after and prior to touchdown respectively (rad/sec)

ω_t = turbine rotational speed (rad/sec)

$\dot{\omega}$ = wheel's acceleration (rad/s^2)

μ = friction coefficient

Chapter 1

1. Introduction

1.1. Research Motivation

The impact an aircraft has on its tyres when it lands has been problematic practically since the invention of the airplane. The tyres frequently smoke as rubber burns off and tyre material is worn away immediately after touchdown.

The aircraft landing smoke can be described by the following chain of events during a typical landing: firstly, the landing speed of heavy aircraft is high, this leads to a great difference between the tangential velocity of the tyre radius and horizontal landing speed at touchdown. The tangent velocity of the tyre is forced to accelerate to overcome the inertia of the wheel/tyre assembly to match the aircraft ground speed. The runway surface can only provide limited friction between the tyre and ground for the acceleration from static. Therefore, slip is inevitable. The slip normally takes place within a second and its distance ranges from several to dozens of meters [1].

The heat flux generated by the slipping tyre at touchdown is enough to melt a thin layer of tyre tread rubber [2]. However, the major part of the heat flux generated occurs when the wheel is fully skidding [3]. The tyre tread temperature rises immediately during the tyre skidding phase within 0.1 seconds to exceed the melting (critical) temperature of tread rubber [2]. Most of the tyre tread material is natural rubber [4], and its critical temperature is about 200 ˚C [2]. Some experiments have shown that the rubber deposited

on the concrete is at this temperature level [5]. At the critical temperature, the bond linkages in the tread rubber material break and then wear occurs easily by abrasion force [2]. About third of the eroded rubber particles burn off under the skidding wheel and evaporate in the form of smoke, while the rest of the eroded rubber remains on the runway [6]. **Therefore, the tyre will not smoke if its temperature remains below the critical rubber temperature level, even if wear occurs, because the rubber particles will not burn**. However, the rubber's contact temperature is a function of the force of friction and the skidding speed, and there is no way to avoid a high force of friction [7]. Therefore, a reduction in the skidding speed in order to avoid a high slip ratio can be achieved by pre-spinning the wheels. This will allow for the avoidance of a high tread temperature and wear, a reduction in environmental pollution and an increase in the number of tyre cycles, which is about 300 cycles (take-offs and landings) [8] for heavy aircraft.

1.2 The Aim of the Project

Inventors of various patents have suggested that it is possible to spin the rear wheels before touchdown to avoid landing smoke [9-28].

The first requirement is to find the effectiveness of the technique of pre-spinning the wheel to reduce the tyre heat, wear, and thus smoke. For this, most of the inventors have suggested using wind turbines. The wind energy generated by an approaching aircraft is at a high enough speed to be used by wind turbines to spin wheels. Most of the patent's inventors [9-10, 13-28] have preferred the use of wind energy as it is already available, while using an electric motor is more complex, heavier than wind turbines and requires

more maintenance. Moreover, the wind turbines are relatively easy to construct. However, the wind turbine has limited efficiency, and to use it for aircraft, it should be small enough to fit in the aircraft undercarriage. It also is important to avoid extra weight or have any aerodynamic effects. Therefore, it is necessary to know the minimum level at which the wheel must be pre-spun to avoid the rubber reaching its critical temperature; as fully pre-spinning the wheel requires large wind turbines. Once the pre-rotation is known, wind turbines can be designed and tested virtually against different wind speeds.

1.2.1 The Novelty of the Project

Some authors have used numerical simulation to determine tyre heat and wear under different conditions: skidding, cornering, and free rolling.

Rosu et al. (2016) [29] developed a 3D finite element model for aircraft tyres in rolling and skidding conditions to predict the tyre tread temperature at the contact zone. Also, they found the temperature rise of fully skidding tyres by simulating a sliding block of rubber under a constant vertical load. The second simulation is similar to what has been done experimentally by Linke et al. (2014) [30]. The results show a strong link between heat and wear.

Lin and Hwang (2004) [31] produced a numerical model to investigate the temperature distribution in a smooth tyre operating under different speeds and a constant vertical load. The model results were approximately similar to the results obtained by McAllen et al. (1996) [32] which used a finite element method to compute the temperature rise of free rolling aircraft tyres.

More literature about tyre and wear is presented in Chapter 2. The available literature shows that researchers have investigated tyre temperature or wear for a fully skidding wheel or a skidding wheel at constant speed separately. Moreover, most of the researchers used a constant vertical load on the tyre.

In this thesis, the novelty is the following:

1. The wheel behaviour (fully skidding, spin-up and rolling) is covered in one simulation, which means that the tyre heat and wear build up, instead of every condition being simulated separately.
2. The aircraft landing simulations include the horizontal and vertical landing speeds. The vertical velocity of the aircraft body (sink rate) is considered by pointing the landing gear, with a space between the wheel and runway at the beginning of the simulation. The wheel is connected with a shock absorber and there is a weight box (aircraft body). This is useful to find the tyre impact, deflection, spin-up, and free rolling, which will give changeable reaction and friction forces versus time, as the friction force is the main factor in tyre heat and wear.
3. The effect of pre-spinning the wheel on the tyre heat and wear is investigated.
4. The tyre wear is calculated with respect to the variable rubber hardness according to the tyre tread temperature for more accuracy. This is because increasing the tyre tread temperature decreases the rubber hardness and thus increases the tyre wear [2].

Moreover, different types of wind turbine have been connected to the aircraft wheel and simulated against a high wind speed. This is to check the ability of wind turbines to spin aircraft wheels at approach.

1.2.2 Case Study and Project Procedure

In this thesis, a Boeing 747-400 single main landing gear wheel is modelled using ANSYS. This wheel is simulated in two main conditions; on the ground at touchdown, and at approach. For this, it is important to know the typical landing procedure to get the correct aircraft speed at approach and touchdown.

The technique used in a typical aircraft approach is to maintain a constant speed until about 15 m above the runway threshold and then flare to reduce the sink rate (downward vertical speed) for a smooth landing [33]. This manoeuvre increases the aircraft pitch angle to induce drag, which will reduce the landing speed by approximately 10 knots (5.14 m/s) to lessen the landing distance [34]. Figure 1.1 shows the aircraft landing process; approach, flare, full skidding wheels, spun-up wheels, deceleration, and the research areas.

The first model simulates the skidding phase after the landing impact. In this model, a coupled structural – thermal transient analysis in ANSYS has been used to model a single wheel main landing gear as a mass-spring system. This model provides results for tyre tread temperature and wear, plus skidding distance and time for a typical aircraft landing, and for wheels already rotated before touchdown, to find how much reduction of tyre heat and wear can be achieved by pre-spinning the wheel, as suggested by many patent inventors, to avoid landing smoke.

Based on the first model's results, the wheel is simulated against different wind speeds in the approach phase using ANSYS Workbench CFX. The wheel is accelerated from zero to the target rotation speed to find how much torque is required to spin it during the aircraft approach. Once the torque is known, the wind turbines are designed and simulated using ANSYS workbench CFX in order to optimize performance according to the geometry, achieved wheel angular velocity, and acceleration.

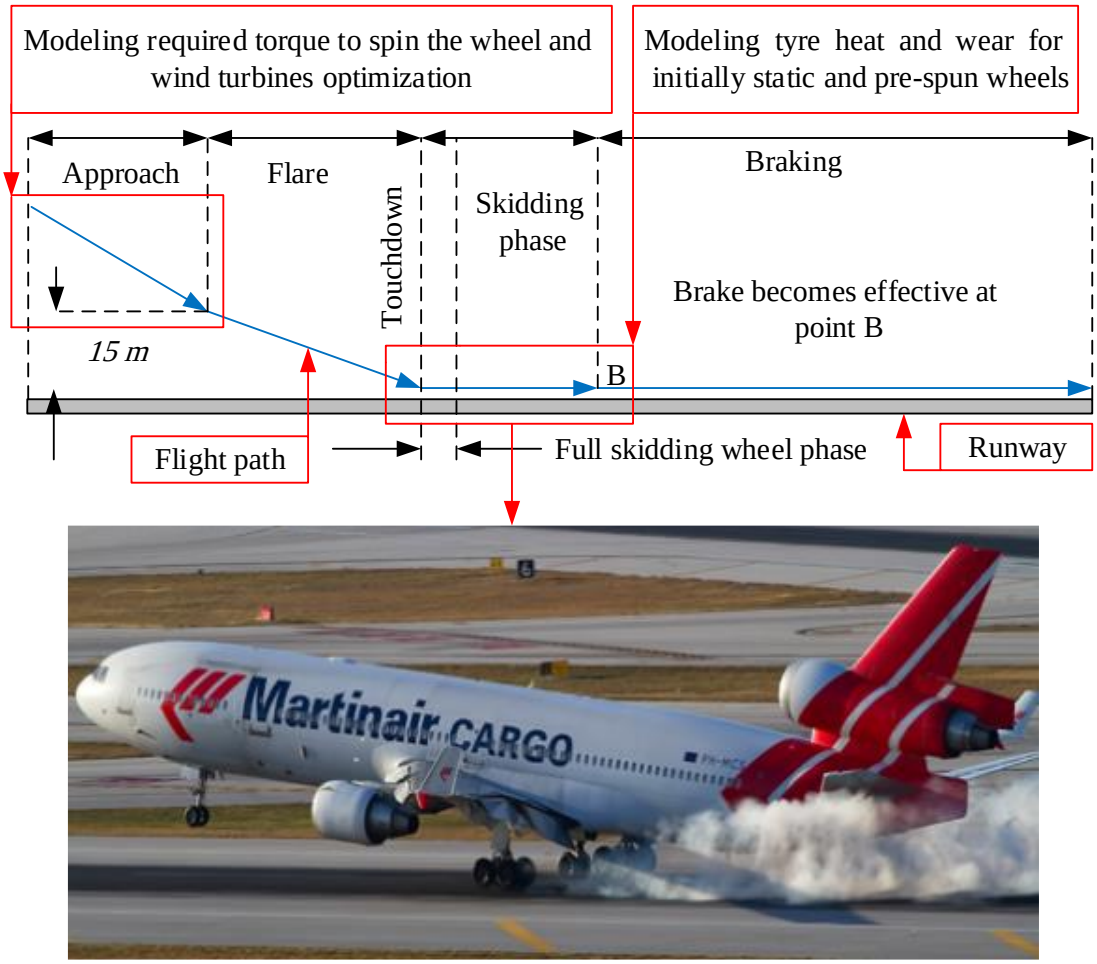

Figure 1.1 Typical aircraft flight path (modified from [33]), landing smoke, and research areas.

1.2.3 Landing Gear Dynamic and Tyre Construction

The tyre models rely on knowing how the vertical load reacted at the contact patch. To calculate the force reacted by the tyre, a vehicle model describing the dynamic loads imparted that bear down on the aircraft's landing gear wheels is required. Typical large aircraft landing gear structures rely on a mechanical device known as an oleo strut, shown in Figure 1.2, which is an air–oil hydraulic shock absorber. It cushions the impacts of landing and, while taxiing, it damps out vertical oscillations. An oleo strut consists of an inner metal tube or piston, which is connected to the wheel structure and moves up and down in an outer (or upper) metal tube that is attached to the airframe. Oils and gas fill the cavity located within the strut and piston. A small orifice connects the two chambers into which this cavity is divided. The compressed gas contained in the cylinder supports the weight of the aircraft when it is on the ground and static. When the aircraft is landing or taxiing over bumps, the piston slides up and down and this action compresses the gas. The oil is thus forced through the orifice by the compressed gas acting as a spring, and this acts as a damper [35].

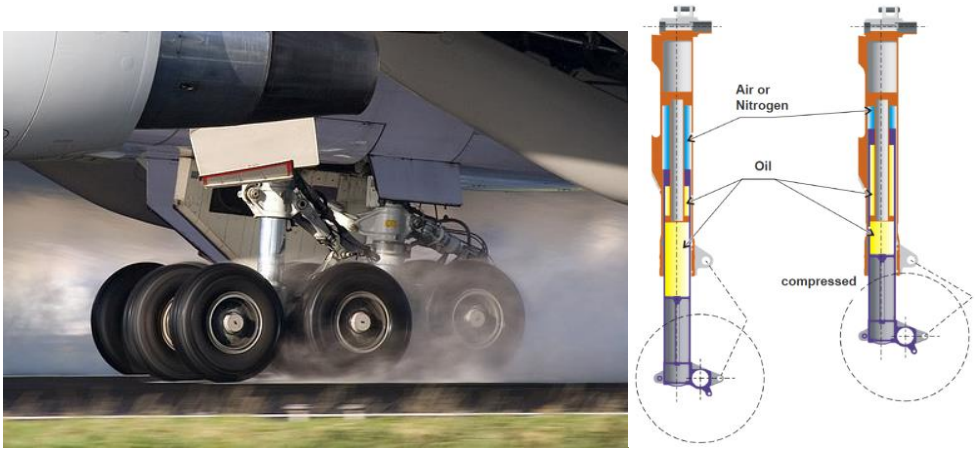

Figure 1.2 Oleo strut piston mechanism visible on a Boeing 747 (lift) [36], Oleo-strut mechanical workings (right) [37].

There are two types of aircraft tyre; radial and bias. Manufacturers are increasingly turning to the radial tyre as it is lighter in weight, has better performance at landing, and better resistance to foreign object damage (FOD) [38]. Figure 1.3 shows the typical construction of an aircraft radial tyre.

The landing smoke is the result of melted and eroded tyre tread as it makes contact with the runway [3]. The tread material is a rubber compound which has good resistance to wear. Most of the aircraft tyre tread has grooves to allow the water to pass through it in case of a wet runway; and to improve the ground friction between the tyre and the runway [39].

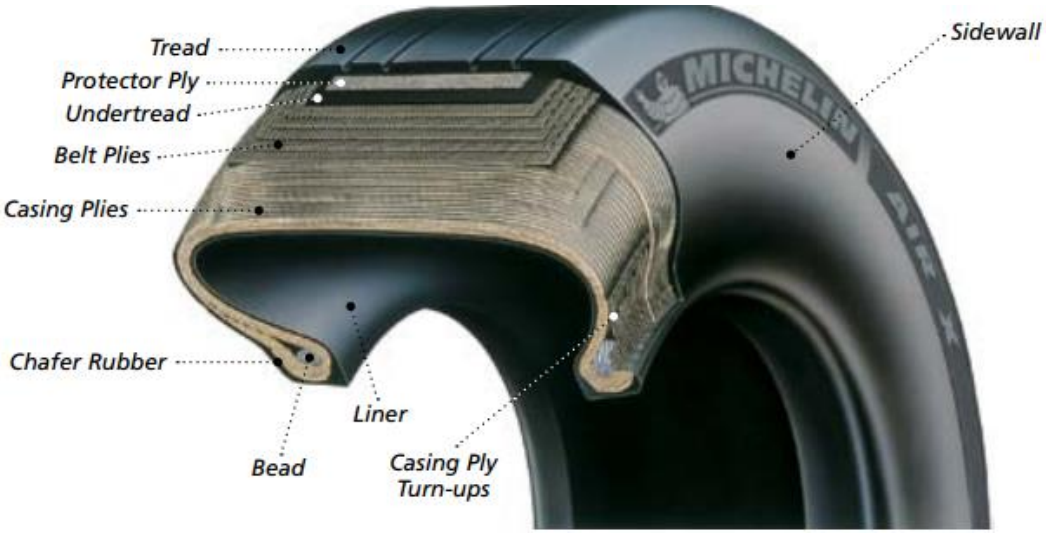

Figure 1.3 Typical construction of an aircraft radial tyre [38].

1.3 The Effect of Landing Smoke on the Economy and Environment

Aircraft landing smoke has economic consequences as well as environmental ones. The following material presents and analyses the facts about how tyre wear and landing smoke impacts the environmental surroundings of airports, human health and safety, and costs to the airline operators, airports and affects the wider economy.

1.3.1 Economic and Safety Impacts

1.3.1.2 Runway Contamination and Cleaning

Rubber material worn from aircraft tyres via abrasion between the tyre and asphalt runway surface builds up on the runway surface [2]. The heat caused by the friction of a tyre hitting the pavement and spinning up to a free-rolling velocity changes the rubber composition, melting it into a hard, carbonized layer [6].

Bennett, et al. (2011) [6] suggest the average mass of all the main landing gear tyre tread material eroded per landing is 1kg for a wide bodied airliner. Water-blasting Technologies company which removes aircraft tyre rubber from the runway, has estimated the rubber deposit on the runway to be in the range of 0.45-0.68 kg per aircraft landing [40].

Federal Aviation Administration (FAA) figures state that the world's busiest airport, Chicago O'Hare, had 881,933 flight operations (about 440,966 landings) in 2014 and the 30 busiest U.S. airports saw over 6.268 million landings in the same year [41]. That makes roughly 2,820 tons of rubber deposited on the runways (based on 0.45 kg per landing [40]) for those 30 airports alone in 2014. It is important to treat deposits of rubber

build-up correctly and regularly; otherwise the friction level of the runway decreases. Potentially, this can cause loss of directional control for an aircraft, particularly in wet weather [40]. Figure 1.4 shows rubber-removal from a runway.

In aviation, the second biggest cause of accidents and incidents is when aircraft land on runways that are wet or contaminated. The reduced friction can result in aircraft skidding off the runway [42]. Tyre wear is therefore a safety issue as well as an economic one.

Figure 1.4 Rubber-removal contractors cleaning carbon-black rubber deposits from a runway [43].

US airports regularly carry out Runway Friction Level Testing. Continuous Friction Measuring Equipment (CFME) which has been approved by the Federal Aviation Administration (FAA) is used for this and determines if any cleaning of runway rubber is necessary. The CFME also measures the amount of runway surface deterioration, so that a corrective plan of action can be put in place and ensure that aircraft can land safely on the runway.

Friction level classifications have been devised by the National Aeronautics and Space Administration (NASA) based on their correlation tests at the Wallops Flight Facility. They used many types of friction tester machine. The testers operating at two speeds to check the friction levels are not below 0.42 and 0.26 at tester speeds of 40 and 60 mph respectively. The correct rubber removal equipment should be used to eliminate any build-up of rubber and other contaminants on the surface of the runway when the levels of friction are below the action level [44].

The safety concern from aircraft tyre wear depositing material on runways should be considered among many other factors including the volume of aircrafts landing on the runway, as well as weather conditions [45]. Table 1.1 shows how often the FAA recommends that friction tests should be carried out.

Table 1.1 FAA recommended runway friction testing frequency [45].

Number of daily minimum aircraft landings per runway end	Minimum friction survey frequency
<15	1 year
16-30	6 months
31-90	3 months
91-150	1 month
151-210	2 weeks
>210	1 week

Runway rubber removal cleaning operation costs include the cost of amortization of installed instruments and machinery, maintenance, staff, fuel and operations. Indirect costs for cleaning rubber include costs for inspection and approval of staff and equipment. Time spent testing and cleaning runways reduces the income revenue from landing fees as the runway is effectively out of use, and air traffic control is disrupted. Although an exact cost for cleaning worn tyre material from runways is difficult to define, any technology that can reduce tyre wear will directly reduce the amount of runway cleaning required and hence reduce the associated costs. The safety aspect of runway surface contamination cannot be ignored as the potential legal costs due to accidents from improper runway maintenance and the immeasurable human life costs are enormous.

2.3.1.2 Tyre Replacement and Retreading Costs

An aircraft is able to safely operate with an acceptable amount of tyre wear. During its lifetime a tyre will have been retreaded on average five times; and at least 95% of aircraft tyres being used at any one time have been retreaded [47]. Tyres can be damages in many ways, as shown in Figure 1.5.

The oval-shaped flat spot or skid burn in the tread rubber shown in Figure 1.5 (a) is caused by aggressive skidding, where the wheel does not rotate and the rubber abrades against the ground.

Figure 1.5 (b) shows tread rubber reversion, where an oval-shaped area in the tread similar to a skid is worn, and rubber has been burnt due to hydroplaning on a wet or contaminated runway.

Open tread splicing is shown in Figure 1.5 (c), where a crack appears in the tread rubber where the joint (splice) separates in a radial (sideways) direction.

Figure 1.5 (d) shows the wear pattern from chevron cutting, which is damage caused by running and braking on cross-grooved runways. If tyre wear is bad enough for the internal ply fabric to be eroded, structural rigidity is lost and the tyre must be replaced. If only the rubber tread is affected by wear then the tyre may be retreaded to extend its life or for rebalancing [46].

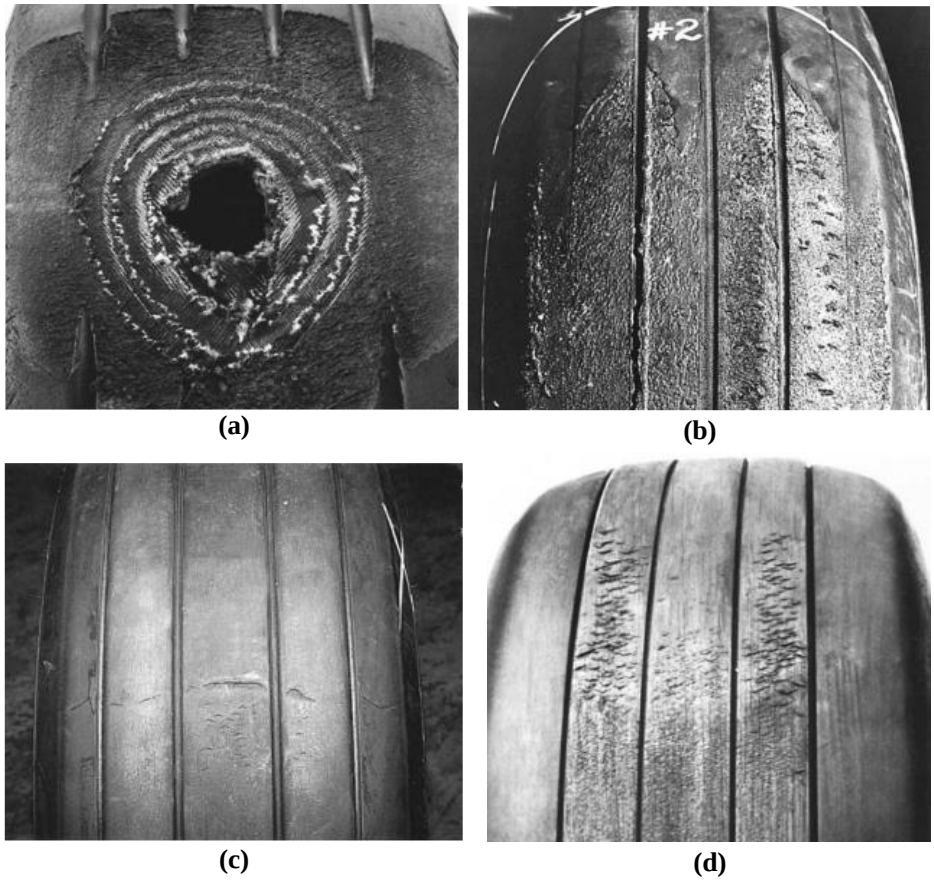

Figure 1.5 Tyre tread wear patterns: (a) Skid, (b) Tread Rubber Reversion, (c) Open tread splice and (d) Chevron cutting [46].

Chai and Mason (1996) [48] report that the cost of a new tyre for a Boeing 747 is $2,100 and $2,900 for a Boeing 777; and about only 300 landings are allowed for tyres before they have to be replaced.

The cost of retreading is roughly $1,312 per tyre. A new tyre replacement is required in 2.5% of cases, where embedded foreign objects deep in the rubber are found during the retreading process which could cause further damage if reused [49]. Finding embedded foreign objects before sending a tyre to be retreaded saves the aircraft operator the retreading cost, but the expense of a new replacement tyre is incurred. McCreary (2008) [49] states from Air-Transport of America (ATA) data that aircraft tyres are sent for retread every 100 flights.

From the data above, the overall cost of tyre retreading and replacement per landing can be approximated at $54.24 to $64.91 per tyre per landing:

$$\text{Cost per tyre} = \left(\begin{array}{c} \dfrac{(\$2100 \text{ to } \$2900)\ \text{replacement}}{\text{per 300 landings}} \\ \\ + \dfrac{\$1312\ \text{retread}}{\text{per 100 landings}} \\ \\ +2.5\% \times \dfrac{\$1312\ \text{retread} + (\$2100 \text{ to } \$2900)\ \text{replacement}}{\text{per 100 landings from retread with emdedded foreign objects}} \end{array} \right)$$

Some large wide-bodied aircraft have 18 tyres, so the average cost of retreading and replacement per landing is between $976.32 and $1168.32 for all tyres in the aircraft's landing gear.

1.3.2 Environmental impact

One of the several issues restraining the development of airports is the local air quality, which is greatly affected by the smoke produced by rubber tyres reaching critical temperatures during landings [50]. Tyres are reported to generally lose up to1 kg of tread material per landing, 32% of which is emitted as smoke [6], containing 270 mg of harmful particulate matter (PM) for wide-body airliners [52].

It was long thought that size of tyre deterioration particles was not sufficiently small to be a danger to health [53]. However, in research carried out by Montague (1995) [54], it was shown that people who lived near motorways had a higher sensibility to oncology and allergic illnesses; and that this was due to aerosol emissions into the atmosphere caused by the wear of automobile tyres. The study revealed that the tyre particles per cubic meter of air in these areas ranged from 3,800 to 6,900. Over 58% of these particles were less than 10 microns, and thus small enough to be able to go into human lungs, causing allergic reactions and bronchial asthma. The human body is unable to excrete these tyre particles. Research carried out in Moscow in 2003 [53] demonstrated that automobile tyre rubber which had been worn into tiny particles was a core pollutant of the city's air, as it constituted 60% of the hazardous matter therein.

There are costs for the treatment for respiratory diseases due to increases in particulates, the reduction in house values due to noise generated from airports and for cleaning buildings contaminated by aviation pollution. Aviation may well be responsible for these costs to society, but it does not pay for them [50].

Rubber procured from factories is required for replacement of tyres which in turn affects the environment by emitting hazardous chemicals and materials into the atmosphere and waterways [55].

As far as the impacts of the rubber are concerned in the rubber industry, environmental issues are incurred by the utilization of chemicals at various stages of operations which harm local ecosystems.

The effluent from rubber processing is acidic in nature and accumulates in the air and soil after discharge from the factories, polluting the climate. Other chemicals used in tyre manufacturing include high levels of ammonia, sulfate, nitrogen compounds which are all highly toxic and harmful to the environment. Control of pollution from rubber tyre production for environmental preservation costs manufacturers as well as airlines because both have to take costly preventive measures including wastewater treatment practices and in-plant control measures [56].

1.4 Thesis Outline

Chapter 2: Literature review covering: aircraft landing smoke, tyre temperature, tyre wear, the elimination of aircraft landing smoke patents survey, drag turbines and wheel aerodynamic forces.

Chapter 3: The tyre temperature for initially static and pre-spun wheels are presented and discussed. The first objective is to validate the use of the pre-spinning technique to reduce the tyre tread temperature below the rubber's critical temperature. The second objective is to know how much initial wheel rotation is sufficient to avoid tyre tread reaching its melting point, which results in smoke.

Chapter 4: The tyre wear for initially static and pre-spun wheels are discussed in the light of the results presented in Chapter 3, and demonstrates that the tyre tread hardness is a function of material temperature. Further, the reduction of the tyre wear by pre-spinning wheel is investigated.

Chapter 5: Simulations are made of the wheel as it approaches landing at different wind speeds. The wheel is rotated from zero to the required rotational speed to measure the forces created and then to calculate the torque required to spin it.

Chapter 6: With reference to the results from Chapter five, different types of drag turbines are simulated in order to estimate optimal turbine size, acceleration and targeted rotational speed of the wheel.

Chapter 7: Conclusions and Future Work

1.5 Published papers and conferences

Table 1.2 shows the connections between the chapters and corresponding papers and conferences.

Table 1.2 The connections between the chapters and corresponding papers and conferences.

	Title	type	Status	Corresponding chapter
1	Alroqi, A., Wang, W., and Zhao, Y., "Aircraft Tire Temperature at touchdown with wheel pre-rotation," AIAA: Journal of Aircraft.	Journal paper	Accepted	Chapter 3
2	Alroqi, A., and Wang, W., "The prevention of aircraft tires overheating by pre-rotating the wheels," The 7th International Conference on Mechanical and Aerospace Engineering (ICMAE 2016), 18-22 July 2016. doi:10.1109/icmae.2016.7549581.	conference	published	Chapter 3
3	Alroqi, A., and Wang, W., "Reduction of Aircraft Tyre Wear by Pre-rotating Wheel using ANSYS Mechanical Transient," AEF, vol. 17, pp. 89–100, Jun. 2016, doi:10.4028/www.scientific.net/aef.17.89	Journal paper	published	Chapter 4
4	Alroqi, A., and Wang, W., "A Comparison of Aircraft Tire Skid with Initial Wheel Rotational Speed using ANSYS Transient Simulation," 5th International Conference on Mechanical and Aerospace Engineering (ICMAE), Berlin, Germany, November 28th 2015.	conference	published	Chapters 3&4
5	Alroqi, A., and Wang, W., "Comparison of Aircraft Tire Wear with Initial Wheel Rotational Speed," International Journal of Aviation, Aeronautics, and Aerospace, Vol. 2, NO. 1, 2015, pp. 1-30. doi:10.15394/ijaaa.2015.1043.	Journal paper	published	Chapter 4
6	Alroqi, A., and Wang, W., "Determination of Required Torque to Spin Aircraft Wheel at Approach Using ANSYS CFX,." American Journal of Aerospace Engineering. Vol. 3, No. 2, 2016, pp. 13-23. doi:10.11648/j.ajae.20160302.12	Journal paper	published	Chapter 5
7	Alroqi, A., and Wang, W., "Pre-rotation Wind Turbine Design and Optimization for Aircraft Landing Gear," Advance Engineering Forum journal.	Journal paper	Accepted	Chapter 6

Chapter 2

2. Literature Review and Survey

The objective of this literature review is to give an overview of the subject and find the methods and resources required to model tyre temperature and wear during aircraft landings, evaluate suitable spin-up devices and give an overview of the aircraft wheel aerodynamic forces when rotating. Section 2.1 covers a literature review of modelling tyre temperature and wear during aircraft landings; in section 2.2 a collection of the elimination of aircraft landing smoke patents are assessed; section 2.3 analyses various wind-turbine designs and in section 2.4 there is a literature review of isolated rotating wheel aerodynamic forces.

2.1. Aircraft Landing Smoke, Tyre Temperature, and Tyre Wear

Bennet et al. (2010) [57], while intending to characterize engine exhaust dispersion, found the magnitude of particulate mass in tyre smoke to be an order of magnitude larger than emissions produced by the engines.

In a later study by Bennet et al. (2011) [6] experiments were conducted to determine the physical composition of tyre smoke generated by landing aircraft. They used a scanning LIDAR with optical condensation particle counters to find that landing smoke consists of particles found in tyre rubber and components of runway asphalt. Bennet et al. (2011) [6] approximated that a typically large aircraft loses 1 kg of tyre mass per landing over the entire landing gear apparatus. The tyre smoke measured by Bennet et al. (2011) [6] was

generated over 0.32 seconds after aircraft touchdown, and extended 75 m along the runway. It is doubtful that the aircraft tyres skidded over 75 m, although aerodynamic suction from the large aircraft body could explain the spread of smoke along the runway. The total tyre wear was estimated in Bennet's study (2011) [6]; and only 32% was estimated to be emitted as smoke, while the major part of material worn from the tyres remained on the runway surface.

Literature describing the physical process that causes aircraft tyre rubber to vaporize under landing loads is sparse, although multiple studies have been reported in the automotive field. Tyre skid-marks are caused by material being removed by abrasion between slipping tyres and the asphalt road surface.

Persson (2006) [58] states that the friction force generated between the tyre and asphalt surfaces is related to the internal friction of the rubber, which is a bulk property. The hysteretic friction component is determined by gripping and sliding of the rubber over a rough surface. These oscillating forces lead to energy dissipation, which can cause heating of the tyre material to a level where smoke is produced.

Few studies were found to have attempted simulation modelling of longitudinal tyre dynamics during landings. In the first, Padovan et al. (1991) [1] built an energy-balance model to compute the rate of work due to interfacial friction between tyre and runway surfaces and its effect on the growth of wheel rotary inertia and slip work. In the study, calculations were based on a model of the space-shuttle, which experiences a large amount of tyre wear per landing. A simple Coulomb-friction model was employed, using a constant friction coefficient and a non-linear curve fitted to experimental data to express

vertical tyre load. It was concluded from various simulations that tyre wear was increased with horizontal landing speed, sink rate and surface friction coefficients.

Slagmaat (1992) [59] investigated suitable tyre models for simulating longitudinal aircraft tyre dynamics and found the Pacejka 'magic formula' models, popular in automotive literature, were not suitable to represent the fast-dynamics in aircraft landings. Significant simplifications were applied to the Pacejka tyre model, and a multi-body nonlinear landing gear model was implemented for vertical tyre-load simulation, although comparisons with experimental results were not made, due to a lack of reliable experimental data being available.

Besselink (2000) [60] developed a model allowing for the simulation of lateral “shimmy” oscillations in a Boeing 747-400 aircraft’s main landing gear. Although the scope of this work does not involve lateral dynamics, some important experimental data was recorded, including experimental wheel speed time traces measured on a Boeing 747-400 aircraft during landing, which are useful for validating our simulations. Measured data in both Besselink (2000) [60] and Khapane (2006) [61] show aircraft tyres accelerating from zero rotational speed to a free-rolling velocity within about 0.1 seconds from touchdown.

Padovan, J. and Padovan, P. (1994) [62] developed a methodology and correlated algorithms to model aircraft tyre wear and temperature during the use of an antilock braking system (ABS). They estimated the tread surface temperatures for different landing speeds in the range of 20 – 80 knots (10 – 41 m/s) and the total vehicle weight being 9979 kg. They used two methods: harmonic ABS cycling point wise and square

wave on/off ABS braking point wise. However, the temperature they recorded reached 204 ˚C within a portion of a second during maximum landing speed.

Linke et al. (2014) [30] used a high speed linear tester at the Institute of Dynamics and Vibration Research in Hanover, Germany to investigate aircraft tyre tread temperature when a wheel is fully locked (slip ratio =1) at touchdown. They found that by using a block of rubber sliding on a concrete track for 5.5 m and a bellows cylinder to increase the vertical pressure being applied on the rubber, the sliding rubber temperature rose up from 22 ˚C to 171 ˚C after 2 m distance. This was effected by a pure sliding speed and a 25 bar vertical load. The addition of pressure on a sliding locked block may increase temperature, however, increasing the pressure (load) on a free-rolling tyre during touchdown will actually reduce the temperature by reducing the slip distance.

Kondé et al. (2013) [63] are modelled an aircraft tyre in cornering using finite element software and experimental devices for pure sliding rubber. They tested the fully locked wheel under a 250 kN constant vertical load and a 50 km/h sliding speed to estimate heat flux generated by friction. However, the tyre tread temperature increased significantly to 190 ˚C when the tyre slid over a 4 m distance. This result is useful to validate heat flux generated by our model.

In early research, NASA (1960) [64] did some simulations to estimate tyre tread temperature during the skidding phase. They found that the average was 800 F (426 ˚C). Another test by NASA (1969) [65] found that the tread temperature reached 315 ˚C.

In this thesis, a coupled transient structural – thermal in ANSYS has been used to model a single wheel main landing gear to find the tyre temperature and wear. This model

simulates the real landing with touchdown speeds, including sink rate. It also has the wheel connected to a shock absorber, to find the damping force and the wheel's dynamic behaviour.

2.2. The Elimination of Aircraft Landing Smoke Patents survey

Here, examples of patents designed to prevent the aircraft landing smoke are presented. Patented solutions have been suggested by Beazley (1947) [9] and later by other inventors. As a result, various ideas have circulated since as early as the 1940s, several of which are presented here. Patents for aircraft wheel rotational devices and methods focus on ideas that range from simple to mechanically complex. The literature indicates that some pre-rotating systems are mechanically complex, heavy or not durable. Therefore, several patents focus on passive air flow systems that require modifications to the wheels themselves to cause the air stream to rotate the descending wheels before they touch the ground. Most of these are wheel-mounted accessories intended to utilize the air stream during descent to start aircraft tyres rotating before touchdown, while others are complex systems of magnetic, hydraulics, compressed air and gas and similar mechanical systems. Pre-rotation is the primary means of getting tyres on an airborne plane to begin spinning before they hit the tarmac on landing.

The first patent was published by Beazley (1947) [9]. He writes of experiments with vanes or cups mounted on wheels as early at 1944 that proved unsatisfactory on pneumatic tyres. Another early method of pre-rotating tyres was to provide a surface on which they could begin to spin before landing; both methods had too many disadvantages. Likewise, it was important to delay initiating spin to avoid a gyroscopic

effect of rotation on the airplane. Therefore, Beazley (1947) [9] devised circumferential pockets or recesses with a nozzle extending downward and forward to spray 'motive fluid' such as compressed air normally carried by an aircraft via a flexible conduit. An electronic or ‘electric eye’ valve operates the nozzle and is pilot-controlled. If the wheels are not fully extended, the valve will not operate, which gives the pilot a warning that there is a problem with the wheel mechanism. A predetermined amount of compressed air moves the wheels forward at the desired speed.

Abbasszadeh et al. (2015) [10] suggested using many cone shapes connecting with plate on the wheel rim in their patent. Every cone has a circular leading edge to produce as much air resistance as when it is facing the wind to spin the wheel before landing.

In the year of 2014, three patents were published. Sweet et al. (2014) [11] suggested using electric geared motor assembly to spin the wheel. Also, an electric motor has been suggested by Didey (2014) [12] of the Airbus company. Karl (2014) [13] applied for a patent on his very similar hub-mounted free-spinning device designed to pre-rotate wheels. Winter’s crescent-shaped airfoils are essentially the same as the foregoing descriptions of hub-mounted, free-turning devices.

Sami and Anis (2013) [14], utilize a radially-hinged flaps made of a flexible resin plastic base, then Kevlar-type material, then a top layer of similar material as the base; all bonded together with stitching, adhesive, and/or thermoplastic bonding. Each disc-shaped piece has passive, auto-retracting flaps or vanes that open when exposed to the air stream created by the descending plane. Above the horizontal centreline of the wheel, the hinged flap stays closed; below the tyre's centreline, air pushes the flaps open and fully open at

the bottom; and this action torques the wheel into rotation. Additional structures keep the flap from exceeding 90 degrees when open. Among the drawbacks of this device is that the outer circumference of the disc may include a weighted ring to supply centrifugal force to reset a disc displaced by a rough landing also, bolting into the tyres themselves may compromise their inherent structure. Thus, this assembly does not appear to be as viable a design as some others.

The Japanese team of Ushiyama and Tawara (2013) [15], also take an airstream approach. While their description is comprehensive and complex, their design concept is that of a 'revolution drive disc' with a 'rubber ringed plate and plural fins' that is attached to the side of the tyres with and appropriate adhesive. When struck by air flow when the wheels are lowered, the six rubberized projecting fins make the wheel turn in a forward motion.

Gooding et al. (2011) [16] repeat the airfoil design, this time confining their 'windmill machine' to the front landing tyre, a device to be bolted to the wheel hub. They created a model using Styrofoam airfoils attached to an aluminium backing and attached to an automobile tyre. Subjecting the device to a light headwind of 1.95 m/s and altering their airfoils to determine the best efficacy, it managed to pre-rotate the tyre. However, their device has not been made to withstand landing airspeed headwinds, tested in a wind tunnel, or even reached a stage of materials determination.

Liu et al. (2011) [17] adapted magneto rheological (MR) dampers used in other aerospace and automotive applications to reduce vibration and excessive force upon landing. They researched and created mathematical calculations to prove that incorporating MR

dampers that utilize fluids to modify the dynamic range and lower power needs act as semi-active actuators to significantly improve wheel performance upon landing. Although no actual working models were achieved, the concept of MR dampers appears viable if incorporated appropriately with a pre-rotation device; therefore, their research is included.

Broitzman (2009) [18] attempted to bring the concept of incorporating airfoils onto the sides of tyres into the public domain so that aircraft tyre manufacturers would not suppress the idea. His design incorporates two kinds of airfoils: one curvilinear molded onto the tyre during manufacture that are equidistant, apart from the hub to the outer edge of the tyre; the other airfoils are angled squarely at ninety degrees. His design is a bit too simplistic and would likely run into problems without having some kind of shielding over the top half of the tyres. Nevertheless, the problem with all airstream type wind airfoils are that they do not take into account frequent cross currents of air that occur during landing and how those changing winds might impact the operation of the airfoils. Further, most are not controlled by the pilot, which can, in and of itself, become problematic if there is any kind of landing problem. Finally, the up-spin, while predictable by simple physics, is not speed-reliable and assumes that all tyres will pre-rotate at the same speed and that every landing will be directly into a prevailing, steady wind, which is not always the case.

Soderberg (2009) [19] has patented a 'magnetically induced' wheel pre-rotation assembly. His device consists of a stationary piece and a rotating component that is operated by electromagnetic to begin forward rotation and also support braking operations after landing. Endeavoring to improve on previous applications, Soderberg’s design (2009)

[19] adds the feature of being able to retard forward motion of the tyre when that is needed. His assembly is somewhat complex and requires microprocessor incorporation of the electromagnetic application with the plane's computerized system, as well as additional linkage to the brake system, claiming all parts are readily available in current technology markets. Soderberg (2009) [19] overcomes lack of space problems by melding his component parts with the existing static and rotating structures of the landing wheels. However, it is not exactly explained how incorporation of electromagnets and microprocessors into the delicately precise landing system might react with other precision parts that could be negatively impacted by such magnetic reactions. Nevertheless, his design does differ in its proposed ability to also contribute to retarding forward movement, although pilots would have to learn how to manage the difference.

Schmitz (2009) [20] builds upon Soderberg's idea (2009) [19] of airfoils. Schmitz takes a slightly different approach by incorporating a valve device between the jet engine and the wheel that gets its power from the gases and compressed air of the jet engine. The system relies on existing on board instrument information to control wheel spin with precision and "integrate the propulsion device into the wheel structure". This eliminates problems of extra weight from an additional device, limits aerodynamic impacts, offers more control of wheel spin, and permits the use of existing tyres without modification. Schmitz's design compensates for temperature extremes during flight and uses simple high-pressure lines between the jet engine and the wheel for operation. A processor-controlled valve in the line controls the flow of compressed air and gas, remaining closed after touch-down. The processor depends upon on board controls to determine what its

position and functionality should be. Schmitz' design relies on the assumption that airfoils are incorporated in the wheel.

Zha (2007) [21] also devised tyre-mounted airfoils to be attached to one or both sides of the tyres. In what he describes as a "plurality of airfoils" appended to the tyres rather than the hubs, the airfoils are intended to provide higher torque to pre-rotate the landing gear wheels. The airfoils could also be integrated with the tyre when it is manufactured. Although Zha (2007) [21] provides detailed wind speed and rotation speed tables to justify inclusion of airfoils on tyres, his design concepts and drawings are remarkably similar to others that have been around since the 1970s and add nothing new to the discussion. Moreover, without an accompanying fairing, the airfoils simply may not work.

Horvath and Szoke (2006) [22] avoid the addition of an assembly to the wheel and instead alter the tyre's design to incorporate curved airfoils that protrude from both sides of each tyre. Placing the airfoils on both sides, they claim, will minimize the protrusion. They suggest the airfoils could also be attached to existing tyres and made of "durable material", suggesting rubber, synthetic rubber, and closed or open cell foam. This material can then be bonded to "the carcass plies by nylon fabric or other methods, and covered by rubber or other synthetic materials". While this is a potentially good concept, Horvath and Szoke (2006) [22] have not executed their idea to see whether it works. Moreover, such a tyre design change would likely also require all new wheel assemblies and enclosures to accommodate them, which is neither cost effective nor feasible. Using the physics of moving air is a primary focus of many patents focused on aircraft wheels.

Airstream is provided by the plane moving through the air, generally hitting protruding flaps or vanes or protrusions attached to the wheels in a pinwheel configuration.

Yoshioka et al. (2005) [23] examined the aircraft wheel's vertical shock absorber known as the oleo strut and its inability completely absorb forward movement of a landing plane. They devised a "crank element to absorb horizontal shock from the forward direction". Thus far they have relied solely on computer simulations that demonstrated a 62.1% reduction at the oleo strut's maximum bend point and a resulting 69.9% reduction in the tyres' sliding friction. Their simulation tests also reduced vibration, resulting in an assumed smoother landing. In addition to only having simulation testing thus far, the added weight of their device is considerable; however, their statistics, if reliable in translation to actual application, is quite impressive.

Suzuki (2002) [24] also takes a mechanical approach to spinning aircraft wheels before landing using pure pneumatics. His wheel drive unit has a pneumatic motor utilizing compressed air to turn a first impeller (an expander); then a second impeller (turbine-type) is turned by the first impeller's exhaust. Together, the two impellers, fixed to the axle of the wheel, then turn the wheel together with a third impeller that is housed in a sealed airtight case. According to Suzuki, this pneumatic motor can accelerate the wheel to match the aircraft speed upon landing. The pneumatic motor not only drives two impellers, it can act as a vacuum brake by controlling the impeller in the airtight housing. According to Suzuki, it is a "compact, high-torque, high-speed drive unit/pneumatic actuator for the wheel unit" to increase safety on landings and take-offs. One advantage noted by the inventor is that his design has no upper rotational speed limits. However, limitations that do come to mind are those imposed by the complexity of this apparatus

and its potential for pneumatic failure that would then compromise the landing equipment.

Lyons (2002) [25] also approaches the problem with the application of physics and wind. His design is essentially a hubcap arrangement with raised vanes that rotate in the airstream with the top half of the assembly covered by a shroud so that only the bottom vanes are exposed. As the landing gear is lowered, the vanes begin to turn, and the stationary portion of the hub torques the wheel in forward momentum. Very similar to Lyons' design (2002) [25] is Opitz's design (1975) [26] that also utilizes a shroud or "deflecting fairing" to cover half the tyre while exposing the lower portion of the tyre to air flow. Once again the longitudinal centre of the tyre is the dividing line with a wheel rotator exposed on the bottom half to create torque when the wind drives it. Advantages of the design are its simplicity and the ability to attach them to existing wheel hubs. Among the disadvantages are concerns about the shroud that might come off, compromising one or more wheels' momentum and potentially interfering with a safe landing. The assembly also must be anchored to the wheel's axel, which might be damaged in the event of assembly failure. Finally, as wind speeds and landing speeds vary widely, such variables as crosswinds, ground speed, aircraft weight, tarmac condition, and more can alter the design's effectiveness negatively.

Almen (2002) [27] also designed an airfoil assembly to be bolted to the rims of aircraft tyres intended to use airstream to initiate wheel spin. His bolt hole patterns are said to line up with existing wheel rim holes, although for a "preselected aircraft" – in other words, it is not one size fits all. His radial air vanes are intended to catch the wind and bring the

tyre to pre-rotation at an assumed same speed as the landing aircraft. Once again, the same concept is in place without practical testing.

Gannatal (1993) [28] tackled the challenges of landing a space shuttle, a vehicle requiring substantially longer landing space than conventional aircraft. One again, an airfoil concept was incorporated; however, this time, the device is intended to essentially self-destruct upon landing. The device is attached to the wheels by bands that fit into grooves to be built into the tyres. Cups are collapsed by elastic bands until it is time to allow the wind to catch them; they also stiffen when filled by the wind so they do not bend backward and collapse when they are not supposed to do so. A break-away buckle automatically releases when the shuttle touches down. Gannatal's ideas (1993) [28] are problematic. Firstly, he requires specialized tyres with grooves to hold his apparatus. More significantly he puts the devices on the shuttle tyres. They may not survive lift off and therefore could not be put into place before departure, even enclosed in wheel wells. Secondly, expecting astronauts to put them on while deployed in space is not reasonable. Finally, should the release buckles fail, a safe landing could be compromised.

2.3. Drag Turbines

A drag turbine is essentially a wind device whereby the wind pushes against the blades, forcing the rotor to turn on its axis. The efficiency of this device is limited by the speed of the wind, as the blade rotation cannot exceed wind speed [26]. Typical examples of a drag turbine include cup anemometers and vanes, along with paddles which can change turn parallel to the wind, clam shells that open on the downward wind side and close on an upwind. These devices are inefficient for energy production because each has a large

torque with a low rpm rate which makes them unsuitable for commercial energy production. However this torque could be useful in stimulating movement in the aircraft wheel prior to touchdown. Another benefit of this form of turbine is that they are relatively easy to construct [66]. There are a number of drag turbines on the commercial market, such as the Savonius models and the Darrieus turbine along with the solar wind turbine, the helical style drag turbine and the Maglev. In addition there are the Nogushi and the Cochrane vertical axis turbines. Given the end-use of the drag turbine being considered in this thesis and the foregoing requirements for wheel and tyre design, it is suggested that only the Savonius and the Darrieus models are suitably robust for this study.

2.3.1 The Savonius Drag Turbine

The manufacturer Savonius produces a drag turbine called the drag-type Vertical Axis Wind Turbine (VAWT) [67]. This type of wind turbine can be easily fitted on the wheel's rim to spin the wheel. According to Tong (2010) [68], the Savonius drag turbine was originally developed in the early 20th century and has since been adopted for use in building integrated wind energy systems, in water pumping and natural ventilation stacks. As shown in Figure 2.1 (a), the basic version of the Savonius VAWT is a rotor with an S-shaped cross-section typically formed by two semi-circular blades which have a small overlap [69].

Tong (2010) [68] describes a vertical turbine as having a vertical axes perpendicular to the ground with the advantage that this arrangement can accept wind from any direction and does not require a yaw control, as the movement is limited by the speed of the wind.

It is argued that this could be useful in runway conditions where there can be cross winds and local air turbulence. The Savonius rotor is available in a number of different configurations, including a two-blade, three-blade and even four-blade configuration. In addition the rotor is available as a single stage operation or a double stage rotor [68].

Figure 2.1 (b) shows that the turbine operates in a manner similar to a cup anemometer with two blades mounted on a rotor. The blades are free to spin in the wind and the layout is such that at any time one of the blades will face into the wind, with the remaining two backing into the wind. The back of the cups are designed to reduce drag and as such a have curved shape. This difference in drag creates a force that drives the blades and turns the rotor.

The design is such that the open cup is moved through the wind cycle becoming the cup with its back to the wind; this rotation continues as long the wind blows, as shown in Figure 2.1 (c).

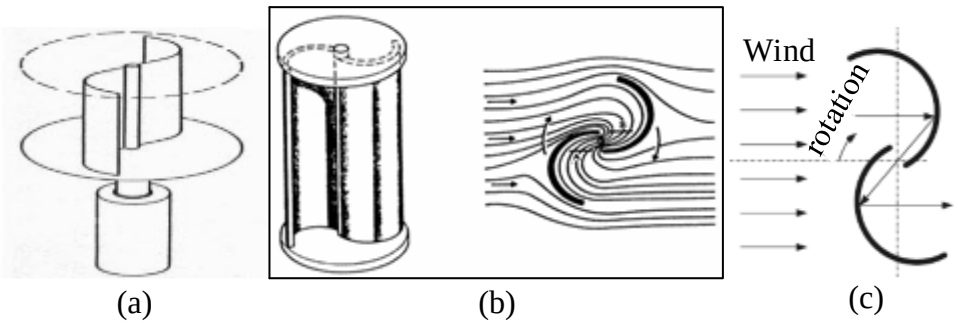

Figure 2.1 (a) Drag Type Vertical Axis Wind Turbine, (b) Drag forces driving the cups and the rotor of the Savonius VAWT [67], and (c) Operating Principles for a Savonius VAWT turbine [71].

According to Altan and Atilgan (2012) [70], the wind hitting the Savonius wind rotor creates a positive wind force that constitutes a positive torque on the concave blade with a corresponding negative wind force that constitutes a negative torque on the convex blade. The torque is a function of the wind speed and the orientation of the blade. The differential in torque secures the rotation movement of the rotor.

Rajbongshi et al. (2014) [72] studied the performance of a three bladed Savonius rotor in which rotational speed could be varied with the addition of semi-circular deflectors, whereby the speed of rotation increased with the number of semi-circular deflectors. Paraschivoiu (2002) [73] points out that the power of a Savonius rotor is based on the shape of the blades.

Dincer and Zamfirescu (2011) [71] state that the benefit of the VAWT is that it does not need to be pointed in the direction of the wind, which it is suggested simplifies the design for this dissertation. In other words the actual design of the cups/blades is based on the need to use drag to generate torque due to the pressure difference between the concave and convex surfaces of the turbine cups or blades and the reaction forces of the deflected wind that is behind the convex surface. According to Dobrev and Massouh (2012) [69] the drag turbine rotor can operate in a range of wind speeds and operates at low tip speed ratio. Dobrev and Massouh (2012) also note that most of the useful torque was created by the convex side of the blade surface.

Another advantage of this simple design is that the rotor can be used in steady wind conditions or turbulent conditions, because there is a continual force on the cups - provided there is wind [71]. Mahmoud et al. (2012) [74] add that the Savonius rotor is

also a low cost device with the added advantage of simplicity of design for easy production.

Staudt (2010) [75] suggests that there are alternatives to the Savonius rotor including the Darrieus turbine, which was designed in 1931 as a high tip speed rotor for the production of electricity. The Darrieus design is aimed at increasing the blade velocity above the prevalent wind speed. This turbine is available as a curved blade or straight blade version. This turbine is available in two-blade or three-blade configuration. The Darrieus operates, as shown in Figure 2.2.

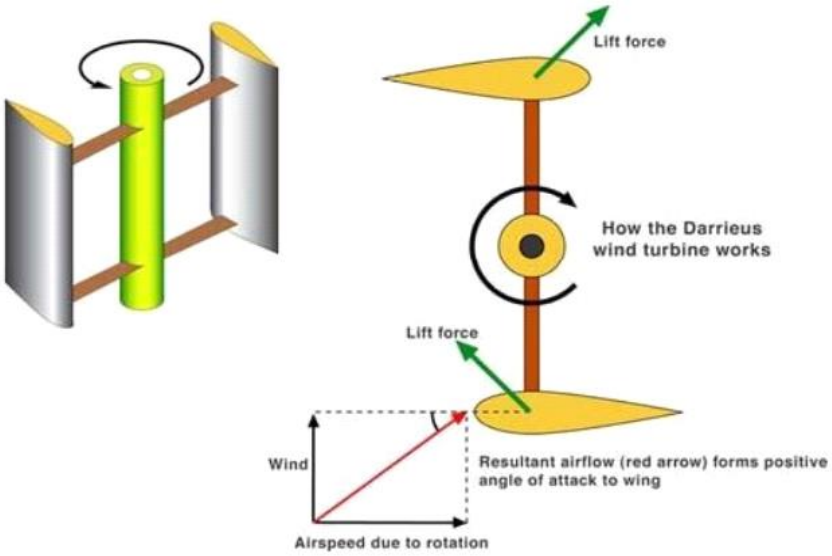

Figure 2.2 Darrieus Operating Principles [76].

This type of turbine is typically bigger than the Savonius. Staudt (2010) [75] points out that one of the drawbacks of this design is that it has very limited self-starting capacity because the design of the blades requires a degree of lift and can stall at low tip speeds. This indicates that the Darrieus is less versatile than the Savonius and it could also be

argued that the design is flimsy in comparison to the robust style of the Savonius. Therefore, the Savonius represents the preferred option for this study. This choice is supported by a number of studies conducted over the past three decades.

2.3.2 Performance of Savonius Drag Turbines

There have been several studies regarding the performance of Savonius drag turbines including a study by Modi and Fernando (1989) [77] cited by Staudt (2010) [75] which found that performance could be varied based on the number of blades and the geometric layout of the turbine. Another study by Ushiyama and Nagai (1988) [78] found that the coefficient of performance was related to the tip speed ratio and the bearing friction losses. It is noted, however, that these studies were ultimately designed to test the performance of the turbine with respect to energy production.

A study by Fujisawa and Gotoh (1994) [79] on the performance of a Savonius rotor measured pressure distributions on the surface of the two-blade rotor at varying rotor angles and tip-speed ratios. The study found that there was flow separation region on the blade surface which was linked to rotation and flow through the overlap. This flow separation contributes to the production of torque in the rotating rotor while the weakened flow through the overlap acts as resistance to the motion. The research concluded that the pressure distributions caused by the wind on a rotating rotor differ substantially from pressure distributions in a motionless rotor particularly on the convex side of what the researchers term the advancing blade. In other words a low pressure region is created by the moving 'wall effect' of the blade.

Dobrev and Massouh (2012) [69] cite various studies in which the flow of air around different blade configurations was tested, for example Nakajima et al. (2008) [80] examined the aerodynamic performance of different designs using pigment streak-line methods to enable visualisation of the flow about a single and two-stage Savonius rotor. Whereas particle image velocimetry (PIV) was used in a study by McWilliams and Johnson (2008) [81] to explore the flow around different Savonius models. This study indicated that there is considerable interaction between flow over the forward blade and the wake of the trailing blade.

2.3.3 Experimental Research on Savonius Rotors

The question is which rotor design is most suitable for progressing this study. Tong (2010) [68] points out that in choosing the number and shape of the blades it is essential to take into account that these blades rotate the velocity of the air relative to the blade "*changes in magnitude and direction*". Also, because of the blade layout, each blade is influenced by the wind from the wake of the blade ahead of it and from its own wake as it rotates downstream about the turbine axis. These factors mean that the blades are subjected to fluctuating aerodynamic forces which can lead to fatigue affecting cost, maintenance schedules and service life.

Morshed et al. (2013) [82] studied the performance of a three-blade Savonius turbine with the intention of improving performance of the rotor. These tests were conducted in a low speed wind tunnel and involved a series of semi-cylindrical three-bladed Savonius rotor scale models each with different overlap ratios. The study measured pressures around the concave and convex surfaces of each blade and static torque using

computational fluid dynamics (CFD) simulations to analyse the aerodynamics. The study found that blade overlap significantly affects performance and concluded that turbine models without overlap ratio have better aerodynamic performance.

Fujisawa (1992) [83] investigated the aerodynamic performance of Savonius rotors, testing different overlap ratios based on pressure distributions on the blades. The study also included visualisation of the flow fields in and around the rotors, with and without rotation. The study included tests on four rotors each with two semi-circular blades. The different between each test specimen was the overlap ratios which ranged from 0 to 0.5. Fujisawa (1992) [83] measured the static torque performance and found that torque improved by increasing the overlap ratio, particularly on the returning blade. This effect was attributed to the effect of pressure recovery by the flow through the overlap. The study found that torque and power performance of the rotating rotor achieved a maximum at an overlap ratio of 0.15. This effect was created by what Fujisawa (1992) [83] describes as the "*Coanda-like flow on the convex side of the advancing blade*", which is increased by flowing through the small overlap ratio. The study concluded that rotor performance deteriorates as the overlap ratio increases.

The review highlighted a number of studies on this issue. Dobrev and Massouh (2012) [69] conducted experiments on the aerodynamic performance of Savonius turbines. The tests were conducted in a closed circuit type wind. The tests involved a two-blade Savonius rotor with the following dimensions: 200mm high, 219.5mm in diameter, the blade making a circular arc of 180°, blade thickness 1mm, blade radius 57.5 mm, gap width between blades 11.5 mm and endplates having a diameter of 300 mm. The two-blade turbine was tested at a rotational speed varying from 800 rpm to 1000 rpm, with an

upstream speed of 9 m/s to 15 m/s. The study confirmed that the blade angle affects torque and that the angle of the blade also affects the wind flow between blades. The authors point out that the torque of the blade is caused by differential pressure applied on the convex and concave side. In this case, the blade torque is divided by the rotor torque averaged over one revolution and the results indicate that maximum useful torque is produced when the angular position of the blade is 27˚ and the minimum useful torque at 270˚. These experiments also provide useful data for replicating wind tunnel experiments for this thesis.

Blackwell et al. (1977) [84] conducted tests on Savonius drag turbines to assess and compare the aerodynamic performance of two-blade rotors with three-blade rotors. The tests involved Savonius type rotors of two/three stages and two/three blades at different Reynolds numbers. The measuring variables included torque, RPM and tunnel conditions. The study concluded that the performance of the two-blade rotor was superior to the three-blade in every respect, for example the power coefficient of the two -blade was 1.5 times of the three-blade, the speed ratio increases with the two blade design and the static torque is lower than the three blade design.

These findings are confirmed in a study conducted by Nasef et al. (2013) [85] who studied the aerodynamic performance of stationary and rotating Savonius rotors, testing various overlap ratios and different rotor angles ranging from 0º to 180 º. The study tested five rotors, with two semi-circular blades, but with different overlap ratios including 0, 0.15, 0.2, 0.3 and 0.5, with a Savonius model of 15cm diameter and 15 cm high. The test velocity ranged from 0 to 36 m/s. The study conclude that the static torque coefficient

improves by increasing the overlap ratio. This is particularly true on the returning blade because of pressure recovery effect by the flow through the overlap.

Mahmoud et al. (2012) [74] also conducted studies on different geometries of the Savonius wind turbines and found that, the two blades rotor were more efficient that three and four blade versions. In addition, the study also concluded that end plates on the rotor device were more efficient that rotors without end plates. The study also examined double stage rotors and found that these rotors have a higher performance than single stage rotors.

In summary, the Savonius models are simple shapes that are low cost and easy to manufacture. The drag turbine is available in various configurations from a two-blade style to four blade style. In addition the blades can be placed and shaped to vary the blade gap. The principle advantages of this drag turbine include the fact that it is self-starting, self-limiting and its maximum speed is dictated by wind speed, nor is it dependent on wind direction. A number of research studies were investigated and suggest that the aerodynamic performance of the rotor is dependent on the number of blades and the orientation and angle of the blades. These studies also indicate that rotor performance with respect to torque is dependent on the gap ratio between the rotor blades. A number of studies suggest that the performance of the two blade Savonius is superior to the three or four blade model. There is also a suggestion that the double stage version is superior to the single stage version. The review finds that models of the Savonius rotor can be tested in low speed wind tunnels. It is noted that the majority of research studies available have conducted experiments on the Savonius rotor to improve its performance in energy

production and, as such, these experiments tend to be conducted for relatively low speeds, whereas this study requires high speed to simulate aircraft landing conditions.

2.4. Wheel Aerodynamic Forces

In order to design the wind turbine, it is required to know how much torque is required to spin the aircraft wheel with respect to its weight and the aerodynamic forces. During the wheel rotation against wind, there are new forces created which should be considered.

Kothawala et al. (2013) [86] carried out a computational investigation of the combined effect of yaw, rotation and ground proximity on the aerodynamics of an isolated wheel using steady and unsteady Reynolds-Averaged Navier-Stokes (RANS & URANS). The diameter and width of the wheel was 0.416m and 0.191m respectively. They tested the rotated wheel against a free stream of air with speeds of 70 and 98 m/s. The wheel rotation speeds were 100, 200, and 327 rad/sec. However, they conclude that the wake on rear of wheel increases with increased rotation speeds.

Morelli (1969) [87] tested a stationary and rotated wheel against the same wind speed using a wind tunnel. He found that the drag is increased by about 10% when the wheel is rotating. He concluded that this increase of drag was due to negative lift and induced drag.

Rahman (1996) [88] carried out a computational study on flow around a rotating short cylinder in order to study the effect of rotation on the aerodynamics forces. The cylinder considered is in X-Y plane, the rotation is about the Z axis, and the flow is along the positive x - direction. He found that the clockwise rotation of the cylinder reduced the pressure region above the cylinder with higher pressure at the bottom surface. The

difference in pressure producing an upward lift force for clockwise rotation and vice versa for anticlockwise. Also, the lift force is dependent on the cylinder spin ratio, an increase in the rotational velocity producing an increasing lift force.

To sum up, there is a lift force acting on a rotating wheel which depends on the direction of rotation. In our case, the lift force is downward, which increases the load on the wheel. Also, the rotational (side) drag force increases the wheel's resistance to spin.

Chapter 3

3. The Prevention of Tyre Overheating by Pre-rotating the Wheel

3.1. Introduction

As described in the thesis introduction, at landing impact, tyre sliding occurs and then it spins-up to reach aircraft forward speed. High tyre slip generates heat, which is enough to melt a thin layer of the tread rubber. Melted rubber became weak as its material bonds linkage is broken when the critical temperature is exceeded [2]. One-third of the eroded rubber burnt off under the skidding tyre vaporizes in the form of smoke, while the remaining eroded rubber adheres to the runway [3]. However, the tyre temperature and wear rises up as slip increases. Therefore, the skidding wheel distance and time are major factors of tyre temperature and wear [4].

Pre-spinning the wheel is the proposed solution to the elimination of aircraft landing smoke caused by high tyre tread temperature during touchdown [9-28]. In this chapter, a case study of the aircraft's main landing gear has been simulated for a single wheel, using a coupled structural – thermal transient analysis in ANSYS to estimate the tyre tread temperature for a typical landing and for when wheels are pre-spun, in order to validate the technique of pre-spinning the wheel; and to calculate how much pre-rotation is enough to avoid aircraft landing smoke.

In this chapter, the first objective is to succeed in reducing the tyre tread temperature below the rubber melting point level. The tread rubber is expected to not smoke if its temperature remains below its critical temperature. The aircraft tyre tread is always made of natural rubber [4]. The natural rubber melting point is at about 200 ˚C [2, 5]. The second objective is to find the optimal pre-rotation speed that will prevent the tyre overheating and thus producing smoke.

In this model, the wheel touches down with vertical and horizontal speeds as in a real landing. The wheel is connecting to the body structure by a shock absorber to give damping force versus time. However, the input data includes assumptions that are used for all simulations are similar in order to get a fair comparison of results.

3.2. Modelling and Simulation

The following assumptions were made in order to simplify the model and because the evaluation includes constructing the same underlying assumptions for all wheel statuses. First, after touchdown, the pilot does not use brakes in order to prevent the wheels from extra skidding [89]. Further, constant horizontal speed was used, and the aircraft will land with all of the main wheels and zero wing lift [90, 91]. Moreover, the maximum aircraft landing weight was used. Also, roughly two seconds after the main wheels land, the nose wheel will touch the ground [34]. Therefore, the aircraft weight is divided by the number of rear wheels only.

3.2.1 Aircraft Speed

The aircraft case study in this thesis is the Boeing 747-400. The horizontal speed at landing is equal to the approach speed of the Boeing 747-400, 80.78 m/s [92], minus 5.14

m/s from a decrease in speed caused by the flare [34]. This results in a horizontal touchdown speed of 75.6 m/s.

The vertical sink rate at the moment of landing for the Boeing 747-400 aircraft usually fluctuates between 1.5 m/s and 3 m/s [90]. A sink rate of 2.5 m/s is used at the beginning of each landing simulation in this study. Moreover, two different horizontal speeds of 60 m/s and 90 m/s are used to check the effect of horizontal speed on the tyre tread temperature; for the same purpose, the sink rate values of 1 m/s and 5 m/s have been used.

3.2.2 Landing Gear Dynamics

The simple mass-spring-damper is modelled using the ANSYS mechanical transient as shown in Figure 3.1.

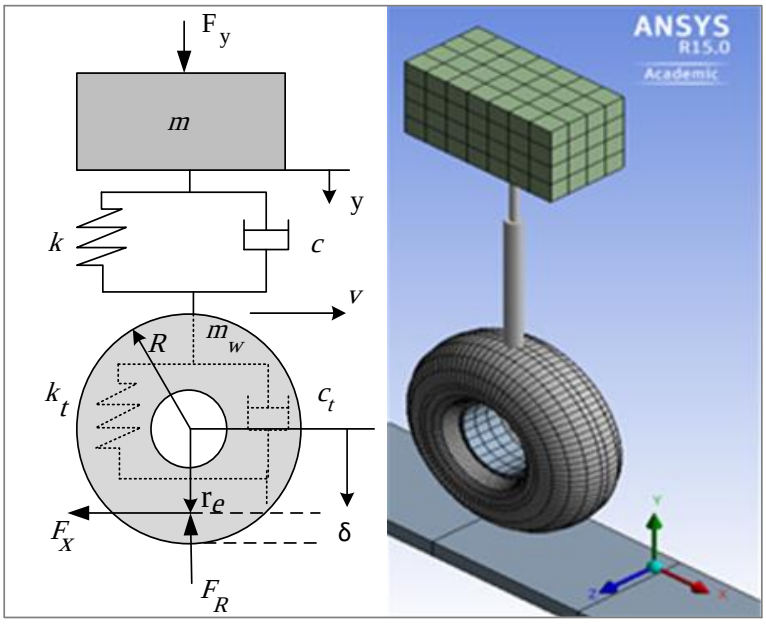

Figure 3.1 Mass-spring-damper system (left) and ANSYS model (right).

F_y is equal to the weight applied on the shock absorber because zero lift is assumed at touchdown [93, 94]. Balancing forces vertically, the equation representing oscillation of the vehicle mass in Figure 3.1 is:

$$F_y = m\ddot{y} + c\dot{y} + ky \tag{3.1}$$

The lumped mass vertical displacement, y has an initial value equal to zero at the moment of touchdown.

For this model, further assumptions are taken into consideration: the tyre is always in contact with the runway surface, the system is under-damped, the initial vertical velocity of the wheel axle mass is zero, ($\dot{\delta}(0) = 0$), and in the initial state, both springs are un-deformed, $y(0) = 0$, $\delta(0) = 0$.

The equation of motion should be written as [95]:

$$\begin{bmatrix} m & 0 \\ 0 & m_w \end{bmatrix} \begin{Bmatrix} \ddot{y} \\ \ddot{\delta} \end{Bmatrix} + \begin{bmatrix} c & -c \\ -c & (c_t + c) \end{bmatrix} \begin{Bmatrix} \dot{y} \\ \dot{\delta} \end{Bmatrix} + \begin{bmatrix} k & -k \\ -k & (k_t + k) \end{bmatrix} \begin{Bmatrix} y \\ \delta \end{Bmatrix} = \begin{Bmatrix} F_y \\ 0 \end{Bmatrix} \tag{3.2}$$

In our case study, the wheel mass, m_w is very small compared to the total mass applying on the wheel (aircraft mass), m, so m_w can be considered as zero in mathematical calculations.

The reaction force, F_R acts vertically on the tyre contact patch which is equal to the aircraft mass. The tyre damping coefficient, c_t multiplied by the tyre deflection rate, $\dot{\delta}$ plus the tyre linear stiffness, k_t multiplied by the amount of tyre deflection δ, are also equal to the reaction force, and can be written as:

$$F_R = c_t\dot{\delta} + k_t\delta \tag{3.3}$$

In a static condition, the tyre deflection rate $\dot{\delta}$ is equal to zero. So, $F_R = k_t\delta$. From this relationship, we can chose the proper stiffness for the tyre material and the proper inflation pressure to control the vertical tyre deflection ($k_t = 1{,}751{,}268$ N/m and $c_t = 22$ Ns/m) [96]. Solving Eq. (3.2) for y and δ, using the initial conditions mentioned in the assumptions would give a solution that could be used for determining its first derivative. Including expressions for the final solution for $\dot{\delta}(t)$ and $\delta(t)$ in Eq. (3.3) would give an expression for change of reaction force in time $F_R(t)$. In this equation, aircraft weight should be included, which applies static force on the system. After sufficient time, the final reaction force over the tyre contact patches will be equal to the downward force reacting on the landing gear structure: $F_R = F_y, \ (t \to \infty)$.

For contact friction, a simple Coulomb friction model is used to calculate the friction force, F_x to be:

$$F_x = \mu F_R \tag{3.4}$$

where, μ is the friction coefficient.

3.2.3 Wheel Translational and Rotational Dynamic

The wheels are assumed to start to spin up from zero rotational speed when the aircraft lands until they reach the aircraft forward speed, and then decelerate as the aircraft decelerates. Figure 3.2 shows the rigid wheel forces at the moment of touchdown (t = 0). The wheel radius, *R*, will deflect under the aircraft weight to become the deflection radius, r_d. The amount of the deflection is $\delta\ (= DB)$. The arc ADC will be the tyre footprint ABC when it is compressed. The vertical force acting downwards on a single wheel is F_y. That force gives rise to an immediate friction force F_x. The aircraft landing

speed on the runway, *v*, and the angular displacement of the wheel, ∅, are shown. Geometric relationships are given below.

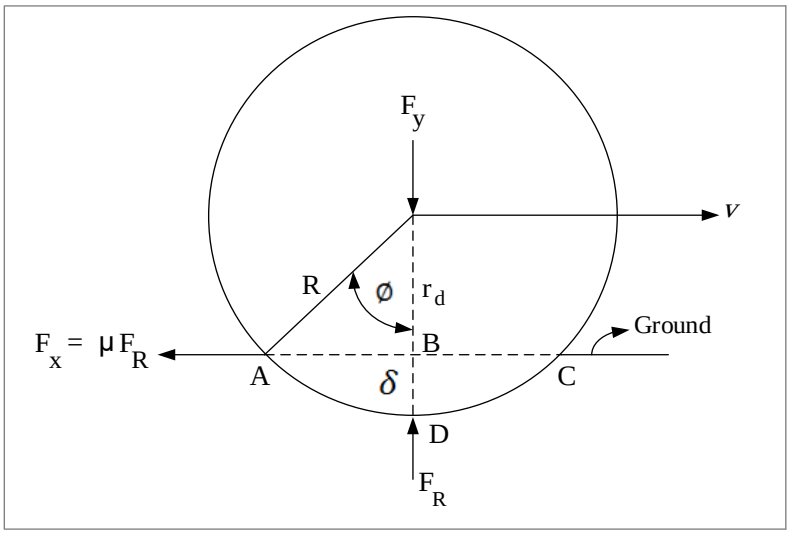

Figure 3.2 The forces on wheel in contact with runway, modified and redrawn from [97].

The tyre deflection shown in Figure 3.2 is defined by:

$$\delta = R - r_d \tag{3.5}$$

If there was enough slip across the extent of the tyre contact patch then the tyre might rotate as if the true radius were the geometric value of the axle height r_d. However, the effective radius of the wheel under the immediate loading conditions should be used. From trigonometry, the angle between the initial and final positions (angular displacement) of a wheel is:

$$\emptyset = sin^{-1}\frac{\sqrt{R^2 - r_d{}^2}}{R} \tag{3.6}$$

and horizontal translation of rolling is:

$$AB = \sqrt{R^2 - r_d{}^2} \tag{3.7}$$

Combining Eq. (3.6) with Eq. (3.7) yields the effective rolling radius:

$$r_e = \frac{AB}{\emptyset} = \frac{\sqrt{\mathrm{R}^2 - \mathrm{r}_d{}^2}}{sin^{-1}\frac{\sqrt{R^2 - r_d{}^2}}{R}} = \frac{R\sqrt{1 - \frac{\mathrm{r}_d{}^2}{\mathrm{R}^2}}}{\sin^{-1}\sqrt{1 - \frac{\mathrm{r}_d{}^2}{\mathrm{R}^2}}} \tag{3.8}$$

The proof by Benjamin and Dexter (1954) [97] concludes that the right-hand side of Eq. (3.8) is closely approximated by the linear function $\frac{2R + r_d}{3}$, so that:

$$r_e \approx \frac{2R + r_d}{3} \tag{3.9}$$

or, since $r_d = R - \delta$ from (3.5), the radial tyres deflection formula will be as [98]:

$$r_e = R - \frac{\delta}{3} \tag{3.10}$$

The friction force, F_x is distanced from the wheel's axle by the effective radius. Utilizing the rotational form of Newton's 2nd law with respect to the wheel moment of inertia I, rotational acceleration of the wheel will be:

$$\dot{\omega} = \frac{F_x r_e}{I} \tag{3.11}$$

Wheel speed, ω with time is simply calculated as the integral of Eq. (3.11) with respect to time, plus an initial wheel velocity, ω_i :

$$\omega = \int_{t_0}^{t_f} \dot{\omega}\, dt + \omega_i \tag{3.12}$$

where, t_0 and t_f are the initial and final time interval respectively, ($t_0 = 0$, and $t_f = 0.2$ seconds).

Figure 3.3 describes four stages of wheel behaviour at touchdown within a fraction of a second, which is a combination of translational and rotational motion.

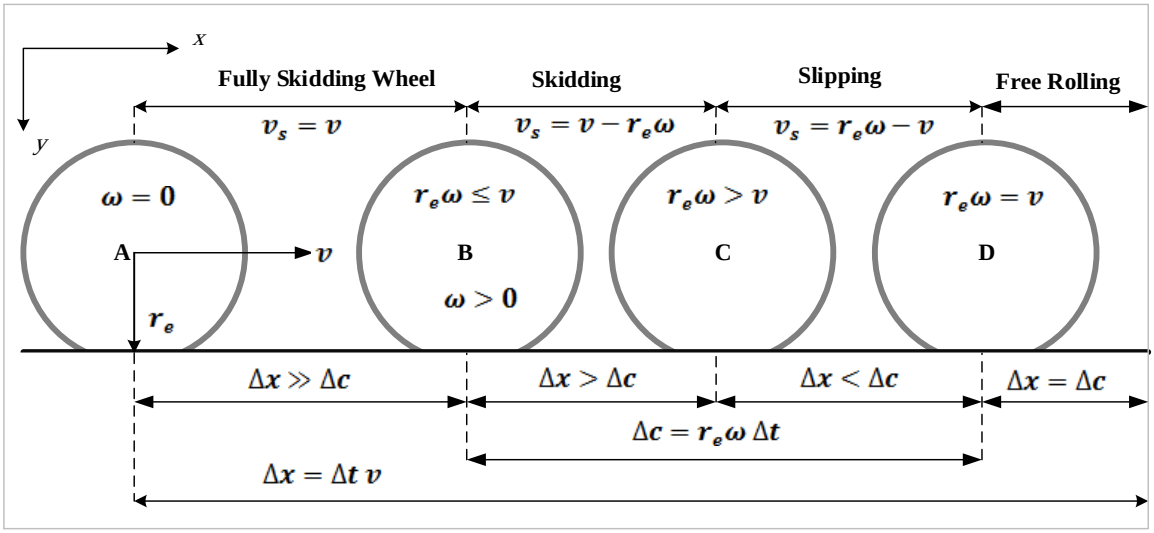

Figure 3.3 Four stages of wheel behaviour at touchdown within a fraction of second.

At position A, the wheel just landed and it is at full skid, $\omega = 0$, and then it will slide for distance Δx to position B. We can calculate the distance, Δx at any position by knowing the skidding time because v is assumed constant ($\Delta x = \Delta t\ v$).

From position A to B, the tyre contact patch will not change, so the circumference of the tyre's sliding distance (Δc) at contact with the runway is just the tyre contact patch. Thus, $\Delta x \gg \Delta c$, and the relative velocity between a point tangential to the outer tyre surface "skidding speed, v_s" is equal to the forward speed of the aircraft, v:

$$v_s = v \tag{3.13}$$

The second stage is the spin-up phase which begins when the wheel starts to spin-up from position B as it is affected by a high friction force, F_x, to reach the free rolling level at position C. In this stage, $\omega > 0$, $r_e\omega \leq v$, $\Delta x > \Delta c$, and the skidding speed is:

$$v_s = v - r_e\omega \tag{3.14}$$

The third stage is between the positions C and D, which is referred to as slipping. At this stage, the wheel is already rolling and towed by the aircraft structure to match its forward speed; at the same time, the shock absorber and the tyre are fully compressed, which means less wheel effective radius (torque arm). Also, the friction force between the tyre and runway has reached its peak value, therefore, the wheel's angular velocity has increased suddenly to be higher than the free rolling level, $r_e\omega > v$ and therefore, the tyre's circumference distance is higher than the forward distance of aircraft $\Delta x < \Delta c$. In this case, the skidding speed will be:

$$v_s = r_e\omega - v \tag{3.15}$$

At the fourth stage, the wheel is settled down to the free rolling level after position D to the end of the runway. However, the longitudinal wheel slip ratio, λ, is defined as:

$$\lambda = \frac{v_s}{v} \tag{3.16}$$

Substituting Eq. (3.13), Eq. (3.14), and Eq. (3.15) in Eq. (3.16) to present different wheel slippage behaviour [99]:

$$\lambda = \begin{Bmatrix} \frac{v}{v} = 1 & \text{if} & \omega = 0 & \text{(fully skidding wheel)} \\ \frac{v - r_e\omega}{v} & \text{if} & r_e\omega \le v & \text{(skidding)} \\ \frac{r_e\omega - v}{v} & \text{if} & r_e\omega > v & \text{(slipping)} \end{Bmatrix} \tag{3.17}$$

The distance, Δx presented in Figure 3.3 is the distance covered by the wheel in both cases; skidding and free rolling. It is valid to calculate the skidding distance as the aircraft forward speed is assumed constant, but the exact skid distance is a function of the skidding speed which can be defined as:

$$S_D = \Delta t \, \Delta v_s \tag{3.18}$$

Because the aircraft forward speed, v is constant during this simulation, once we calculate the skid distance, S_D, simply the skidding time will be:

$$t_s = \frac{S_D}{v} \tag{3.19}$$

At a high slip ratio, the tyre's temperature at its contact surface becomes higher and the friction coefficient becomes lower. However, the landing speed has a larger effect on the friction coefficient than the temperature [100].

Burckhardt's friction model is used to estimate the tyre runway friction coefficient μ. Burckhardt's model is a function of longitudinal wheel slip, λ and aircraft horizontal ground speed, v which are defined as [101]:

$$\mu(v, \lambda) = [C_1\left(1 - e^{-C_2\lambda}\right) - C_3\lambda]e^{-C_4\lambda\, v} \tag{3.20}$$

where, C_1 is the friction curve maximum value, C_2 is the friction curve shape, C_3 is the difference between the maximum value at $\lambda = 1$ and the maximum value of the friction curve, and C_4 is in the range of $0.02 - 0.04$ s/m.

In this thesis, we are using the dry concrete parameters which are: $C_1 = 1.2801$, $C_2 = 23.99$, $C_3 = 0.52$, and we assume $C_4 = 0.03$ s/m.

Figure 3.4 shows $\mu - \lambda$ curves with different horizontal touchdown speeds.

In this simulation model, constant friction coefficient of 0.7, 0.65, and 0.6 were used for the speeds of 60 m/s, 75.6 m/s, and 90 m/s respectively. These are based on the range of values at $\lambda = 0.05 - 0.15$, which many manufactures use [101].

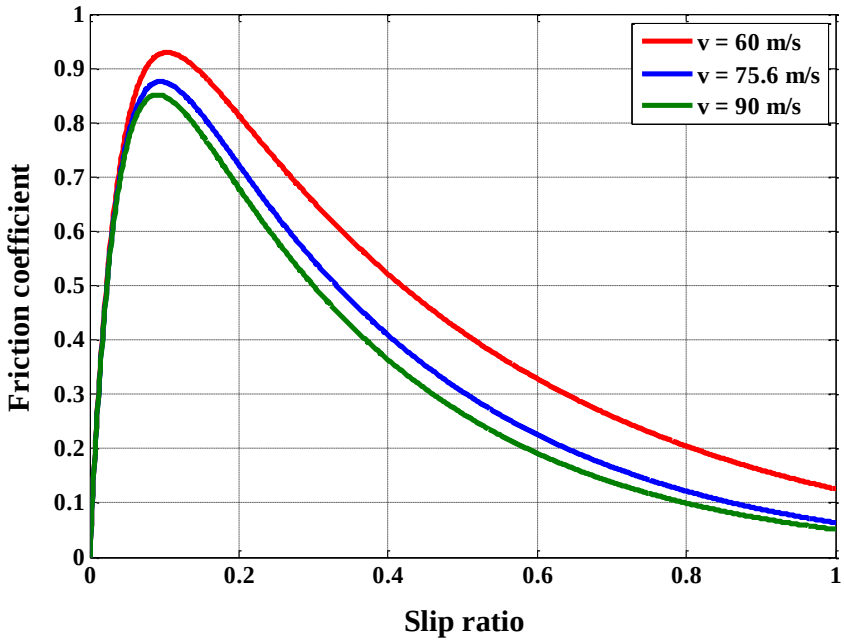

Figure 3.4 Relationship between μ and λ at different horizontal landing speeds.

3.2.4 Tyre Heat Generation

There are two ways that heat is generated by tyres: a friction phenomenon caused by sliding the tyre under a heavy load and the stress deformation cycle. In this thesis, we focus on sliding friction, which is very high compared with other sources.

At landing impact, the tyre is sliding similar to a block of rubber under a vertical force on the same contact area. This leads to very high heat produced by friction power, in this case, the heat flux, q is defined as:

$$q = \frac{F_x v_s}{A_c} \tag{3.21}$$

Where, A_c is the tyre contact area (m^2), which is constant at a fully skidding wheel and then starts to change [102]. Boeing provides a formula to calculate the tyre contact area.

This is done by dividing the load per tyre by the tyre inflation pressure. The tyre footprint area is a 1.6 ellipse (the major axis is 1.6 times the minor axis) to be calculated as:

minor axis $= 0.894\sqrt{A_c}$, and then the major axis $= 1.6$ x minor axis [103].

Once the tyre starts to spin-up, the contact area will be changed to a new contact area that is not heated yet, and the slip ratio becomes less, which means less heating for the new tyre area. Moreover, the initial contact area, which already has been heated to the maximum temperature level, will decrease in temperature as it comes in contact with the new "cold" runway area and cool air. This means that the maximum tyre tread temperature will only occur on the initial contact surface while the wheel is fully skidding [64]. Moreover, Eq. (3.21) is the total heat flux and part of this thermal power will transfer to the tyre and part will transfer to the runway. Therefore, a partition coefficient, P_c should be used to multiply by the heat flux equation. The partition coefficient is governed by the thermal conductivities and diffusivities of the tyre, k_t , α_t and runway, k_r , α_r respectively and it can be written as [102]:

$$P_c = \frac{\mathrm{k}_t}{\mathrm{k}_r}\sqrt{\frac{\alpha_r}{\alpha_t}} \tag{3.22}$$

Thermal diffusivity, α can be expressed with respect to the material density, ρ ; thermal conductivity, k ; and the specific heat, c_v to be as:

$$\alpha = \frac{\mathrm{k}}{\rho\, c_v} \tag{3.23}$$

Because all heat flux parameters are functions of time, by adding the partition coefficient in Eq. (3.22) to Eq. (3.21), the tyre heat flux becomes as follows:

$$q_t = P_c \int \left(\frac{1}{A_c} F_x \, v_s \right) dt \tag{3.24}$$

A theoretical model for tyre tread heat flux generated at contact with the runway is attached as Appendix A.

3.2.5 Simulation Setup

The overall view of the simulation model is shown by Figure 3.5. The landing gear will touchdown on the runway with vertical and horizontal speeds, which simulates the typical aircraft landing.

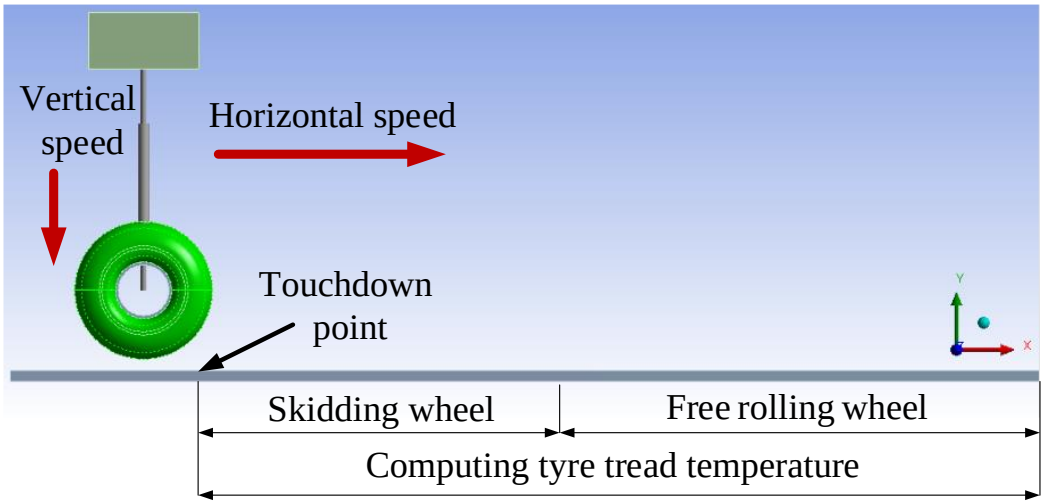

Figure 3.5 Overall view of the simulation model (not to scale).

In a typical aircraft landing, the wheel is supposed to be fully skidding and spun-up to reach a free rolling level within a fraction of a second. The simulation model will compute the tyre tread temperature from the moment of touchdown until the end of the simulation. The same model will run with the wheel initially static (normal landing), with a pre-spun wheel, and at different landing speeds.

The model consists of five parts: the tyre, the rim, the shock absorber, the weight box, and the runway as shown in Figure 3.6.

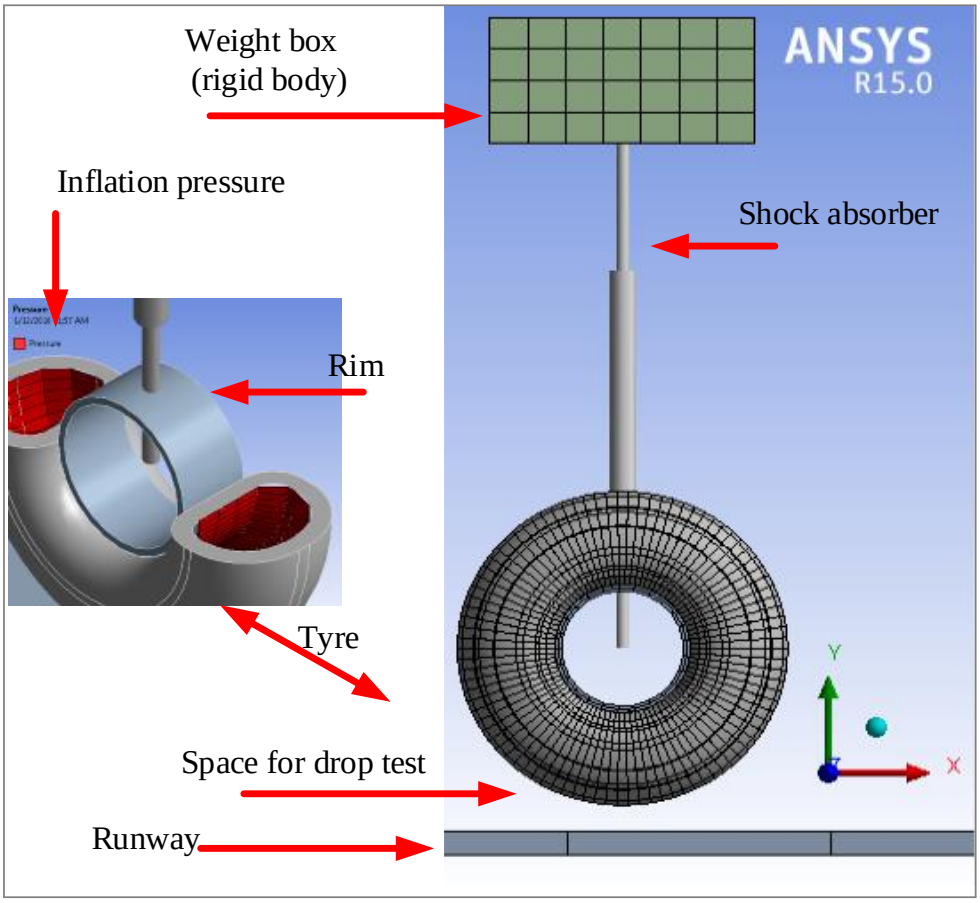

Figure 3.6 Geometry of parts: tyre, shock absorber, weight box, rim, and runway.

Using ANSYS design modeler, the tyre has been modelled as one material (rubber) because the goal of this project is to estimate temperature on the first layer of the tyre tread only. The 5180 nodes and 2286 elements are used to mesh the tyre and it was filled to 1.482 $x10^6$ Pa. The rim has been added to the tyre to control its weight by increasing or decreasing its density to obtain the correct wheel mass.

A shock absorber has been connected from the centre of the rim to the weight box. Its position is vertical to avoid any cornering, it has the same properties as a Boeing 747-400 shock absorber and is valid for a single wheel ($k = 3.12x10^5$N/m and $c = 3.42x10^5$ Ns/m) [90].

The weight being applied on the wheel is 18484 kg, which is found by taking the maximum landing weight of a Boeing 747-400, which is 295,743 kg [92] divided by 16 (number of rear wheels). Finally, the runway is designed to be long enough to complete the simulation. The runway is modelled as being of concrete material with a flat surface, and no texture.

ANSYS mechanical transient software can simulate the dynamic behaviour, but to find the heat flux generated by friction, we have to use a coupled field structural-thermal analysis. In this case, we are supposed to use elements that support combined structural-thermal. ANSYS provides several solid elements that have these properties. "Solid226" is used for this model by applying the command APDL (ANSYS Parametric Design Language) for the tyre and runway contact surfaces. The users defined results of "TEMP" and "OMGZ" were chosen for tread temperature and wheel angular velocity respectively.

A coupled structural – thermal transient analysis in ANSYS uses this formula to find the total generated heat:

$$q = (FHTG)\,\tau\,v_s \tag{3.25}$$

where, $FHTG$ is the fraction of frictional dissipated energy converted into heat and is called the "frictional heating factor"; τ is the equivalent frictional stress, and v_s is the

sliding speed. ANSYS uses 1 as a default value for $FHTG$, which is used in this simulation.

The amount of heat flux going up to the tyre and down to the runway is governed by these equations:

$$q_c = (FWGT)(FHTG)\,\tau\,v_s \tag{3.26}$$

$$q_T = (1 - FWGT)(FHTG)\,\tau\,v_s \tag{3.27}$$

where, q_c is the heat flux of the contact surface, which is the runway, q_T is the heat flux of the target surface, which is the tyre, and $FWGT$ is the weight factor which controls the distribution of heat flux between the two surfaces. ANSYS uses 0.5 as a default value for $FWGT$ [104]. In this simulation, it is assumed that 90% of heat flux is going up to the tyre and 10% is going to the runway. In this case, $FWGT$ is set to be 0.10.

At frictional contact between the tyre and runway, the simulation provides the forces for every time step. During transient analysis in each time step, there is a small increment of wheel sliding or angular displacements applied, so it is important to apply a small time step ($dt = 1x10^{-6}sec$).

Table 3.1 shows the 3D main landing gear wheel geometry data. The tyre rubber is hyper-elastic material, which is available in the ANSYS software as standard material model.

Table 3.1 Wheel geometry data [105].

	Weight (kg) [106]	Diameter (mm)	Width (mm)
Tyre	110	1244.6	482.6
Rim	74.4	510	457.2

Table 3.2 shows the tyre tread material properties. Mooney- Rivlin material model has been considered because the tyre tread contains a rubber compound with available constants. The material constants defined for Mooney – Rivlin model is supported with the stress versus strain curve for the material, which helps to capture the failure behaviour of the tyre.

Table 3.1 Material parameters of tyre tread [65].

Properties	Value
Passion's ratio	0.49
Mass density ($\mathbf{kg/m^3}$)	1125
Mooney Rivlin constants (Mpa)	$C_{10} = 0.643$, $C_{01} = 0.824$
Thermal conductivity ($\mathbf{W/m\ K}$)	1900
Specific heat ($\mathbf{J/kg\ K}$)	0.2

3.2.6 Simulation Process

The main process of the simulation model is shown in Figure 3.7. The simulation begins with the input data in the form of variables and constants.

In this model, there are two steps of calculation for each iteration. The first step is the mechanical analysis of the wheel's dynamic behaviour and the forces generated at the tyre's contact with the runway. In this step, everything needed to calculate the friction power (Eq. 3.21) is done; i.e. the friction force, the wheel skidding speed and the tyre contact area are calculated.

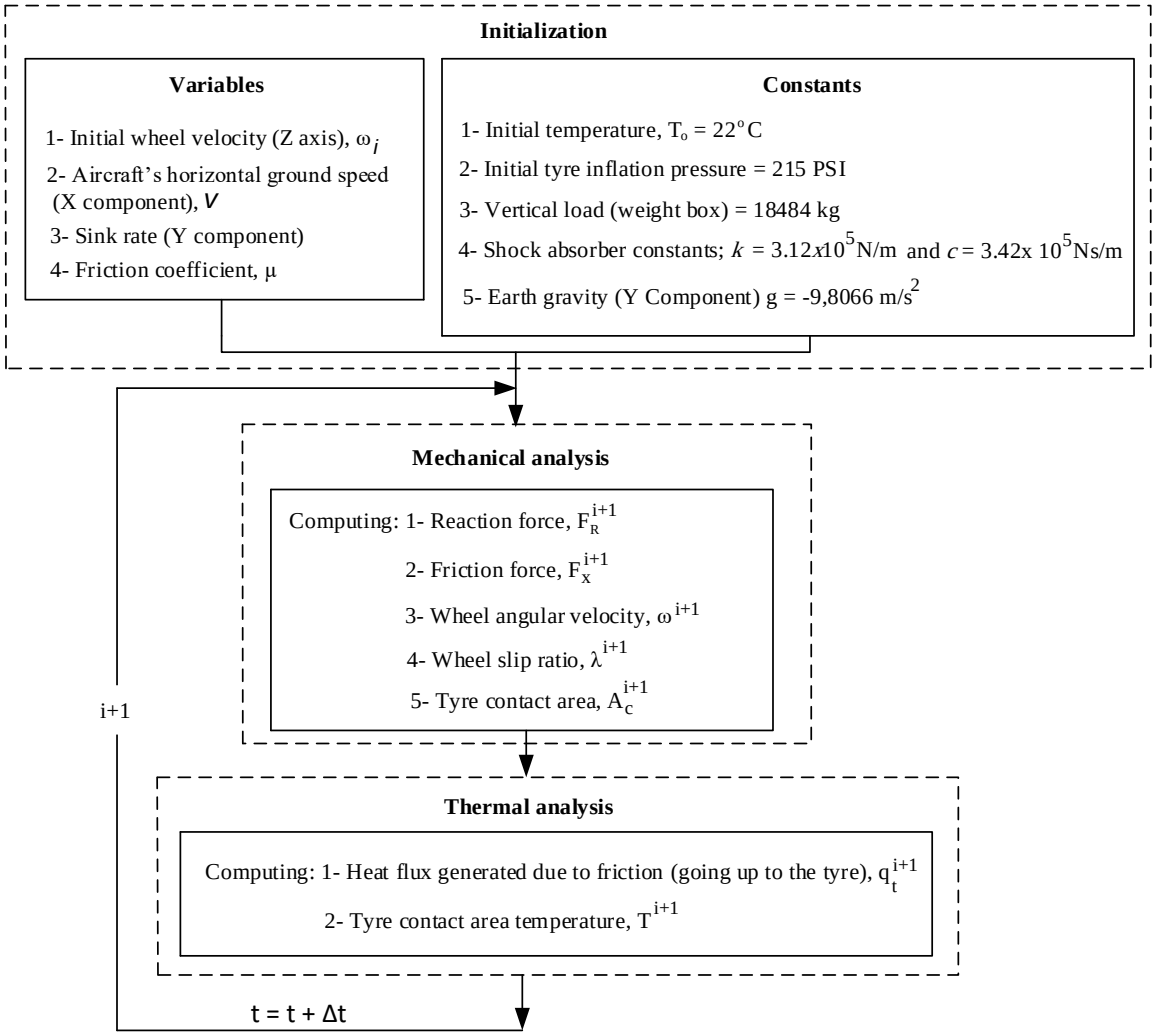

Figure 3.7 Simulation process for every iteration.

The second step is the thermal analysis; where the total heat flux generated between the tyre and runway and then the amount of heat flux that is going up to the tyre is calculated. Finally, the tyre tread contact temperature is calculated, and the process repeated for every time step.

Figure 3.8 shows the outline of the simulation model with some comments. The outline shows the main three sections; geometry, transient and solution. Here, the most important procedures are explained.

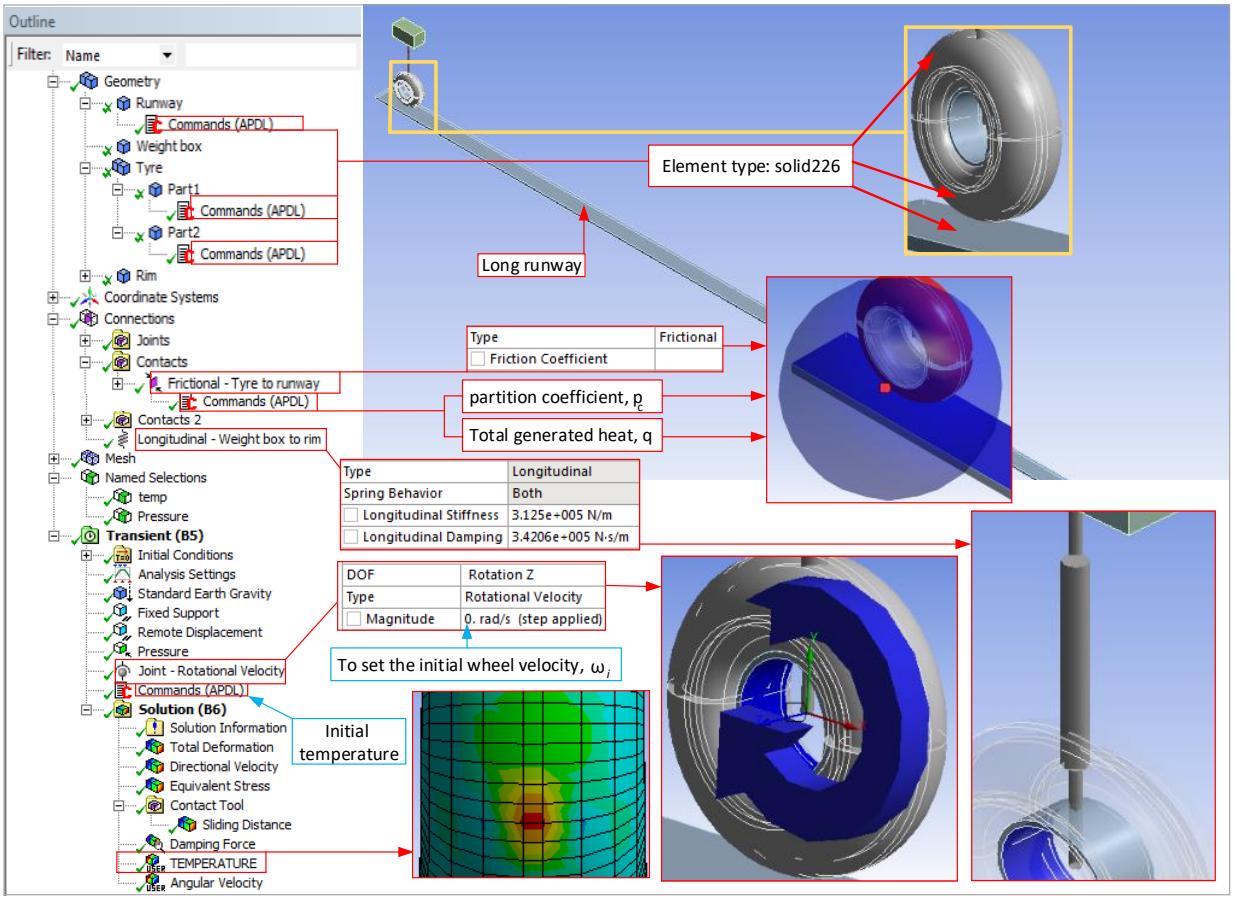

Figure 3.8 Outline of the simulation model.

In ANSYS, only certain combinations of elements can be used. Therefore, the element ‘solid226’ has been used for the tyre and runway to allow coupling structural-thermal analysis as it has a thermal degree of freedom**.**

The analysis has been done by using APDL (ANSYS Parametric Design Language) commands. ANSYS provides many codes (APDL) for different purposes with the option of changing the command by editing the code if required.

In the contact region between the tyre and runway, the friction coefficient is applied and also there are two commands; one for calculating the total heat flux generated due to friction (Eq. 3.21) and the other command is to control the amount of heat flux that is going up to the tyre, which is the partition coefficient (Eq. 3.22).

In the transient section, the initial conditions (horizontal speed and sink rate), analysis setting (controls of step, solver, nonlinear, and damping plus analysis data management) and the initial wheel velocity (direct input shown as 'joint-rotational velocity') are all shown. The temperature is set at 22 ˚C for all the simulations as an APDL command.

In the solution section, we can find all required results. For example, by using the user defined result 'TEMP' with the chosen tyre tread surface, the solver will calculate the tyre tread temperature. The same procedure is used to calculate the wheel angular velocity around a z axis; by using the user defined result 'OMGZ' for the wheel geometry.

3.2.7 Simulation Information

The simulation was run seven times with different initial conditions and for the same requirements. The simulations were as follows:

1. Static wheel: the wheel is static before touchdown (typical aircraft landing). This is to find the tyre tread temperature and wheel behaviour for a typical aircraft landing. Also, this identifies the free rolling angular velocity of the wheel in order to set the 50% and 100% pre-rotated wheel for the 2nd and 3rd simulations respectively.
2. 50% pre-rotated wheel: the wheel is pre-rotated to 50% of its free rolling angular velocity on the runway (based on the results from the 1st simulation). With this simulation, it is possible to check the reduction of tyre tread temperature that can be achieved.
3. 100% pre-rotated wheel: this is similar to the 2nd simulation, only the wheel is 100% rotated before touchdown instead of 50% to compare the results.
4. High landing speed: the horizontal landing speed is increased from 75.6 to 90 m/s to check the effect of a high landing speed on the tyre tread temperature.
5. Slow landing speed: the horizontal landing speed is decreased from 75.6 to 60 m/s for the same purpose as in the 4th simulation.
6. Hard landing: the vertical speed is increased from 2.5 to 5 m/s to check the effect of hard landing on the tyre tread temperature.
7. Soft landing: the vertical speed is decreased from 2.5 to 1 m/s for the same purpose as in the 6th simulation.

3.2.7.1 Boundary and Initial Conditions

The boundary and initial conditions for the simulations are presented in Table 3.

Table 3.3 Boundary and initial conditions.

	Wheel initially static	50% pre-rotated wheel	100% pre-rotated wheel	High speed landing	Low speed landing	Soft landing*	Hard landing**
Initial wheel velocity, ω_i (rad/sec)	0.0	60.5	121	0.0	0.0	0.0	0.0
Initial temperature (˚C)	22	22	22	22	22	22	22
Horizontal landing speed, v (m/s)	75.6	75.6	75.6	90	60	75.6	75.6
Vertical landing speed (m/s)	2.5	2.5	2.5	2.5	2.5	1	5
Initial time step (sec)	$1x10^{-4}$	$1x10^{-4}$	$1x10^{-4}$	$1x10^{-4}$	$1x10^{-4}$	$1x10^{-4}$	$1x10^{-4}$
Minimum time step (sec)	$1x10^{-6}$	$1x10^{-6}$	$1x10^{-6}$	$1x10^{-6}$	$1x10^{-6}$	$1x10^{-6}$	$1x10^{-6}$
Maximum time step (sec)	0.1	0.1	0.1	0.1	0.1	0.1	0.1
Step end time (sec)	0.2	0.2	0.2	0.2	0.2	0.2	0.2
Friction coefficient, μ	0.65	0.65	0.65	0.6	0.7	0.65	0.65

* Low vertical speed landing, ** High vertical speed landing

3.2.7.2 Solution Convergence

ANSYS simulation uses the Newton-Raphson method for nonlinear problems. This method is based on an iteration process which continues until the solution is converged. The convergence procedure is as follows: the simulation determines the criterion force which has a small value, resulting in negligible error. The difference between external and internal loads is called ‘residual’ or ‘convergence’ force; the simulation is repeated until the residual becomes less than the criterion for the sub-step to be converged. Moreover, ANSYS has recovery to help the problem to converge such as load stepping and bisection [107].

In ANSYS, the solver output provides a force convergence graph to monitor the progress. The simulation results are checked carefully. Figure 3.9 shows the force convergence status of the first simulation.

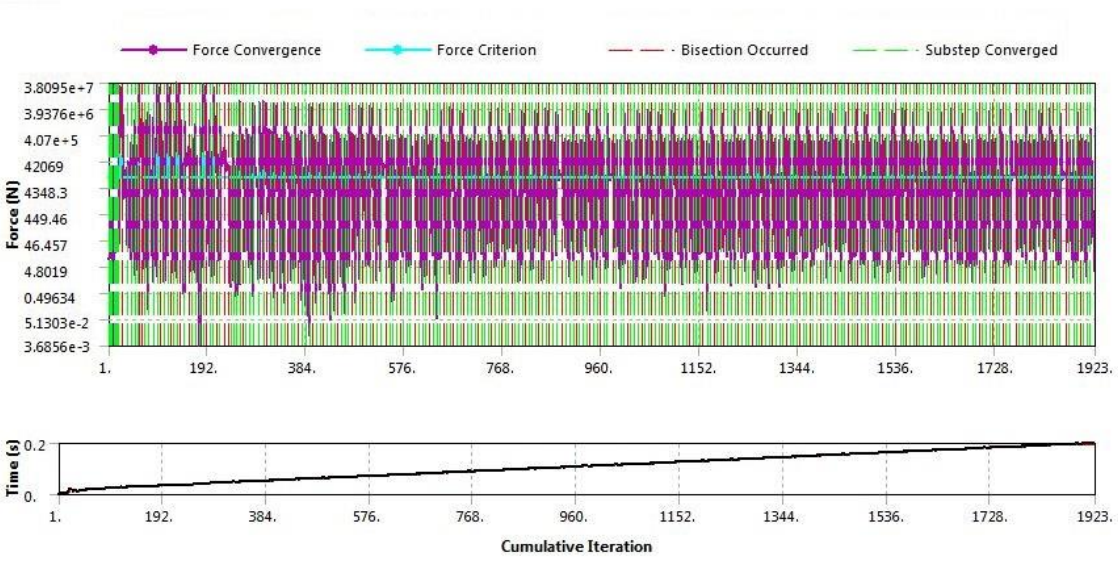

Figure 3.9 Force convergence and time vs. cumulative iteration.

All the simulations show approximately the same convergence status. As shown, a very good force convergence occurred at the beginning of the simulation, and then some bisections occurred, which resulted in a good force convergence rate.

3.3. Results and Discussion

3.3.1 An Initial Verification

For an initial check of the temperature results, we simulated the tyre sliding on the runway without its shock absorber or box weight, and we applied 250 kN vertically on the rim using a constant friction coefficient of 0.65. The speed was set at 13.89 m/s ($50 km/hr$) in order to capture the temperature after 4m of sliding distance.

Figure 3.10 shows the tyre force and a temperature profile of 186.4 ˚C, which is in very good agreement with an error of only 2.36% compared with a temperature value of 190.9 ˚C, which was achieved by Kondé et al. (2013) [63] in their experiment.

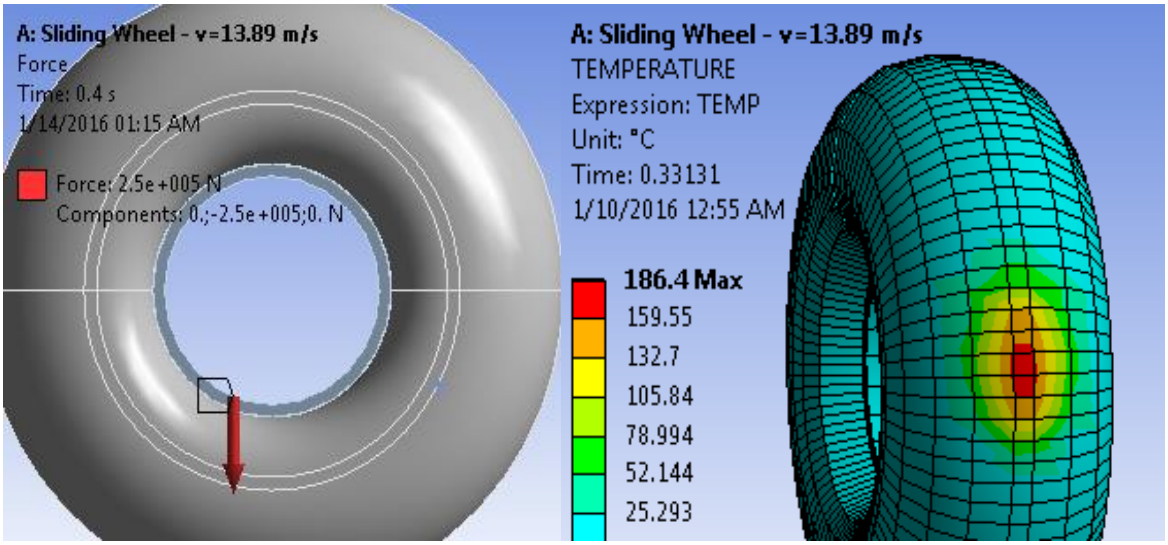

Figure 3.10 Pure sliding tyre force and temperature profile.

3.3.2 Wheel Dynamic Behaviour

From first simulation for the static wheel with $\omega_i = 0$, we obtained the wheel free-rolling angular velocity when it reached to a steady state to set the 50% and 100% pre-rotation wheel for the 2nd and 3rd simulations respectively.

Figure 3.11 shows the tyre deflection at landing impact. We can simply calculate the amount of tyre deflection at a steady state using Eq. (3.5); however, the wheel angular velocity is enough to set the pre-rotation.

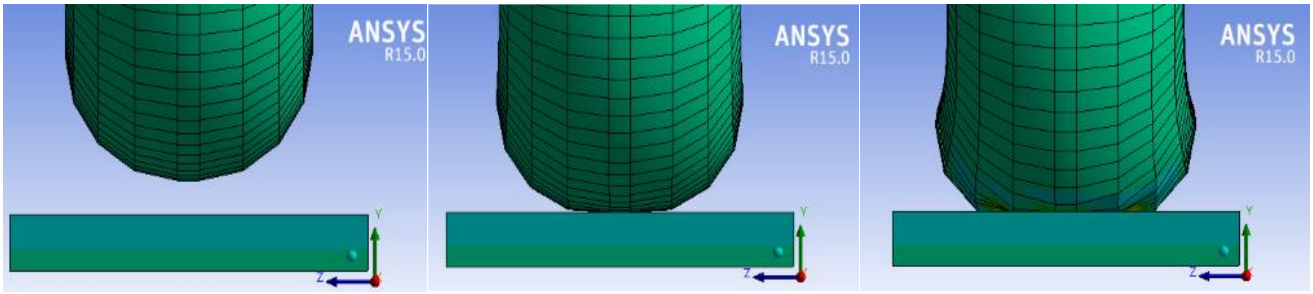

(a) (b) (c)

Figure 3.11 Tyre landing impact: (a) Approach, (b) Touchdown, and (c) Deflection.

The three simulations have the same input data, except the wheel's initial rotational speed, ω_i, therefore, the reaction force, F_R is similar, as the pre-rotated wheel does not make significant changes to the reaction force.

Figure 3.12 shows the vertical and longitudinal forces reacted at a single wheel contact patch versus time during landing, as shown, the peak value of the reaction force is occurred within 0.055 seconds. At this time, the shock absorber is completely

compressed, and the tyre is at the maximum deflection rate, δ. The reaction force is decreased later because it was effected by the shock absorber and tyre damping.

The longitudinal force, F_x follows the reaction force behaviour because a constant friction coefficient is used to avoid model complexity (Eq. 3.4). The friction force increased immediately after touchdown and reached its peak value when the shock absorber and the tyre were fully compressed.

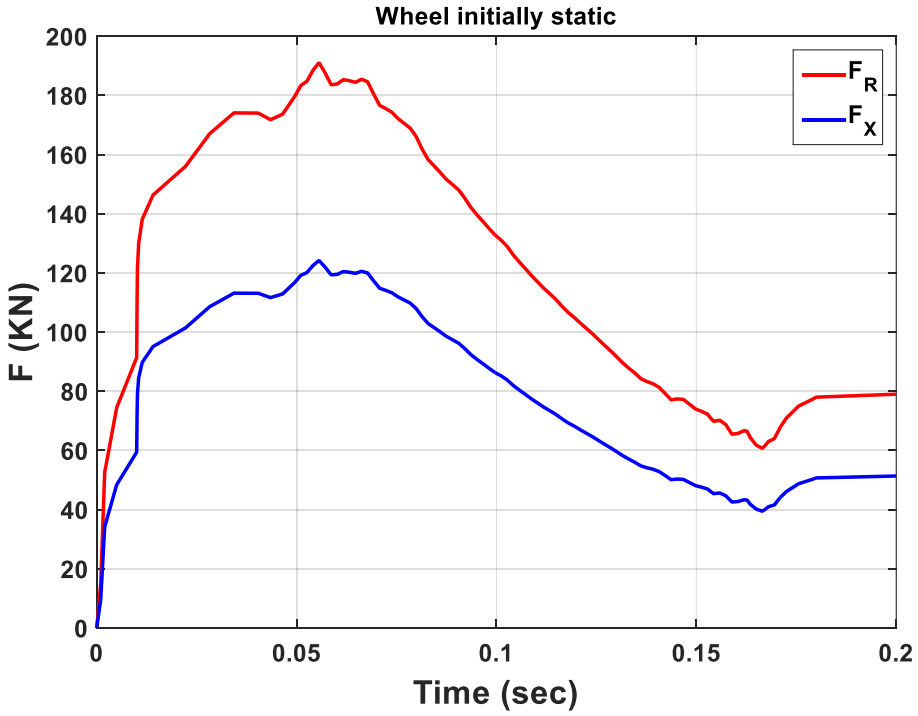

Figure 3.12 Reaction and friction forces vs. time

(Initial horizontal speed = 75.6 m/s, initial sink rate = 2.5m/s).

During the increase in the friction force, the wheel was still at full skid within fractions of a second as it was pulled out by the high forward aircraft speed to cover the full slip distance, until the friction force spun it. At the peak value of the friction force, the wheel

spun-up to overshoot level as it was already rolling and affected by the sudden extra friction force.

Figure 3.13 shows a comparison of wheel angular velocities with initial rotational speeds. For every simulation, the wheel's angular velocity curve is important for showing the wheel's skidding phase, which is the major factor in tyre temperature.

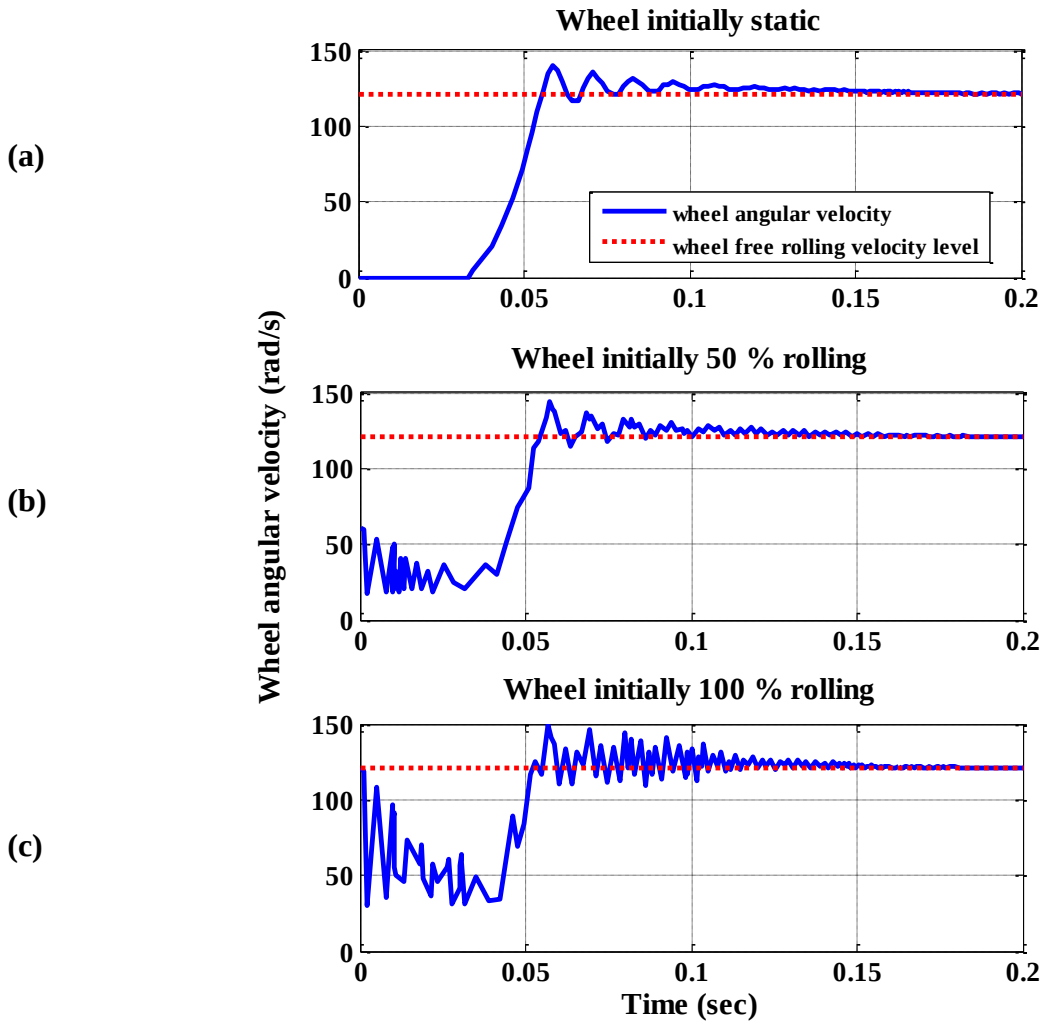

Figure 3.13 Angular velocities vs. time for: (a) initially static, (b) 50% and (c) 100% pre-rotated wheel (initial horizontal speed, $v = 75.6\ m/s$, initial sink rate $= 2.5\ m/s$).

The initially static wheel was at full skid for 0.033 sec with a distance of 2.49 m. Then the wheel started to spin-up and the total skidding distance was 9.1 m during 0.12 sec. This agreed with the Besselink (2000) [60] and Khapane (2006) [61].

The curve shows the wheel spin-up is more than the free-rolling level at 140.4 rad/sec. This is because the wheel was towed to rotate and match the aircraft's forward speed, at the same time, the friction force reached the peak value, as the shock absorber and the tyre were fully compressed and this spun the wheel to overshoot level. During the shock absorber damping, the wheel wavered to spin-down to reach a velocity where $\omega r_e = v$, i.e. the slip ratio can be zero when the aircraft's forward speed is equal to the tangential velocity of a point on tyre's surface. When this occurs, the wheel spin-up phase has ended, and the tyre is able to rolling without interference until breaks are used to slow the wheel.

In the first simulation, the wheel free rolling velocity at a steady state was 121 rad/sec (Eq.3.10). Therefore, this value was set for the 100% pre-rotation, and 60.5 rad/sec was used for the 50% pre-rotation value.

The wheel initially rolling at 50% shows a drop in velocity at the moment of contact with the ground from 60.5 to 17.15 rad/sec within 0.002 seconds. It only waivered for 0.05 seconds with an average of 30 rad/sec.

The friction force became high enough to spin it to overshoot more than wheel's initial static level to 144.23 rad/sec, which is logical as it rotates and is effected by the same effects that occur for a typical landing wheel. However, the steady state rotation was

achieved after 0.13 seconds with slight slipping until 0.14 seconds, and the total distance was 9.83 m.

The wheel initially rolling at 100% pre-rotation also shows a drop at landing impact from 121 to 30 rad/sec within 0.002 seconds. The wheel wavers for 0.04 seconds to spin up to its highest level at 149.31 rad/sec. It settled down to be free rolling after 0.14 seconds with a 10.58 m skidding distance.

Figure 3.14 shows a comparison of wheel slip ratios with initial rotational speeds. The wheel slip ratio calculation is based on the wheel angular velocity and aircraft horizontal speed (Eq. 3.17).

The results shows that when the wheel was initially static it slipped 100% during full skid of the wheel, and it became zero at a steady state.

The maximum value of a 50% pre-rotating wheel was 0.86 of slippage. It increased from 0.5 to 0.72 immediately after touchdown within 0.002 seconds, and it maintained an average value of 0.75 for 0.04 seconds.

The 100% pre-rotating wheel slip increased within 0.002 seconds from zero to 0.75, and then it wavered with an average value of 0.5 for 0.05 seconds.

The comparison shows the lowest average slip was for 100% pre-rotated wheel, but the angular velocity range was the highest. A fully skidding wheel is avoided by pre-rotating the wheel by 50%, but the slip still occurred even with a fully rotational speed. This simulation did not provide torque applied to the spinning wheel before touchdown, and

for this reason, it is possible that the reduction of the pre-spun wheel's angular velocity is high.

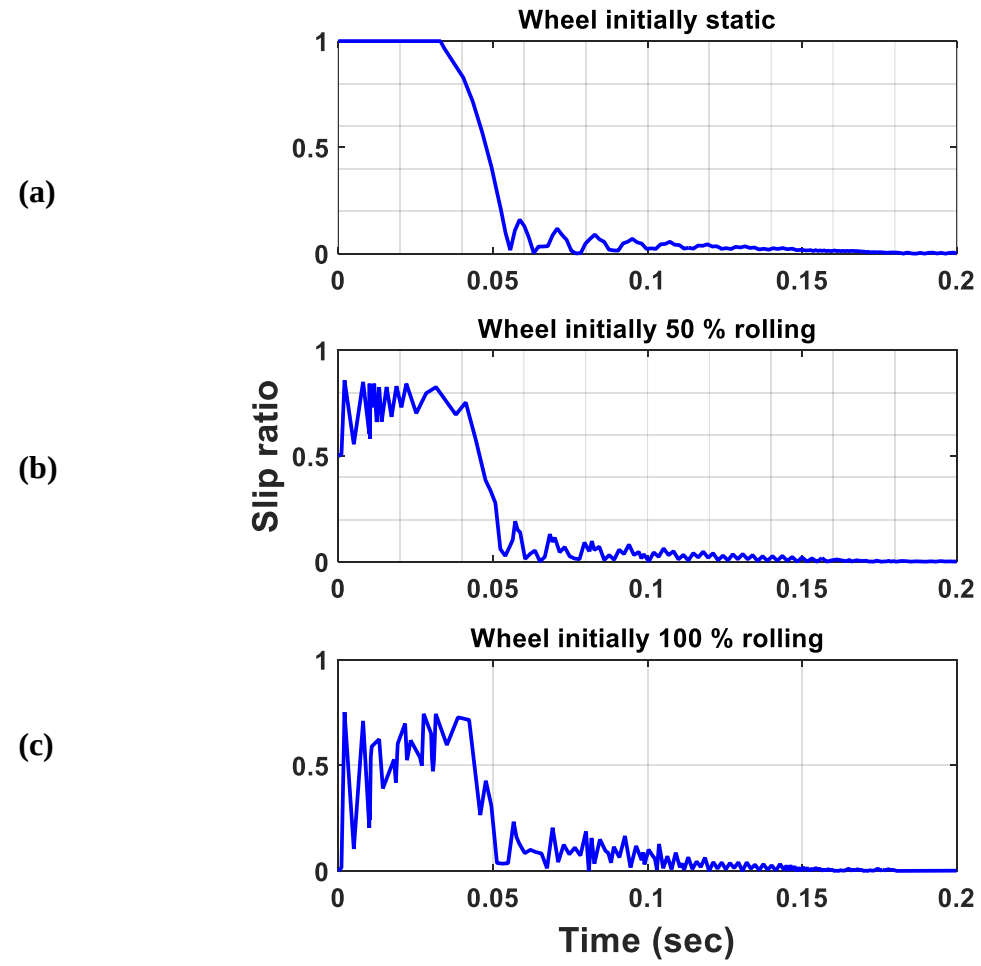

Figure 3.14 Slip ratios vs. time for: (a) initially static, (b) 50% and (c) 100% pre-rotated wheel (initial horizontal speed, $v = 75.6\ m/s$, initial sink rate $= 2.5\ m/s$).

3.3.3 Tyre Tread Temperature

The maximum values of tread temperatures for the three simulations are shown in Figure 3.15. The initially static wheel, in Figure 3.15 (a), recorded the highest temperature on its

first contact area with the runway at 307.41 ˚C. The small area surrounding the wheel had a temperature of 260 ˚C, and the majority of tread temperature was less than 165 ˚C.

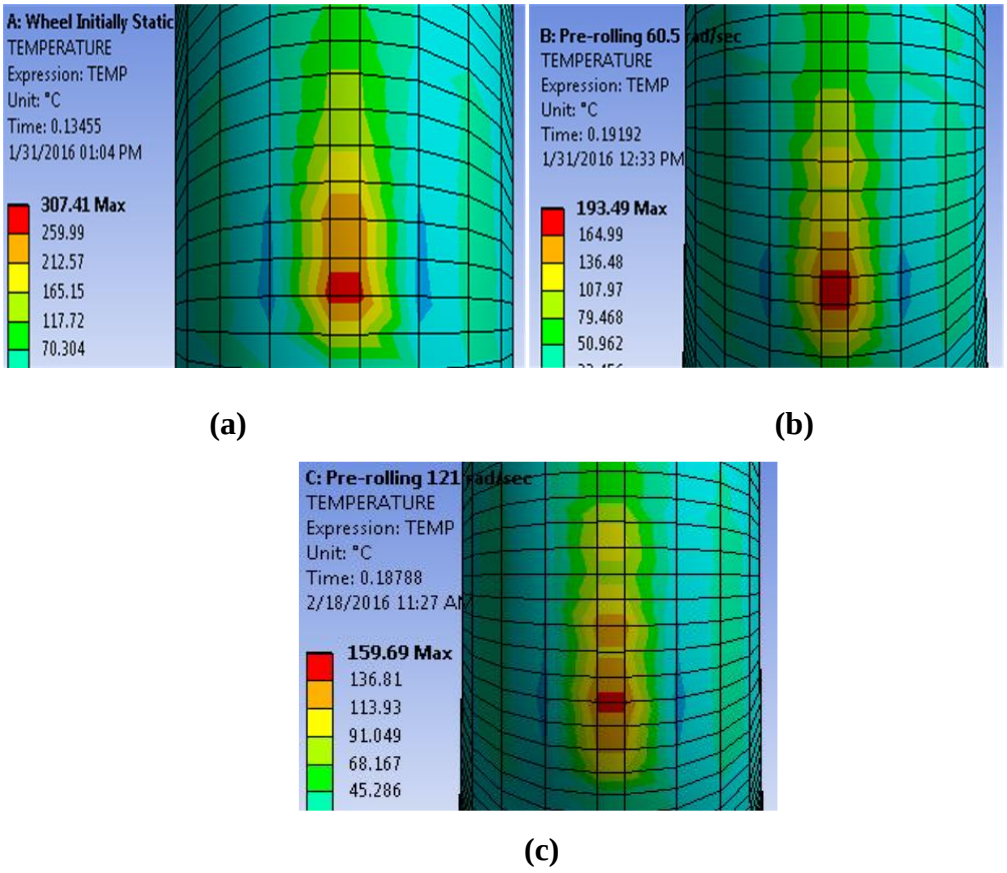

Figure 3.15 Maximum value of tread temperature for (a) wheel initially static, (b) 50% pre-rotated wheel, and (c) 100% pre-rotated wheel.

The temperature is concentrated at the centre line of the tyre's circumference contact area, because the tyre has an elliptical shape, which allows the vertical load to concentrate on the tyre centre rather than the tyre edge.

The static wheel had the highest temperatures because the affected area was fully sliding with a speed equal to the aircraft's forward speed until the longitudinal friction force increased to spin the wheel and then changed its position.

The hottest spot represents the most affected area, and it became sticky and wear occurred easily. Also, the temperature of the surrounding area exceeded the rubber melt temperature. The spin up time was not enough to increase the tyre's circumference area to a high temperature even though the slip was high during spin up.

The temperature decreased by convection due to periods of noncontact for each wheel revolution. Moreover, the tread contacted new cold runway areas that decreased the temperature as well. The fall in temperature appears after the spin-up phase has ended, because it is small compared to the increase in temperature due to the high slip.

Figure 3.15 (b) shows the tyre tread temperature of the wheel initially rolling at 50%, which decreased by 37% comparing with the initially static wheel, as the hottest spot on the tyre tread contact reached 193.49 ˚C. The high temperature was on the area of first contact with the runway, which heated first and then increased with every wheel rotation to be the highest when compared to the tyre's circumference.

In Figure 3.15 (c), the tyre that was initially fully rolling does not show a high reduction of its tread temperature. This is because its slip ratio reached a high level of 75% after touchdown. Also, its maximum temperature was 159.69 Cº on its first contact area.

Figure 3.16 shows tyre tread temperature comparisons, in all simulations, there was a delay in heat flux because the dynamic movement was very fast, and this was followed by an increase in temperatures.

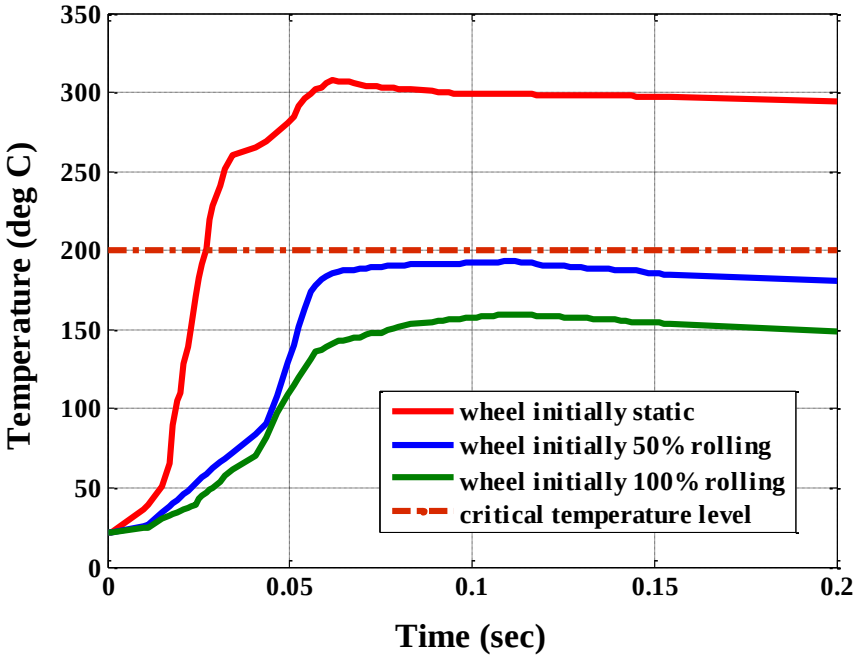

Figure 3.16 Tyre tread temperature vs. time for wheel initially static, 50% pre-rotated wheel, and 100% pre-rotated wheel.

3.3.4 The Effect of Horizontal Speed

With the same inputs, simulations were conducted for an initially static wheel with different landing speeds, $v = 60$ m/s and 90 m/s. The purpose of these simulations is to check the effect of increasing or decreasing the horizontal landing speed on the tyre tread temperature.

Figures 3.17-3.19 show reaction and friction forces, wheel angular velocities, and temperature level curves respectively.

The friction force at the low speed of 60 m/s is higher and increased immediately. This reduced the fully skidding wheel distance (comparing with $v = 75.6$ m/s) to 1.2 m (48% less). Also, the wheel spun up to the maximum value 114.08 rad/sec within 0.052

seconds, and the total skidding phase distance was reduced by 14% to be 7.8 m within 0.13 seconds.

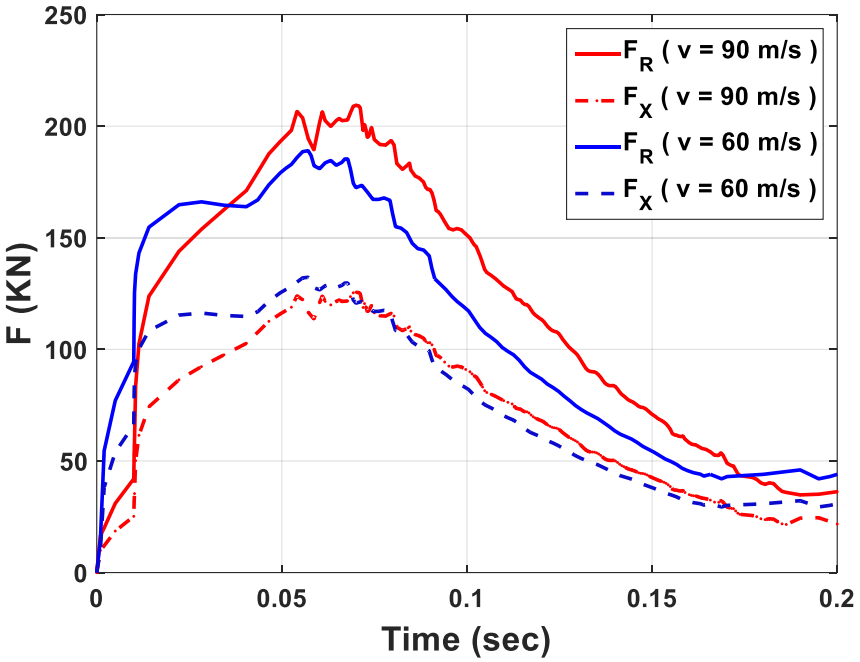

Figure 3.17 Reaction and friction forces vs. time for different landing speeds ($\mathbf{sink\ rate = 2.5 m/s}$).

At the high speed of 90 m/s, the wheel slid longer and was effected by low friction and a high gap between translational and zero rotational speed. The wheel slid for 3.59 m (31% higher), and the total skidding distance increased by 16% to be 10.8 m. The wheel angular velocity reached its peak value at 164.02 rad/sec within 0.064 seconds and settled down after 0.12 seconds.

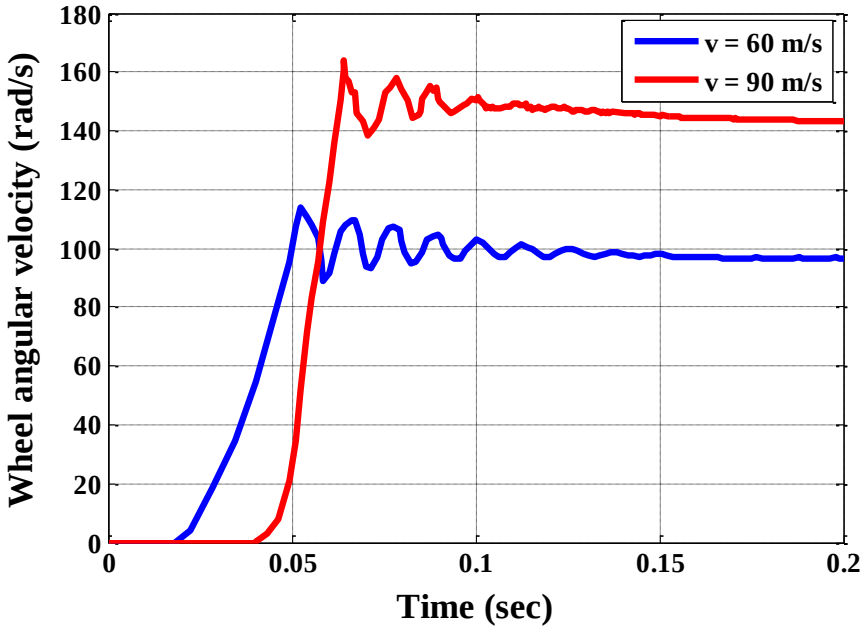

Figure 3.18 Wheel angular velocity vs. time for different landing speeds

(sink rate = 2.5m/s).

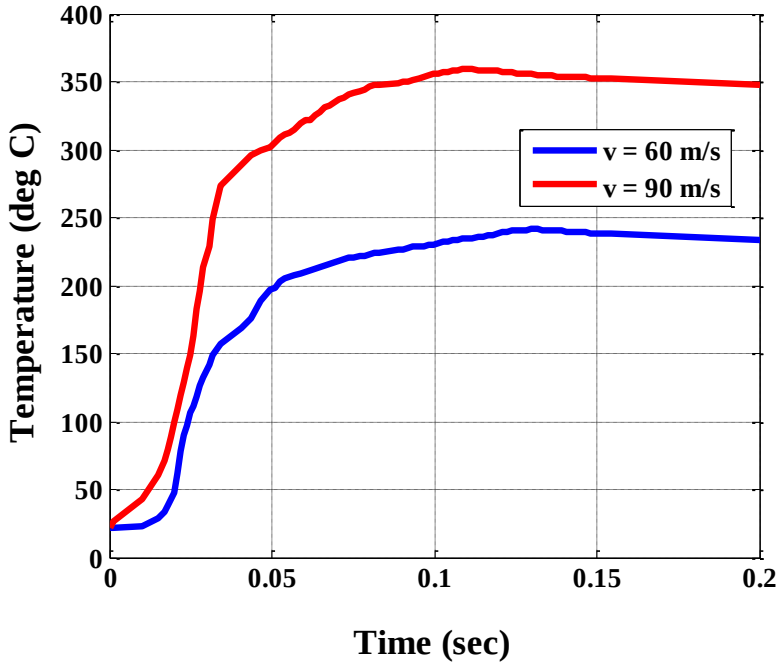

Figure 3.19 Tyre tread temperature levels vs. time for different landing speeds

(sink rate = 2.5m/s).

Figure 3.20 shows the maximum tyre tread temperature values for both high and low horizontal landing speeds. The temperature at the low speed was reduced to 241.3 ˚C (21.5% less) while at the high speed it reached 359.31 ˚C (14.4% higher).

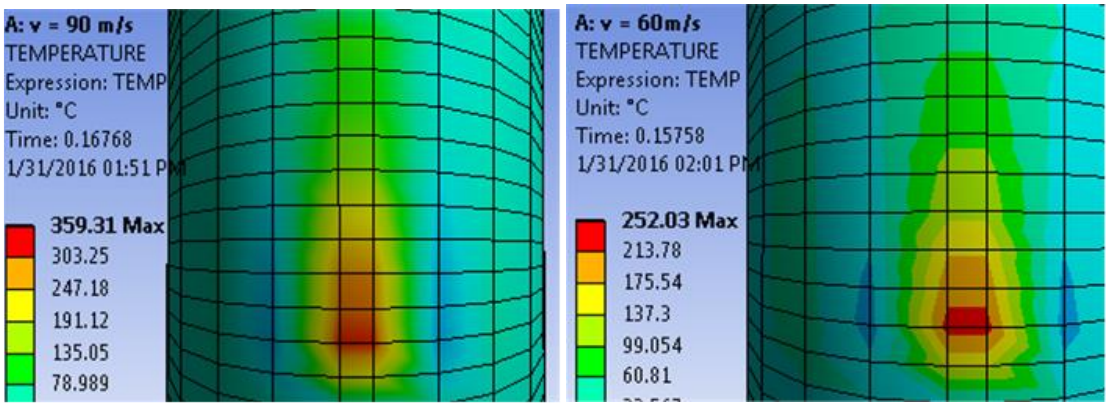

(a) **(b)**

Figure 3.20 Maximum temperature levels for initial landing speeds; (a) $v = 90\ m/s$, (b) $v = 60\ m/s$ (initial sink rate of 2.5 m/s).

3.3.5 The Effect of Vertical Speed

The effect of vertical speed (sink rate) was tested, also using 5 m/s for a hard landing and 1 m/s for a smooth landing with a 75.6 m/s horizontal speed. The results of these simulations are compared with the normal landing simulation result which used a vertical speed of 2.5 m/s.

Figures 3.21-3.23 shows reaction and friction forces, wheel angular velocities, and temperature curves respectively.

The hard landing (sink rate = 5 m/s) shows a temperature lower than for normal landing, because high friction occurred immediately, which reduced the fully skidding wheel time to 0.014 seconds and the distance to only 1.06 m (42% less than for a normal landing).

The total skidding time and distance increased to be 0.13 seconds and 9.83 m respectively. This was because the wheel spun up to 153.67 rad/sec, which is 9% higher than a typical landing. Furthermore, the tread temperature reduced to 284.38 ˚C (7% less) as the time when the wheel is at full skid is reduced.

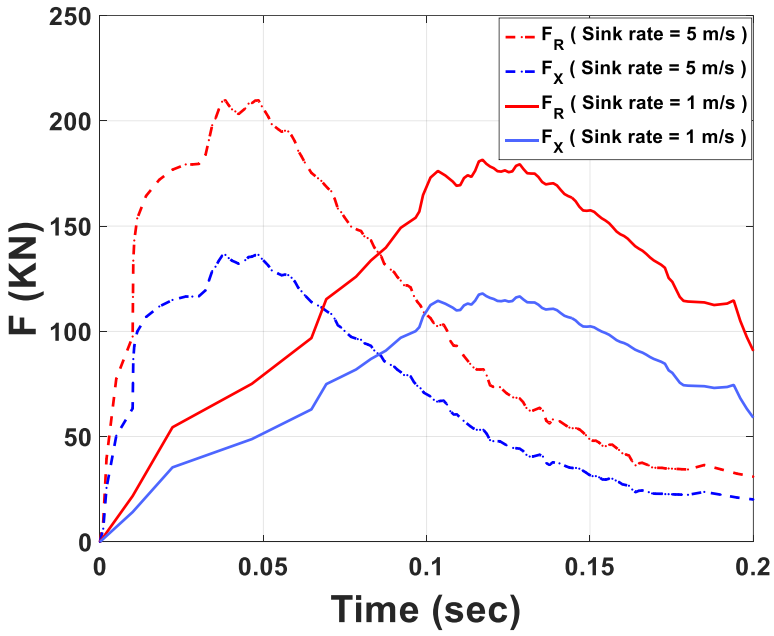

Figure 3.21 Reaction and friction forces vs. time vs. time for different sink rates (initial horizontal speed, $v = 75.6\ m$).

The soft landing (sink rate = 1 m/s) data shows a delay in longitudinal friction that led to skidding a longer distance. The wheel started to spin up after 0.039 sec with a distance of 2.95 m, but the temperature reached to 288.65 ˚C, which is less than for a normal landing (6%). This is because the friction force for a hard landing is less than the friction force for

a normal landing. This appeared with the peak value of wheel angular velocity, which reached 134.76 rad/sec with a relatively long spin up time. The total skidding time and distance was 0.14 seconds and 10.58 m respectively.

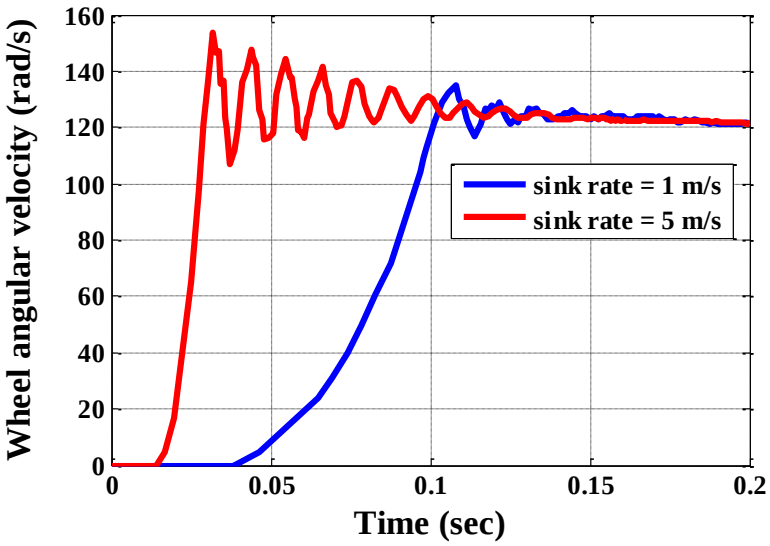

Figure 3.22 Wheel angular velocity vs. time for different sink rates (initial horizontal speed, $v = 75.6\ m$).

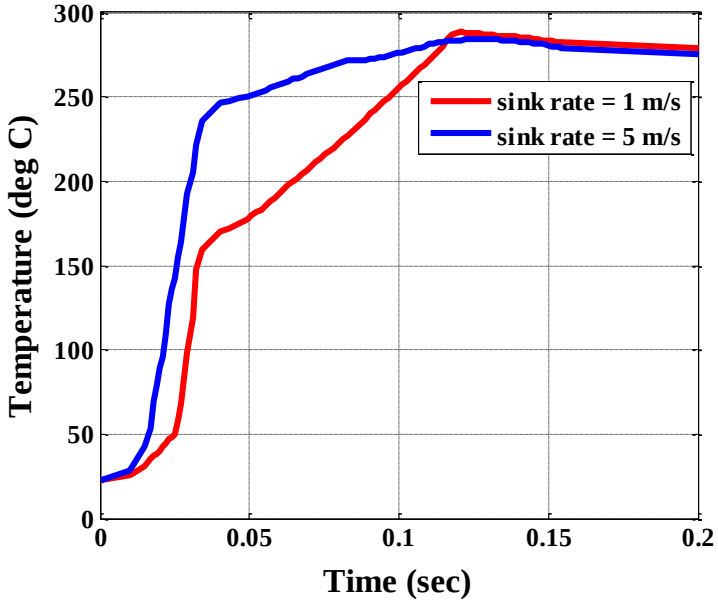

Figure 3.23 Tyre tread temperature vs. time for different sink rates (initial horizontal speed, $v = 75.6\ m/s$).

Figure 3.24 shows the tyre tread temperature profiles for hard and soft landings. The hard landing led to high tyre deflection, which resulted in a large hot spot area compared with a normal and soft landings.

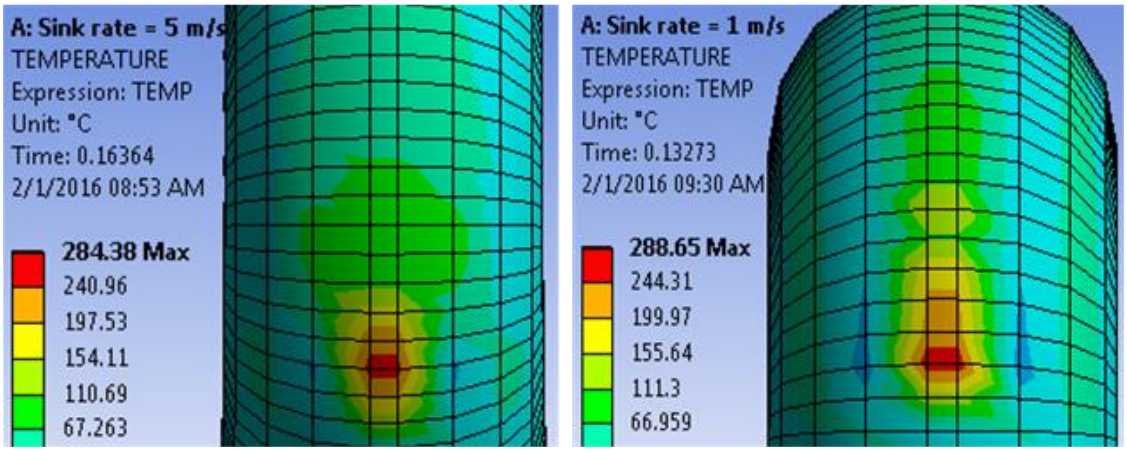

(a) **(b)**

Figure 3.24 Maximum temperature levels for different initial sink rates; (a) 5 m/s, (b) 1 m/s (initial horizontal speed of 75.6 m/s).

3.3.6 Summary of Results

The results show that the aircraft landing smoke can be avoided by pre-rolling the wheel to 50% of its full rotation speed. The tyre tread temperature was less than the critical level for rubber, even with a slipping wheel, because pure sliding is avoided. This means the heat flux is distributed to the whole tyre circumference and the tyre contacts a new cold runway area during every revolution. Moreover, the 50% slipping tyre does produce heat but the skidding time is not enough to increase the tread temperature to a critical level.

For all simulations, Table 3.4 presents the skidding time and distance, maximum slip ratio, and the maximum tread temperatures with input data:

Table 3.4 Summary of results.

	Wheel initially static	50% pre-rotated wheel	100% pre-rotated wheel	High speed landing	Low speed landing	Soft landing	Hard landing
ω_i (rad/ sec)	0.0	60.5	121	0.0	0.0	0.0	0.0
v (m/s)	75.6	75.6	75.6	90	60	75.6	75.6
Sink rate (m/s)	2.5	2.5	2.5	2.5	2.5	1	5
Max. ω (rad/ sec)	140.4	144.23	149.3	164.02	114.08	134.76	153.67
Min. ω (rad/ sec)	0.0	17.15	29.99	0.0	0.0	0.0	0.0
Fully skidding wheel distance (m)	2.49	0.0	0.0	3.59	1.2	2.95	1.06
Fully skidding wheel time (sec)	0.033	0.0	0.0	0.039	0.02	0.039	0.014
Spin-up/ down distance (m)	6.58	9.83	10.58	7.2	6.6	7.56	8.77
Spin-up/down time (sec)	0.087	0.13	0.14	0.08	0.11	0.10	0.116
Total skidding distance (m)	9.1	9.83	10.58	10.8	7.8	10.58	9.83
Total skidding time (sec)	0.12	0.13	0.14	0.12	0.13	0.14	0.13
Max. Slip ratio	1	0.86	0.75	1	1	1	1
Max. Temp. $^{\circ}C$	307.41	193.49	159.69	359.31	241.3	288.65	284.38

Chapter 4

4. Reduction of Tyre Wear by Pre-rotating the Wheel

4.1. Introduction

In this chapter, the same simulation model presented in Chapter 3 with its input data is used to find the amount of tyre wear. The same model with its input data is used. The tyre tread wear is calculated based on Archard wear theory [108] with respect on the effect of tyre temperature on the tread rubber hardness. However, wear is a complex phenomenon; and it is difficult to get the exact value [109]. The Archard wear theory is a simple and common model used to calculate sliding wear between two bodies and it is chosen by ANSYS [110].

The Archard formula considers the main parameters: the reaction force acting on the tyre contact patch, slip distance, contact surface, and the hardness of the softer material [111].

However, the hardness of the softer material is required for the Archard equation, which is the rubber in our model. The temperature is important factor of material hardness which decreases with the increase in temperature [112]. Therefore, the tyre contact surface temperature for every time step is required. Once the temperature is calculated, the correct rubber hardness, according to temperature value, will be substituted in the Archard wear formula for every time step to provide more accurate results. The model provides results for tyre tread wear for a typical aircraft landing, and for wheels already rotated before touchdown, to check how much reduction of tyre wear can be achieved by

pre-spinning the wheel. The effect of increasing or decreasing the horizontal and vertical landing speeds on the tyre wear has also been presented.

4.2. Tyre Wear

The primary location of the abrasive action between tyre and pavement during vehicle operation is on a thin layer of rubber in the tread immediately in contact with the road, called the footprint. This layer and the underlying belt layers are cyclically compressed and uncompressed, creating shear and normal stresses and strains. These stresses and strains make up the frictional work between surfaces, which in turn causes wear of the tread [113]. The magnitude of tyre tread erosion is a function of the severity and duration of the frictional work, the nature of the pavement, properties of the rubber, and other environmental conditions such as temperature, hygrometry, and atmospheric composition [111].

Most tyre wear in an aircraft usually occurs when the tyre comes into contact with the runway and is dependent on the quantity of energy absorbed by the tyre surface during impact. The intensity of wear is proportional to the amount of energy transmitted to the tyre. The absorption of energy is also influenced by the adhesion and the braking conditions of the tyre surface [114].

Adhesion is defined as the process whereby a temporary bond occurs between two sliding surfaces under high pressure conditions. During such conditions, the molecules present in the surfaces are supposed to create a temporary bond between them due to high loads, till the bonds are broken through continuous sliding. During the breaking of bonds, the surface layers will be torn apart from their original positions, leading to wear known as

abrasive wear. In cases where the sliding materials have smooth surfaces, the contact area between the sliding materials is really high, leading to the possibility of a large amount of adhesive wear [115]. Figure 4.1 shows how the rubber behaves on a surface under small and large vertical loads.

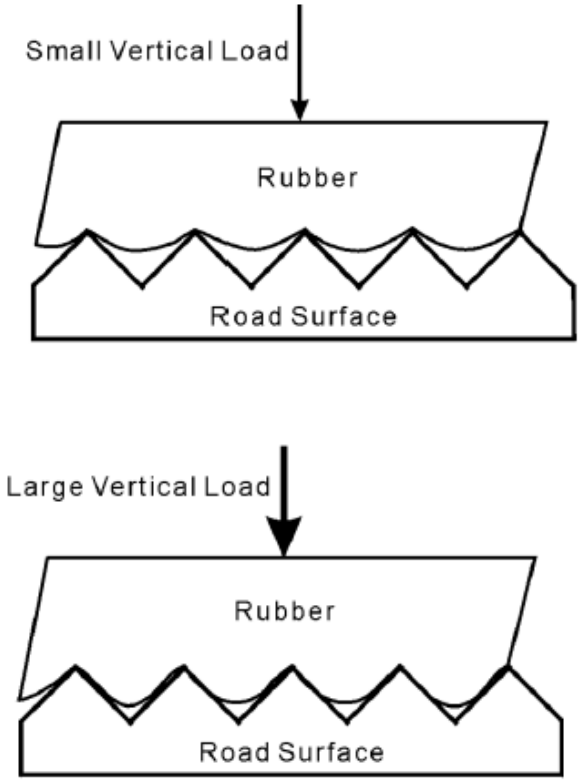

Figure 4.1 Behaviour of rubber under different loads [115].

Another important aspect that determines adhesive behaviour is the type of road surface. The texture of the road surface will have a notable impact on the abrasive force; and the impact will be higher with hard texture road surfaces, even under smaller loads. The presence of hard texture surfaces will create a larger adhesive force under impact. A notable example is when road surfaces made with asphalt, and thus possessing sharper

and harder surfaces, produce abrasive wear to the maximum extent. On the other hand, the sliding velocity between the contact surfaces does create a larger friction force compared to that in surfaces with less texture at low velocity [115]. Therefore, there are two factors that significantly increase the aircraft tyre wear at landing impact; i.e. when the wheel is fully skidding and the vertical load on the tyre is at maximum. Only the skidding speed can be reduced by pre-spinning wheel, while there is no way to avoid the vertical load. Moreover, avoiding a fully skidding wheel, even with high slip, will lead to distribution of the load and frictional heat onto the tyre circumference instead of concentrating them on one area. Therefore, it is expected that aircraft tyre wear will be reduced by the pre-spinning wheel technique, even with slip.

4.2.1 Tyre Wear Estimation

Different methods independently attempt to quantify tyre wear by isolating all but a few factors. One of these methods is the aggregating abrasion pattern, slippage, temperature effects, fatigue theory and the geometry of the contact surface [116]. Other methods, such as Pacejka's "Magic Formula" uses laboratory observed data to determine constants that best fit tyre wear models [117].

The Archard wear theory is a simple model used to associate tyre wear with slip, and is based on the theory of asperity contact. The calculation of abrasion wear is proposed by Archard [108]. The volume of tyre material eroded in Archard wear theory is defined as:

$$V = K_e \frac{F_R}{H} S_D \tag{4.1}$$

where, V is the total volume of wear amount (m^3), F_R is the reaction force reacted at tyre contact patch (N), S_D is the skid distance (m), and K_e is the wear dimensionless coefficient "Archard's abrasion factor", which depends on the wear conditions, heavy or moderate, and is affected by the material's properties and its ability to wear. The value of K_e is less than 1 and it is in a range of 10^{-8} and 10^{-1} [109]. H is the hardness of the softer material, which is the rubber in our case (N/m^2).

Replacing S_D by $\Delta t\ \Delta v_s$ (Eq. 3.18) for every time step and multiplying the rubber density by the two sides of Eq. (4.1) to calculate the wear mass to be as:

$$W_m = \rho\ K_e \frac{F_R}{H} \Delta t\ \Delta v_s \tag{4.2}$$

where, W_m is the wear amount (kg), and ρ is the rubber density ($\mathrm{kg/m^3}$).

As investigated in previous chapter, the aircraft tyre generates heat that exceeds the rubber's critical temperature for about 0.1 seconds immediately after touchdown [2]. Increasing the temperature leads to an increase in the rubber's free volume which decreases the effective molecular conformations potential barriers; thus the rubber's network is weak and the hardness decreases [118].The wear increases with a decrease in the material's hardness [2].

The rubber hardness is usually quoted in Shore hardness values, which range from zero to 100 and are calculated by an indentation test. These values are unit-less, but are related to the rubber's elastic modulus by various algorithms. The available literature shows the relation between the rubber's hardness (in Shore values) and the temperature [119]; however, Archard's formula requires using the rubber's hardness with the unit of N/m^2,

therefore, the rubber's hardness versus temperature is redrawn (Figure 4.2) after converting the hardness unit from Shore values to N/m^2 using a 'hardness conversion chart' [120].

Using Figure 4.2, the hardness values used in this model are based on the tyre tread temperature.

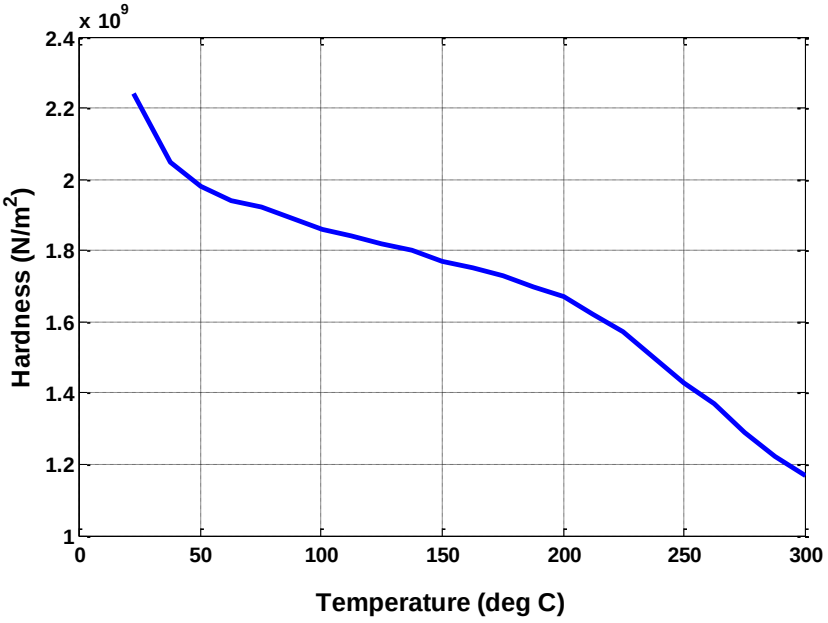

Figure 4.2 Rubber hardness vs. temperature [119].

4.3. Modelling Tyre Wear

The same model, presented in previous chapter with its input data, is employed to find the tyre wear for a typical landing (static wheel) and for pre-spun wheels. The same initial wheel angular velocities, low and high horizontal landing speeds, and low and high vertical landing speeds are used and the same weight is applied on the wheel in order to

find the reduction in tyre wear, plus a comparison of the reduction in tyre temperature and wear for the same landing procedure.

Archard wear theory is employed. For every time step, the correct rubber hardness value is used based on the tyre tread temperature. The value of the tread temperature is not the same on the tyre contact area. In this chapter, the maximum temperature value for every time step is used to choose the rubber hardness from Figure 4.2. The wear calculation flow is shown by Figure 4.3.

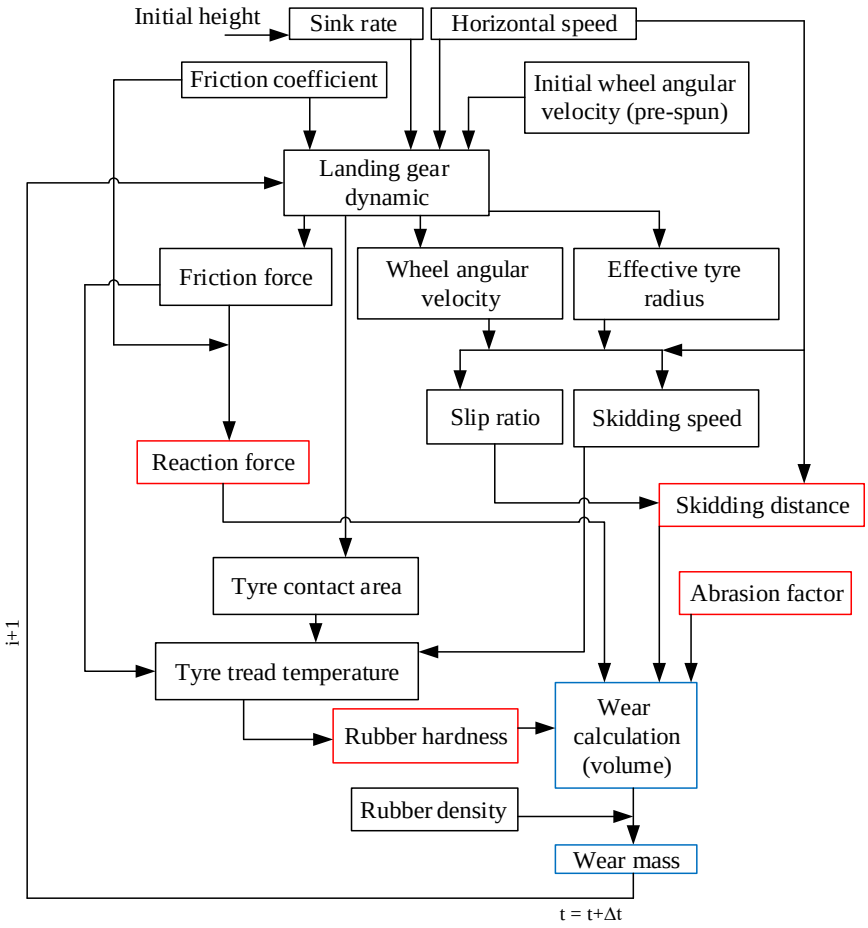

Figure 4.3 Schematic of wear calculation flow.

The solution procedure is to find the Archard wear theory data (Eq. 4.1) which are:

1. Reaction force
2. Skidding distance
3. Rubber hardness
4. Wear abrasion factor (constant)

At the beginning of the simulation, there are initial values:

- Horizontal speed
- Sink rate (downward vertical speed)
- Wheel angular velocity (pre-spun)
- Friction coefficient.

Once the landing gear touches down on the runway, four outputs will be available:

- Friction force between the tyre and runway
- Wheel angular velocity
- The effective tyre radius
- Tyre contact area

Now, the 1st requirement 'reaction force' is computed using the Coulomb friction model (Eq. 3.4) as friction force is known.

From the aircraft horizontal speed, the wheel angular velocity and the tyre effective radius, the wheel slip ratio (Eq. 3.17) is computed. Also, the skidding speed (Eq. 3.15) is computed, thus the skidding distance (Eq. 3.18) is computed, which is the 2nd requirement.

Calculating the 3rd requirement ‘rubber hardness’ requires finding the tyre tread temperature (Eq.3.21) which is calculated as the wheel skidding speed, friction force and tyre contact area are computed.

The wear volume is then calculated; and to find the wear mass in kg, the wear volume is multiplied by the rubber density (Eq. 4.2).

The above procedure is repeated for every time step and the total wear is the result of integration of the wear rate.

4.4. Results and Discussion

The tyre wear is calculated for a typical landing (wheel initially static), 50% and 100% pre-rotated wheels. The horizontal speed is 75.6 m/s and the initial sink rate is 2.5 m/s. The reaction force is similar for the three simulations, as shown in the previous chapter. Therefore, in this part, the comparison of the wear is based on the wheel skidding speed and the tyre tread hardness.

Figure 4.4 shows a comparison of tyre wear rate for a typical landing (wheel initially static), for 50% and 100%pre-rotated wheels. The maximum wear for the three simulations occurred at the same time with different values; this is because the reaction force is similar, but the skidding speed and rubber hardness are different.

Most of wear on rubber of a typical landing occurred during the fully skidding wheel phase and then decreased to be about zero at the end of the skidding phase. The wear curve is increased from the moment of touchdown as the wheel is fully skidding, which means the skidding speed is equal to the aircraft forward speed and the reaction force is

increasing. In other hand, the tread rubber hardness is decreasing, which is increasing the wear rate.

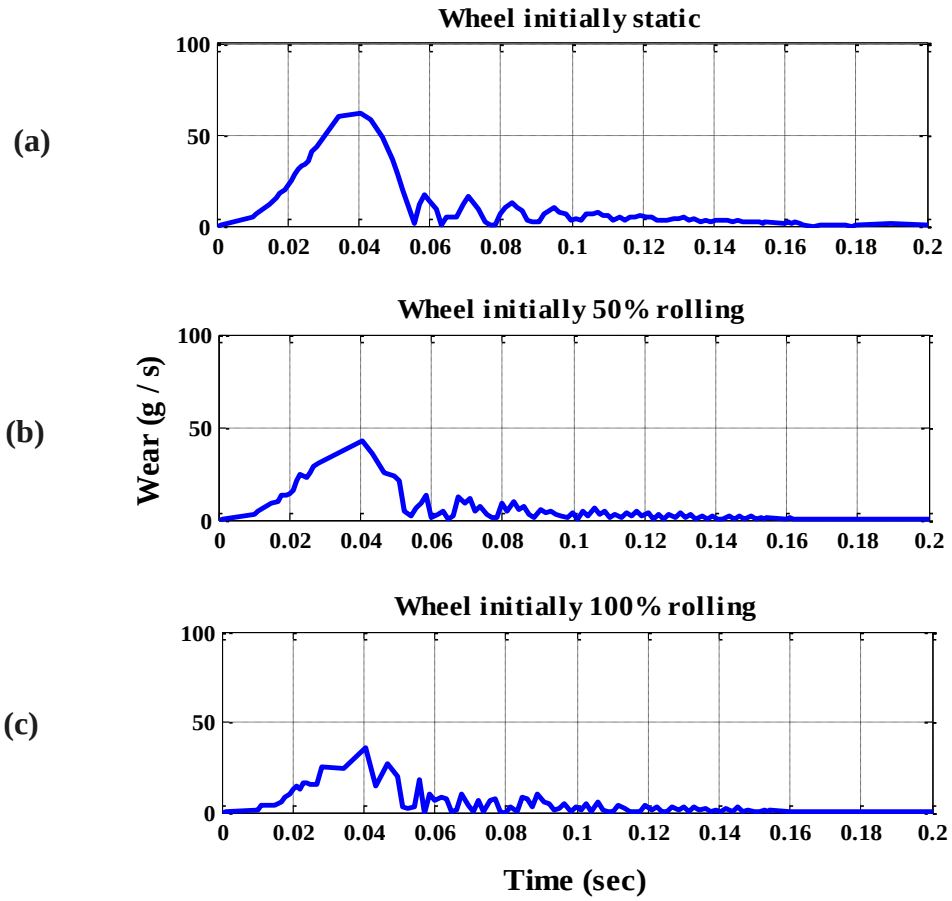

Figure 4.4 Tyre wear rate: (a) initially static, (b) 50%, and (c) 100% pre-rotated vs. time.

The peak value is 61.83 grams per second after 0.04 sec, which occurred before the peak value of reaction force which is at 0.055 seconds, the wear is less at this time because the wheel has already start to rotated due to the friction and aircraft forward speed traction which means a lower skidding speed. The skidding speed became zero for a fraction of a second during the spin-up as the wheel angular velocity reached its free rolling level, while it is increasing to overshoot level, at this time the wear was around zero.

The wear curve increased again as the wheel angular velocity is over its free level "slipping" to fluctuate to the end of the skidding distance. However, the same procedure obtained for all the simulations including the sensitivities of the horizontal and vertical landing speeds.

The 50% and 100% pre-rotated wheels shows a maximum tyre wear rate of 42.89 and 35.55 grams per second respectively, which occurred after 0.04 sec.

The percentage of wear reduction is based on the total wear during the skidding phase. Figure 4.5 shows a comparison of the total wear of tyre, with the wheel initially static, 50% and 100% pre-rotated.

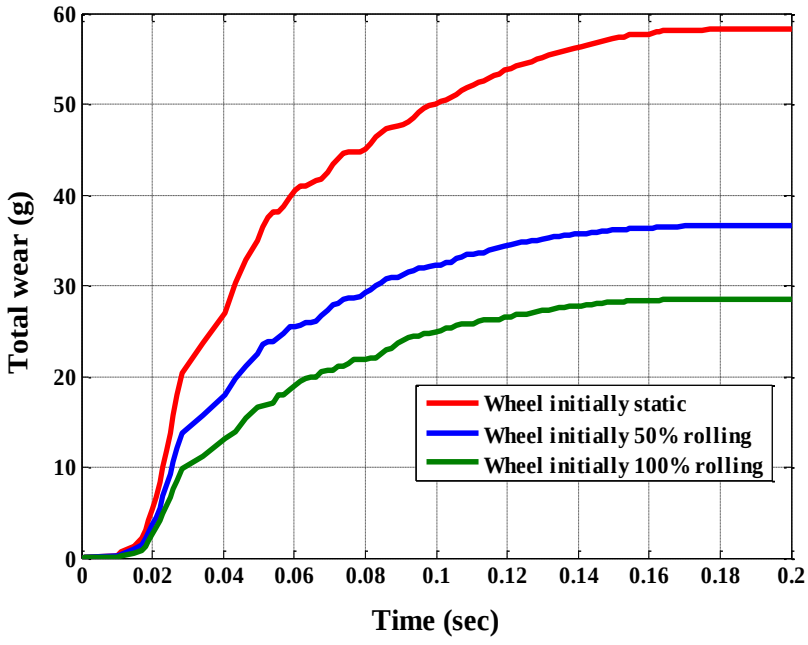

Figure 4.5 Total wear of tyre initially static, 50% and 100% pre-rotated vs. time.

The total tyre wear of the initially static wheel is 58.32 grams which is 0.053% of the tyre weight (110 kg); and multiplying this value by the total number of landing gear wheels (16) gives 933.1 grams. This value is high because the aircraft maximum landing weight is used on all the wheels. However, this value agreed with the results found by Bennett et al. (2011) [6] which is up to 1 kg of rubber eroded for the same aircraft case study.

The total tyre wear of 50% pre-rotated wheel is 36.64 grams which is reduced by 37.17 % compared to the typical landing tyre wear. From the previous chapter results, the critical rubber temperature is avoided at 50% pre-rotation, the tyre will not smoke but the wear still occurs which is the result of high slip.

By using 100% pre-rotation, the total wear is 28.56 grams. The wear is reduced by 51%, which is below expectations, as previous patents expected to avoid the wear completely. However, this value is logical, because the wheel angular velocity dropped at landing impact, slipped and spun-up to overshoot at a high level of rotation, which causes the wear.

4.4.1 The Effect of Horizontal Speed

In this part, the effect of low and high horizontal landing speeds on the tyre wear for a typical landing is investigated. The high and low horizontal landing speeds are 90 m/s and 60 m/s respectively.

The tyre tread wear rate comparison is presented by Figure 4.6. At high landing speed, the wear rate is increased significantly to be 96.84 grams per second after 0.046 sec from touchdown.

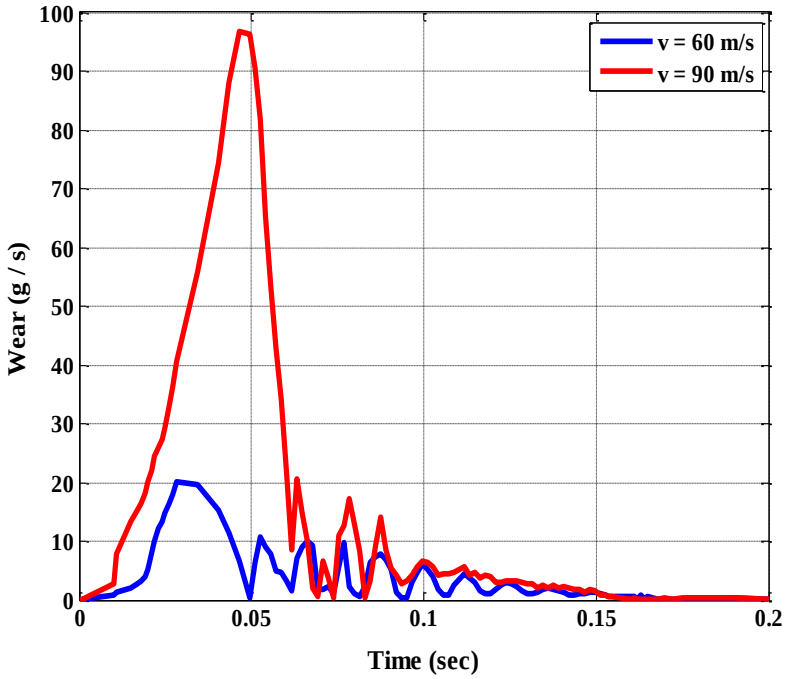

Figure 4.6 Tyre wear rate at different horizontal landing speeds.

This is because the wheel slides for longer as it is pulled by the aircraft forward speed while it in stationary condition, at the same time, the friction force is increasing to spin it, which increases the wear. However, the friction coefficient at a high landing speed is lower than the typical landing contact friction coefficient, which delays the wheel spin-up.

The maximum wear rate value for a slow speed landing is 20.14 grams per second; and it occurs after 0.027 sec from touchdown. This is because the friction coefficient at low landing speed is higher than the high landing speed friction coefficient which spins the wheel faster. Therefore, the wheel did not slide for longer, as the aircraft forward speed is

low. Moreover, the wear is increasing with the increasing reaction force, but at the same time, the wheel is rotated, which means less skidding speed.

The total rubber wear comparison is shown by Figure 4.7. The total tyre wear for a low landing speed is 26.23 grams and for a high landing speed is 76.31 grams.

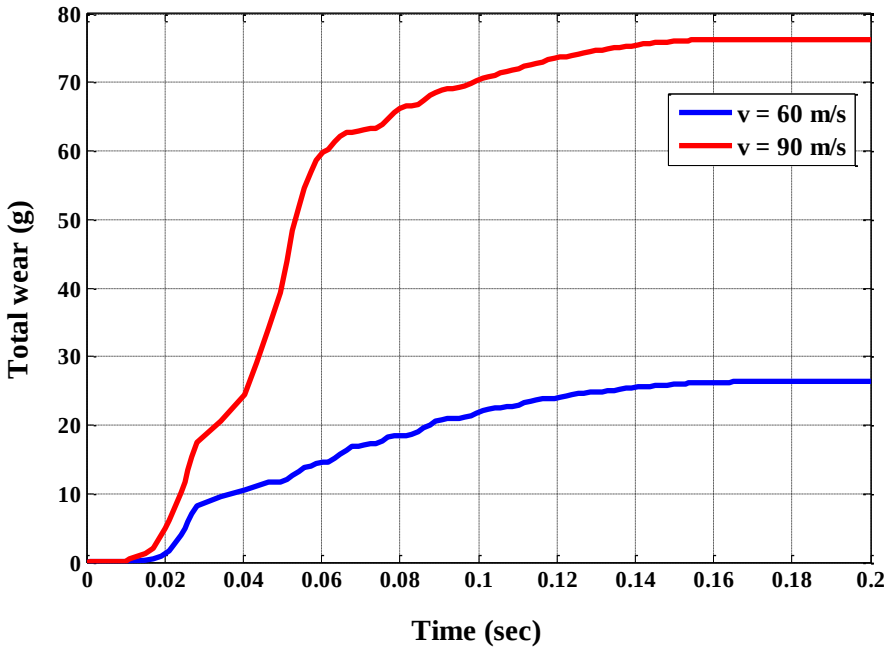

Figure 4.7 Total tyre wear at different horizontal landing speeds vs. time.

The high landing speed is 90 m/s, which is an increase of 16% from the typical landing speed of 75.6 m/s; however, the wear increases by 30.8%, while at low landing speed, the speed reduces by 20.6% and the wear by 54.7%, when compared to a typical landing speed. This means the aircraft tyre wear is very sensitive to any increase in landing speed.

4.4.2 The Effect of Vertical Speed

The low and high vertical speed (sink rate) landings at 1 m/s and 5 m/s respectively were simulated. The tyre wear rate comparison is shown by Figure 4.8. Similar to the tread temperature results in previous chapter, the hard landing shows less wear rate, as the maximum value is only 10.45 grams per second at 0.11 seconds, while the soft landing records 27.27 grams per second at 0.071 seconds.

At hard landing (sink rate = 5 m/s), the friction force is higher which spun-up the wheel faster and reduced the skidding distance and thus the tyre wear. The soft landing (sink rate = 1 m/s) shows a longer skidding distance as the delay in generating of friction force leads to a higher wear rate.

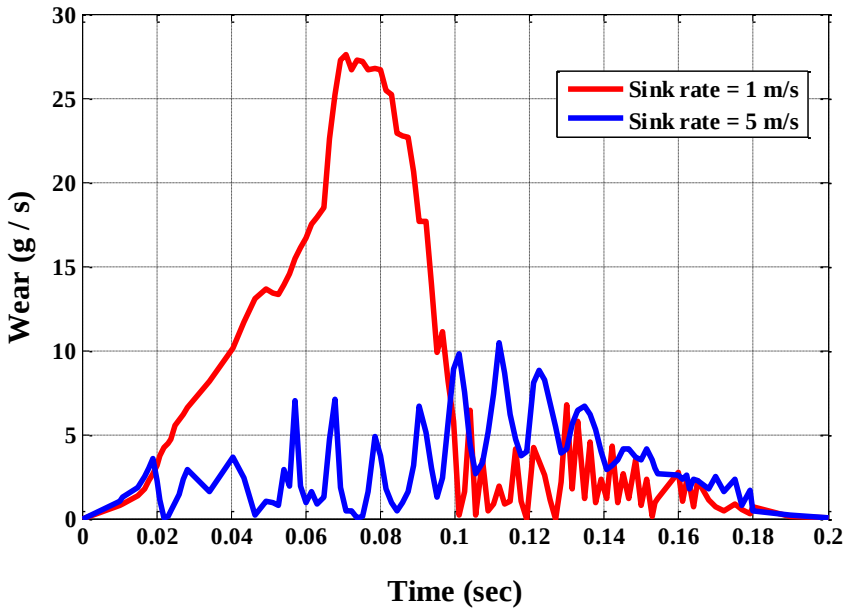

Figure 4.8 Tyre wear rate at different sink rates vs. time.

A comparison of the total rubber wear during the skid phase is shown by Figure 4.9. The hard landing total tread wear is 36.47 grams, which is 37.5% less than the typical landing total tread wear while the sink rate is double that of the typical landing sink rate.

The soft landing total tread wear is 64.58 grams, which is 10.7% higher than the typical landing value, while the sink rate is 60% less than the typical landing sink rate.

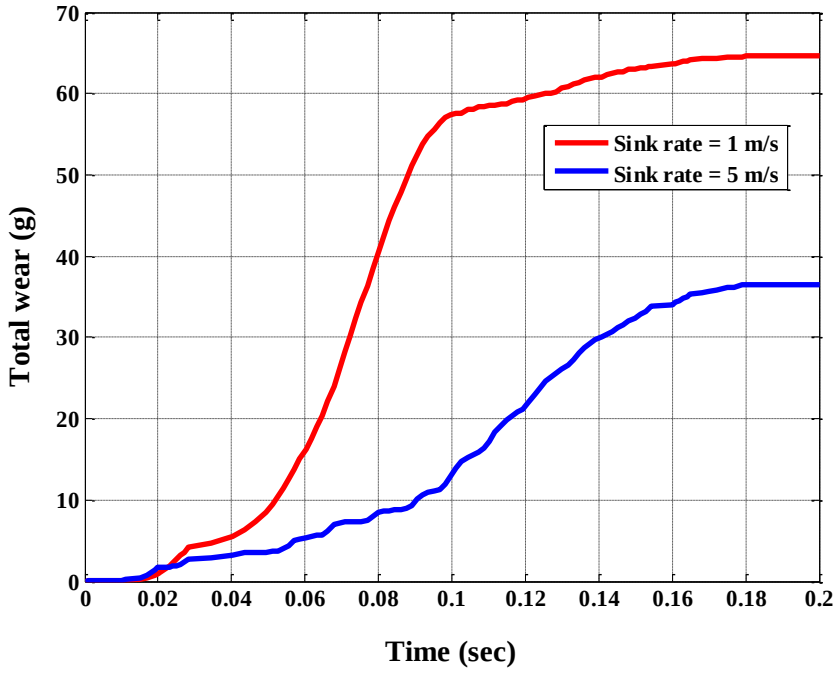

Figure 4.9 Total tyre wear at different sink rates vs. time.

4.4.3 Summary of Results

Table 4.1 shows the tyre tread wear comparison for a typical landing and when initially rolling the wheel plus the sensitivity for different horizontal and vertical landing speeds.

It is possible that in reality, pre-rolling the wheel before landing could reduce the wear more than in the results presented, as only rolling the wheel was used in this simulation

without any torque being applied on it, as a wind turbine would do. The wheel touchdown with torque applied will not show a high drop in its angular speed, which means less slip and consequently less wear. However, this model demonstrated the maximum possible amount of wear to occur for an initially rolling wheel.

Table 4.1 Summary of results.

	Wheel initially static	**50% pre-rotated wheel**	**100% pre-rotated wheel**	**High landing speed**	**Low landing speed**	**Soft landing**	**Hard landing**
ω_i (rad/ sec)	0.0	60.5	121	0.0	0.0	0.0	0.0
v (m/s)	75.6	75.6	75.6	90	60	75.6	75.6
Sink rate (m/s)	2.5	2.5	2.5	2.5	2.5	1	5
Max. ω (rad/ sec)	140.4	144.23	149.3	164.02	114.08	134.76	153.67
Min. ω (rad/ sec)	0.0	17.15	30.0	0.0	0.0	0.0	0.0
Fully skidding wheel distance (m)	2.49	0.0	0.0	3.59	1.2	2.95	1.06
Fully skidding wheel time (sec)	0.033	0.0	0.0	0.039	0.02	0.039	0.014
Total skidding distance (m)	9.1	9.83	10.58	10.8	7.8	10.58	9.83
Total skidding Time (sec)	0.12	0.13	0.14	0.12	0.13	0.14	0.13
Max. Slip ratio	1	0.86	0.75	1	1	1	1
Total wear (g)	58.32	36.64	28.56	76.31	26.42	64.58	36.47
Comparison with the tyre wear of an initially static wheel %	-----	- 37	-51	+30.8	-54.7	+10.7	-37.5

Based on the results in Chapters 3 and 4, pre-rotating the wheel to 50% of its free rolling velocity could avoid aircraft landing smoke and reduce the tyre wear, which would extend life of the tyre. Therefore, the 50% pre-rotation is our choice instead of full rotation; this is because the aircraft wheel is heavy and consequently it may requires large wind turbines for full spinning. Moreover, designing the turbine for full wheel rotation

may lead to excessive free rolling rotation, e.g. in the case of high head wind speed, while using the 50% of free rotation with wind speed equivalent to the aircraft approach speed to design the turbine will guarantee it rotates at the minimum wind speed. This gives the turbine the opportunity to rotate in a safe mode if the head wind were to increase.

Chapter 5

5. Required Torque to Spin the Wheel at Approach

5.1. Introduction

In this chapter, the required torque to spin the aircraft wheel at approach speed has been calculated using ANSYS Workbench CFX, which is used to determine the wheel aerodynamic forces developed by simulation of fluid flows in a virtual environment. The wheel has been tested against different wind speeds, and the aerodynamic forces for the spinning wheel are presented, which include; translational and rotational drags, lift created by vortex, and shaft rolling resistance.

The same case study of a Boeing 747-400 main landing wheel has been modelled using ANSYS CFX in order to calculate the required torque to spin the wheel during the aircraft's approach phase.

The wheel is tested against three high wind speeds. The lowest wind speed is equal to aircraft approach speed in order to simulate the case of a zero heading wind. The model represents the forces created during wheel rotation. Finally, the torque necessary to spin the wheel for required rotation is presented.

The wind speeds used in this simulation are; 80.7, 100, and 120 m/s. The first wind speed (80.7 m/s) is equal to the Boeing 747-400 approach speed [92] whilst the other higher speeds are assumed in case of heading wind speed increase.

5.2. Theoretical Background

In this model, it is assumed that the wheel is moving through the air with zero angle of attack and the direction of rotation of the wheel is anticlockwise. The wheel will accelerate from zero to the required rotational speed.

Figure 5.1 shows the forces to be calculated in order to determine the torque is required to spin the wheel. The wind turbine should be physically attached to the wheel rim to consider the tyre deflection effect at touchdown. In this case, the rim mean radius is the force arm to calculate the required torque to be as:

$$T_{req} = F_{req}\, r_{rim} \tag{5.1}$$

where, T_{req} and F_{req} are the required torque (N.m) and the required force (N) to spin the wheel respectively, and r_{rim} is the mean radius of the rim (m), which depends on the wind turbine position.

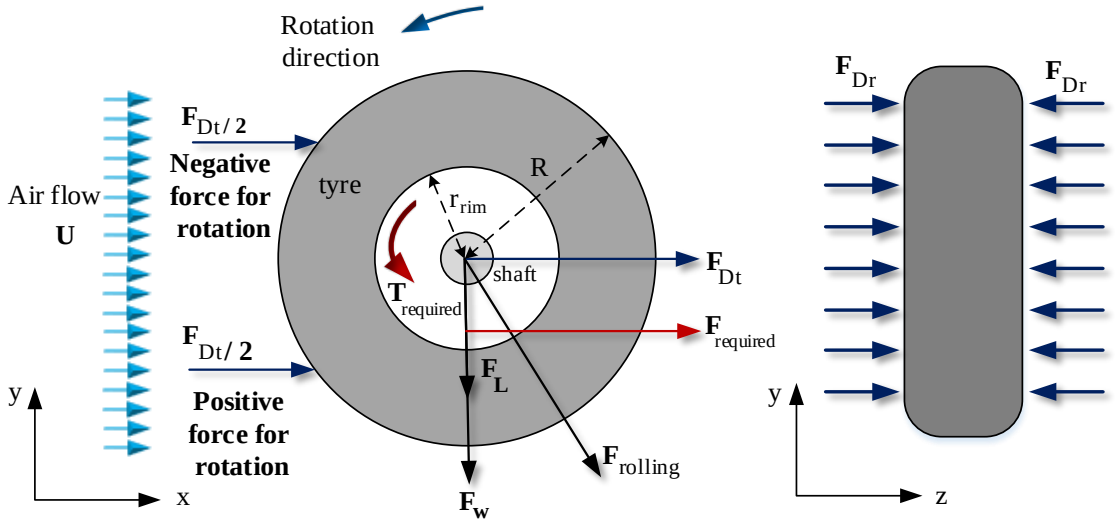

Figure 5.1 External forces acting on the rotating wheel.

The required torque should be equal to the sum of all wheel torques including to the aerodynamic torques some of which will be generated during the wheel rotation. Using Newton's second law for rotation, the required torque will be as:

$$T_{req} = T_{wheel} + T_D + T_{rol} \tag{5.2}$$

where, T_{wheel} is the wheel torque (inertia torque) during acceleration (N.m), T_D is the total drag torque, which is inclusive of the translational and rotational torques (N.m), and T_{rol} is the shaft rolling resistance torque (N.m).

The wheel torque can be expressed by Newton's second law for rotation as:

$$T_{wheel} = I\alpha = I\frac{d\omega}{dt} \tag{5.3}$$

where, I is the mass moment of inertia of the wheel ($kg.m^2$), α is the wheel's angular acceleration (rad/s^2), ω is the wheel's angular speed (rad/sec), and t is the required time to accelerate the wheel (sec).

From Eq. (5.3), this torque depends on the time required to complete the acceleration and it decreases to about zero at ($t = \infty$). Slow acceleration requires less torque and vice versa.

Substituting Eq. (5.3) in Eq. (5.2) with respect to the drag and rolling forces is as follows:

$$T_{req} = I\frac{d\omega}{dt} + (F_D + F_{rol})\, r_{rim} \tag{5.4}$$

where, F_D and F_{rol} are the drag and rolling-resistance forces respectively (N).

5.2.1 Drag Force

There are two types of drag force. Firstly, the translational drag in x direction (F_{Dt}), which hits the wheel frontal area as shown in Figure 5.1. Half of this force is positive for rotation and other half is negative "resistance" and because the wheel is symmetrical, therefore, the two parts have an equal and opposite effect in the static condition and the resultant torque on the wheel shaft becomes zero.

On the other hand, the total force, will be applied to the wheel shaft in x direction which will increase the rolling resistance.

The formula of translational drag can be calculated as:

$$F_{Dt} = \frac{1}{2}\, \rho_A\, C_{Dt}\, A_f\, U^2 \tag{5.5}$$

where, ρ_A is the air density (kg/m^3), C_{Dt} is the translational drag coefficient, U is the wind speed acts on the wheel (m/sec), and A_f is the wheel frontal area (m^2) [121]. The frontal area is roughly rectangular: $A_f = 2RD$, here R and D are wheel radius and width respectively. The force on the wheel frontal area is different from centre to the top or bottom surfaces.

Once the wheel starts to rotate, half of this force in the positive direction becomes higher than the one in negative direction which is effected by the wheel rotation direction, this force is helpful as it will be added to the required force for spinning the wheel.

The other drag force is that created during wheel rotation and it is called "rotational drag force" which increases in magnitude with increasing wheel angular velocity and occurs

around the two side areas of the wheel, acting in the rotation (z) axis. The rotational drag can be calculated by this formula:

$$F_{Dr} = \frac{1}{2}\,\rho_A\,C_{Dr}\,A_{side}\,R^2\omega^2 \tag{5.6}$$

where, C_{Dr} is the rotational drag coefficient, A_{side} is the two side areas of the wheel (m^2), R is the wheel radius (m), and ω is the wheel angular velocity (rad/sec) [122].

5.2.2 Rolling Resistance Force

Three types of force act on the wheel shaft in x and y directions resulting in the total rolling force, F_{rol}. The three forces are, as follows:

1- Translation drag force (F_{Dt}) presented in Eq. (5.5), is applied to the shaft in (x) direction.

2- The wheel weight force, F_w in ($-y$) and is simply; $F_w = m_w\,g$, where, m_w is the wheel total mass, and g is the acceleration due to gravity.

3- The lift force, which is created during the wheel rotation against air flow, can be calculated using the Kutta-Joukowski lift theorem for a rotated cylinder, as shown in Figure 5.2.

Kutta-Joukowski lift theorem for a cylinder [123] describes how the lift force depends on the direction of rotation and acts perpendicular to the air flow direction. The cylinder is pulling a thin layer of flow molecules in its rotation direction resulting in a faster flow on the lower surface than on the upper surface, which leads to less pressure than cylinder top surface. The cylinder upper surface will also pull a thin layer in the opposite direction to

the flow which creates a vortex. This vortex has the effect of increasing the upper pressure. The difference in pressure between the cylinder top and bottom surfaces is the lift force per unit length.

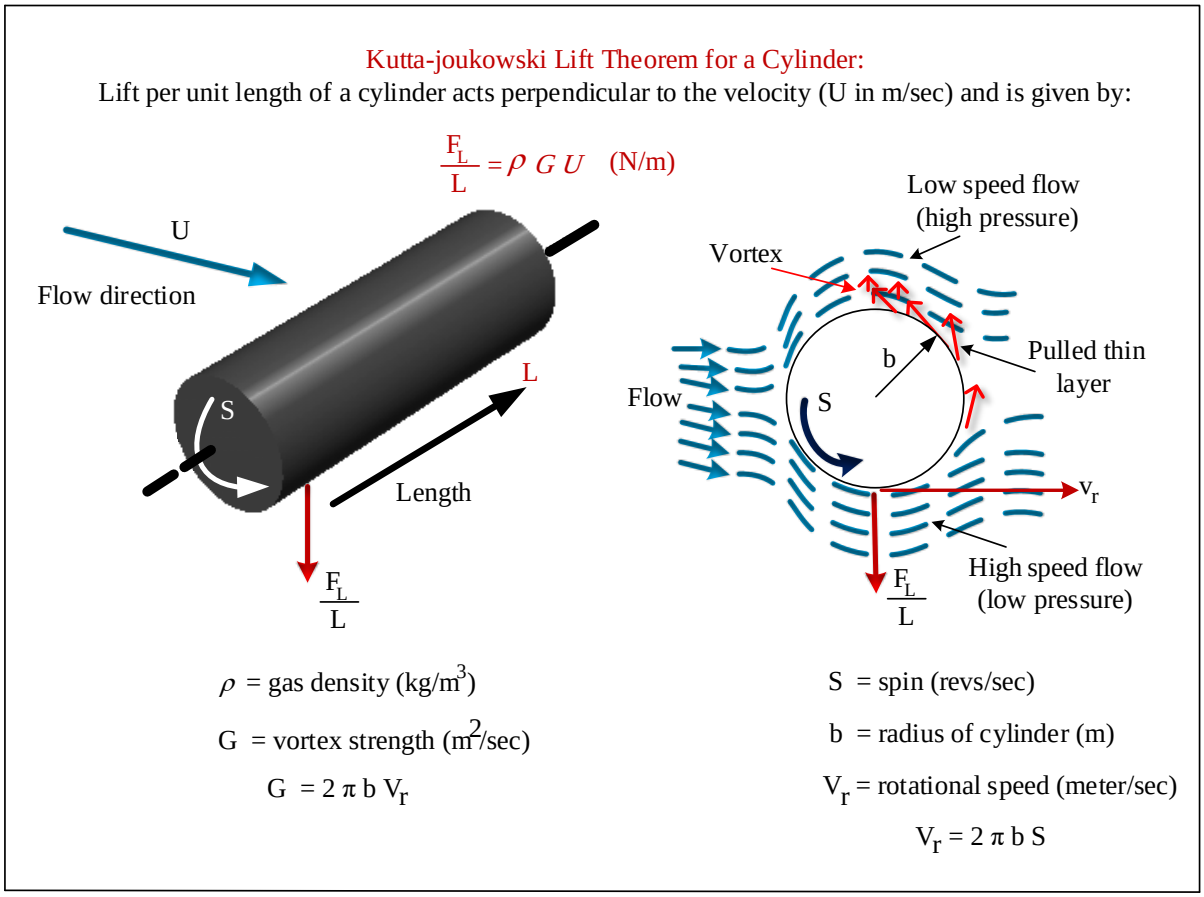

Figure 5.2 Lift force per unit length created during cylinder rotation (modified from [123]).

In our case, the negative (downward) lift force increases the resistance on the shaft because it acts in same direction as the wheel weight force. However, based on the Kutta-Joukowski lift theorem, the lift force can be calculated as follows:

$$F_L = \rho_A \, G \, U \, D \tag{5.7}$$

where, U is the wind speed (m/sec), D is the wheel width (m), and G is the vortex strength (m^2/sec) and is given by:

$$G = 2 \, \pi \, R \, v_r \tag{5.8}$$

where v_r is the relative wheel speed (m/sec), and is given by: $v_r = R\omega$ [123]. The relative speed gives the spin ratio as: $\frac{v_r}{U}$. The increasing of the spin ratio causes an increasing in the lift force [88, 124, 125].

Substituting Eq. (5.8) in Eq. (5.7), and $v_r = R\omega$, the lift force will be as:

$$F_L = 2 \, \rho_A \, \pi \, R^2 \omega \, U \, D \tag{5.9}$$

Now, simply the total force acting on the wheel shaft will be as:

$$F_{ts} = \sqrt{(F_w + F_L)^2 + {F_{Dt}}^2} \tag{5.10}$$

where, F_{ts} is the total force applied to the shaft (N).

Note: The term $(F_w + F_L)$ will be $(F_w - F_L)$ if the wheel rotate clockwise with the same current flow direction.

The bearing friction coefficient must be considered to estimate the rolling resistance. Therefore, the shaft rolling resistance force will be as [126]:

$$F_{rol} = C_r \, F_{ts} \tag{5.11}$$

where, C_r is the bearing friction coefficient, assumed to be angular contact ball bearing with value of 0.0015 [127].

Due to the complexity of fluid flow physics, the wheel aerodynamic forces can be determined numerically using CFD simulation [128]. Therefore, the wheel is modeled using ANSYS CFX to calculate both the forces and the required torque.

5.3. Simulation Model

The present work describes a thorough investigation of 3D computations concerning the air flow around the wheel. The calculated results give a clear indication of the air flow distributions for different inlet velocity values (U = 80.7, 100 and 120 m/s). Modelling tasks using CFD programs will allow us to get closer to the real operating conditions.

Figure 5.3 shows the simulation model overview. The wheel is rotated from zero to 60.5 rad/sec during thirty seconds with constant acceleration ($2.02\ rad/s^2$), maintaining a constant angular speed for a further ten seconds. This is based on assuming that there is sufficient time from retracting the aircraft landing gear to touchdown. However, the purpose of spinning the wheel is to investigate the wheel's aerodynamic forces generated during rotation; these forces are not present on a stationary wheel.

The 3D wheel geometry is modelled using the ANSYS design modeller together with the data as presented in Table 3.1.

The wheel modelled inside the large domain is as shown in Figure 5.4: the tyre being smooth without grooves. The domain dimensions are 20 m x 20 m inlet area by 40 m

long to avoid the wall boundary effect and to be representative of the real aircraft wheel conditions during approach in open air.

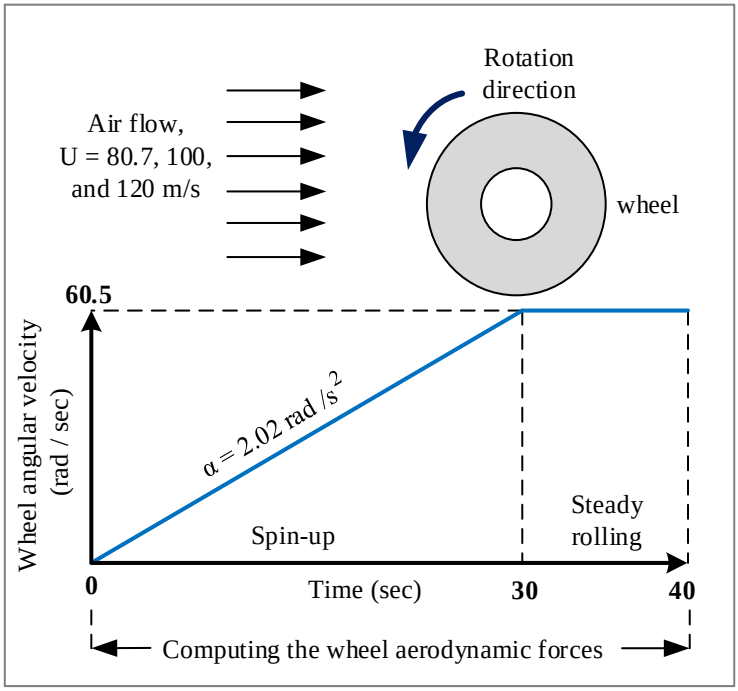

Figure 5.3 Simulation model overview.

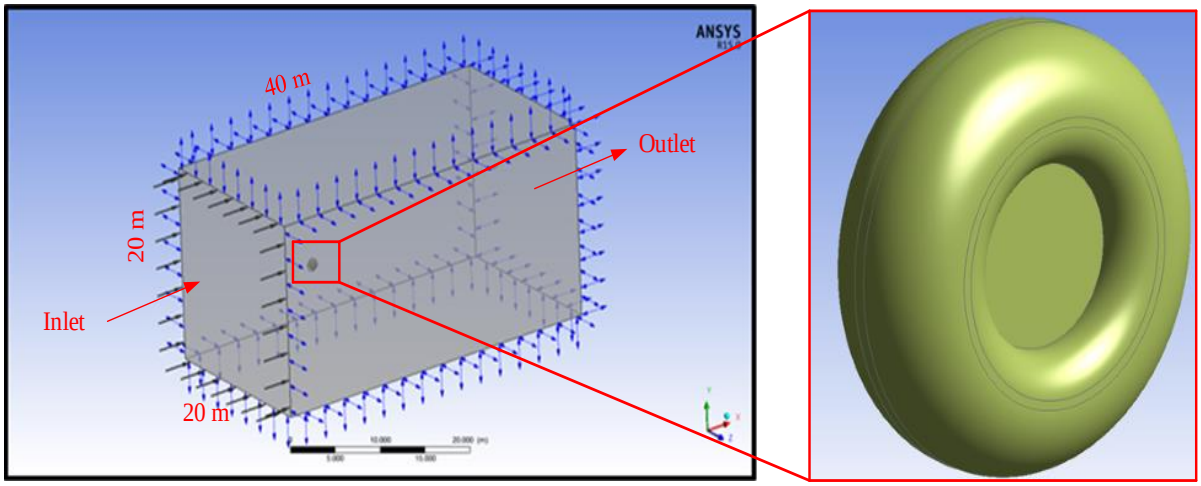

Figure 5.4 Wheel domain.

5.3.1 Mesh Generating

High-quality mesh created for accurate solutions and good convergence. A "Patch Conforming Method" was used to generate the mesh with tetrahedron form elements. In addition, prismatic layers are constructed for the flow near the walls and on the wheel surfaces using “smooth transition” option for more accuracy [129].

The flow regime is subsonic with static temperature at 288 K and the turbulence is zero. Reference and relative pressures are $1.013x10^5$ and 1 Pa respectively. Rough wall surfaces are used as the shear stress transport model (SST) does not accurately predict the amount and onset of the flow separation from soft surfaces [130].

Figure 5.5 shows the mesh interface, and Table 5.1 presents the mesh statistics. The boundary conditions are the same for all simulations except the inlet velocities.

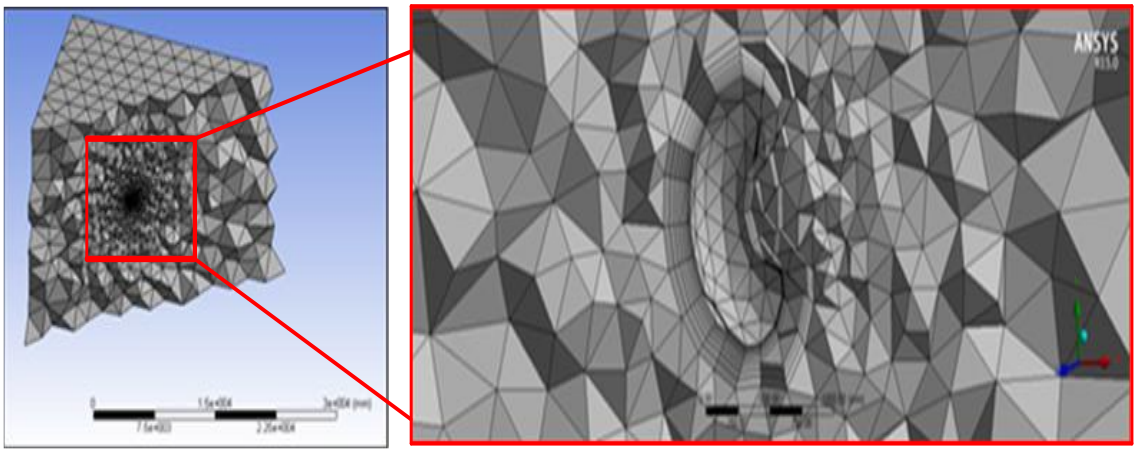

Figure 5.5 Mesh interface of the wheel domain.

The flow type and the physical model in the fluid domain is defined as ‘steady state’ with turbulence conditions using Reynolds-Averaged Navier-Stokes equations. Turbulence is

modelled using the SST (Shear Stress Transport) model and heat transfer using the total energy model.

Table 5.1 Mesh statistics.

	Value
Nodes	9197
Elements	43703
Tetrahedrons	39663
Prisms	4040
Faces	1952
Orthogonality Angle [131]	27.4^0, acceptable range $> 20^0$
Expansion factor	20^0, acceptable range $< 20^0$
Aspect Ratio	57^0, acceptable range $< 100^0$

The SST turbulence model is commonly used and is suitable for a wide range of applications. The SST turbulence model is attached as Appendix B.

The total energy model allows for high speed energy effects and is therefore, suitable for high speed flow applications and has better performance at wall boundaries [132, 133].

5.3.2 Solution Convergence

ANSYS CFX uses an iterative approach to solve Reynolds-Averaged Navier-Stokes (RANS) equations to reach a converged solution. In ANSYS CFX, there are two methods to check the solution convergence; the first method is by checking the residual value, which is the most important measure of convergence because it relates to the accuracy of the solved equations. The root mean square (RMS) residual level of 1E-4 is the default target and sufficient for many engineering applications [134]. A residual level of 1E-5 is considered well-converged and 1E-6 is considered tightly converged, but usually the residual cannot achieve the levels of 1E-6 or 1E-5. However, a residual level below 1E-3 is an acceptable convergence [128].

The second method is by tracking the variations of the aerodynamic loads to be low at the end of iterations, in other words, the variable should converge to an approximate fixed value at every iteration, which indicates less imbalance [134].

Figure 5.6 shows the residual values of the pressure and the velocity components for the first simulation. All the simulation solutions are considered converged as the residuals decreased to below 1E-3 with a low imbalance at the end of the iterations.

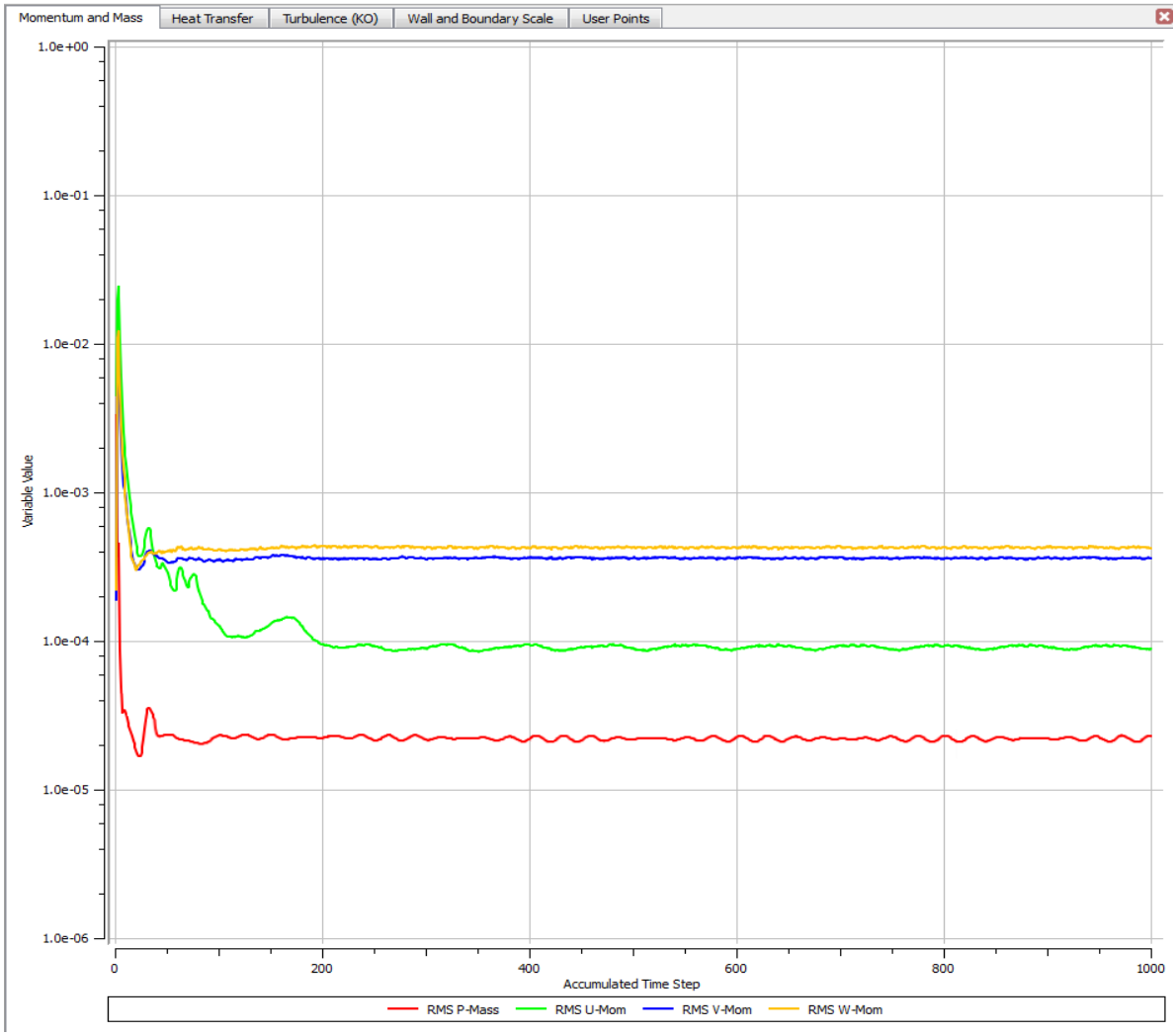

Figure 5.6 Variations of the residual for the pressure and the velocity components vs. accumulated time step.

5.4. Results and Discussion

A comparison of the air flow around the wheel at three wind speeds; 80.7, 100, and 120 m/s is shown in Figures 5.7-5.10.

As shown in velocity x-y diagrams, a thin layer of flow molecules is pulled by the wheel in the rotation direction. At the top of the wheel, the layer of flow is in the opposite direction to that of the wind which created the vortex, this has the effect of increasing the pressure at the top of the wheel, thus producing a negative lift force. Moreover, the wind speed is higher at the wheel bottom with consequently less pressure than the top wheel area, which leads to the total overall vertical force acting on the wheel to be in a downward direction.

The lift force varies directly as the wind speed, that is the higher the wind speed the higher the lift force developed. The air flow speed behind the wheel is approximately zero for all wind speeds, which is in agreement with Kothalawala et al. (2013) [86].

In general, an increase in the wind speed produces a corresponding increase in the aerodynamic forces around the wheel.

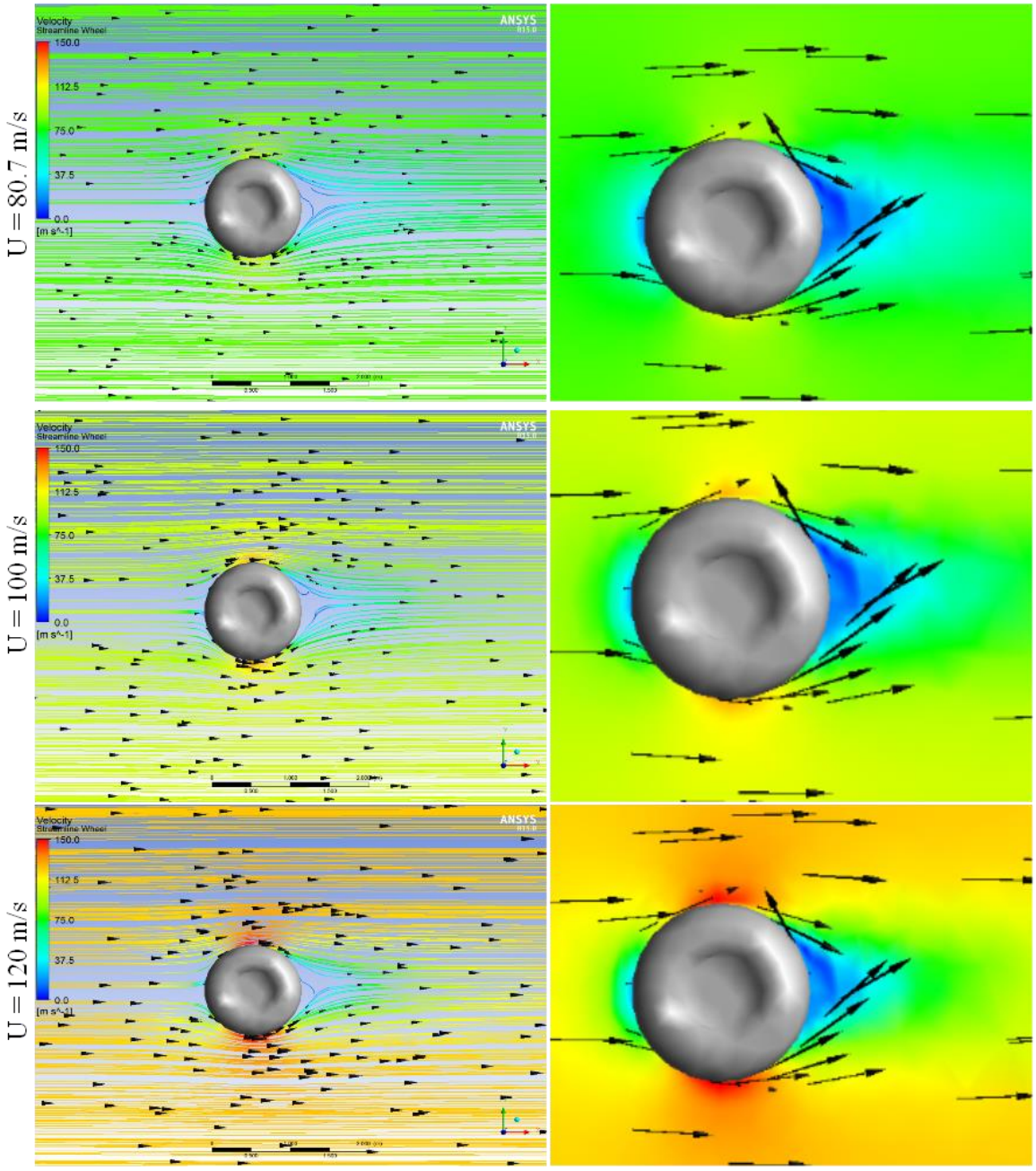

Figure 5.7 A comparison of different velocity flow profiles around the wheel at different wind speeds

(Streamline fluid velocity, plane x-y)

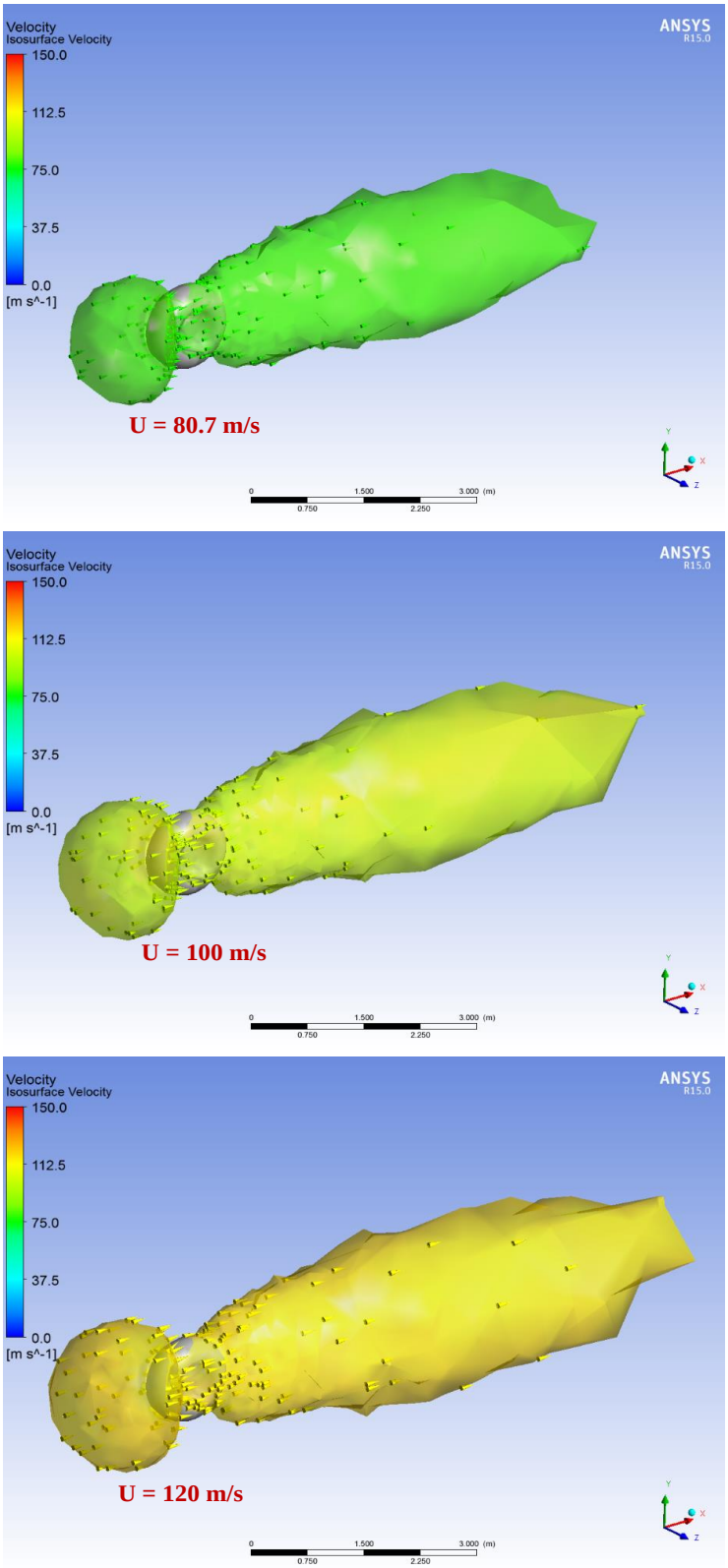

Figure 5.8 A comparison of different velocity flow profiles around the wheel at different wind speeds (Iso surface).

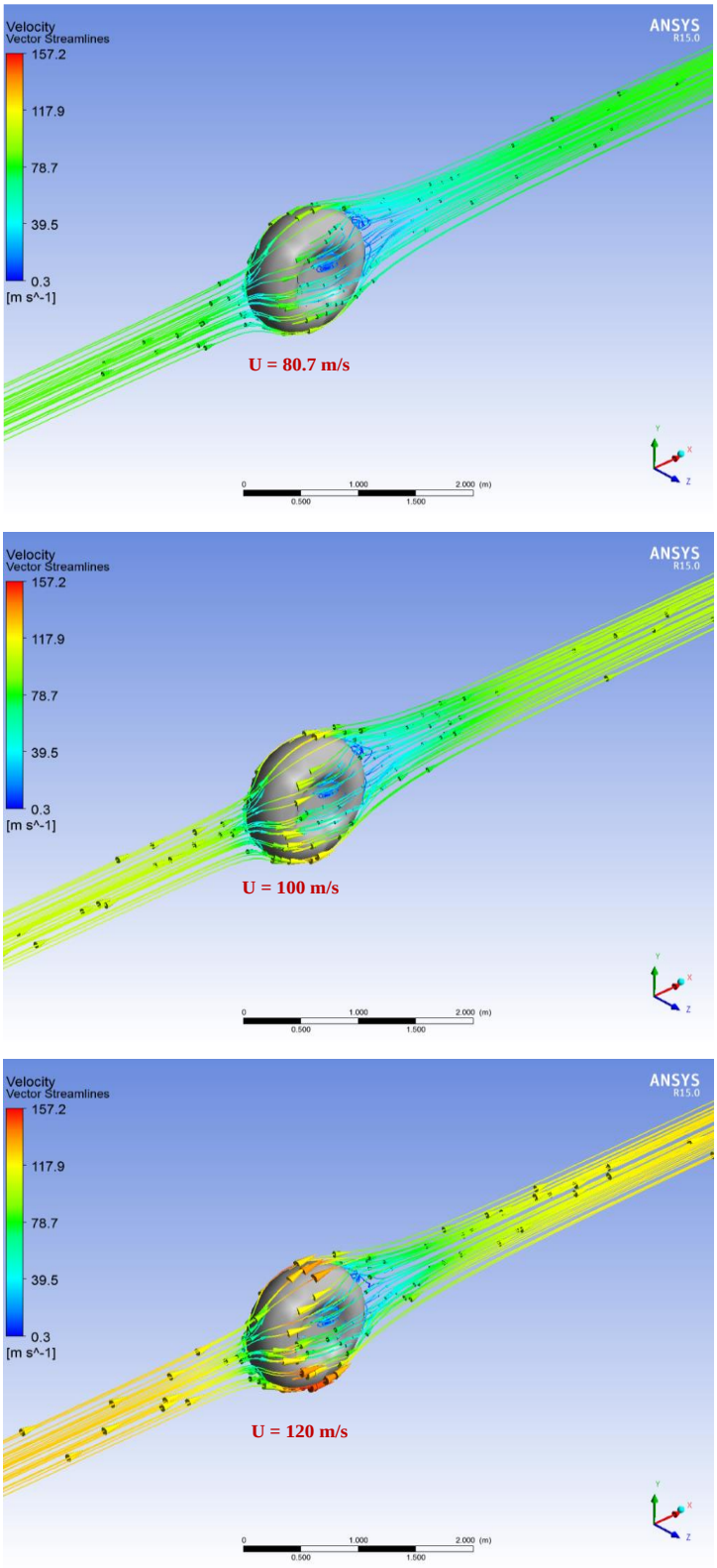

Figure 5.9 A comparison of different velocity flow profiles around the wheel at different wind speeds (vector streamline).

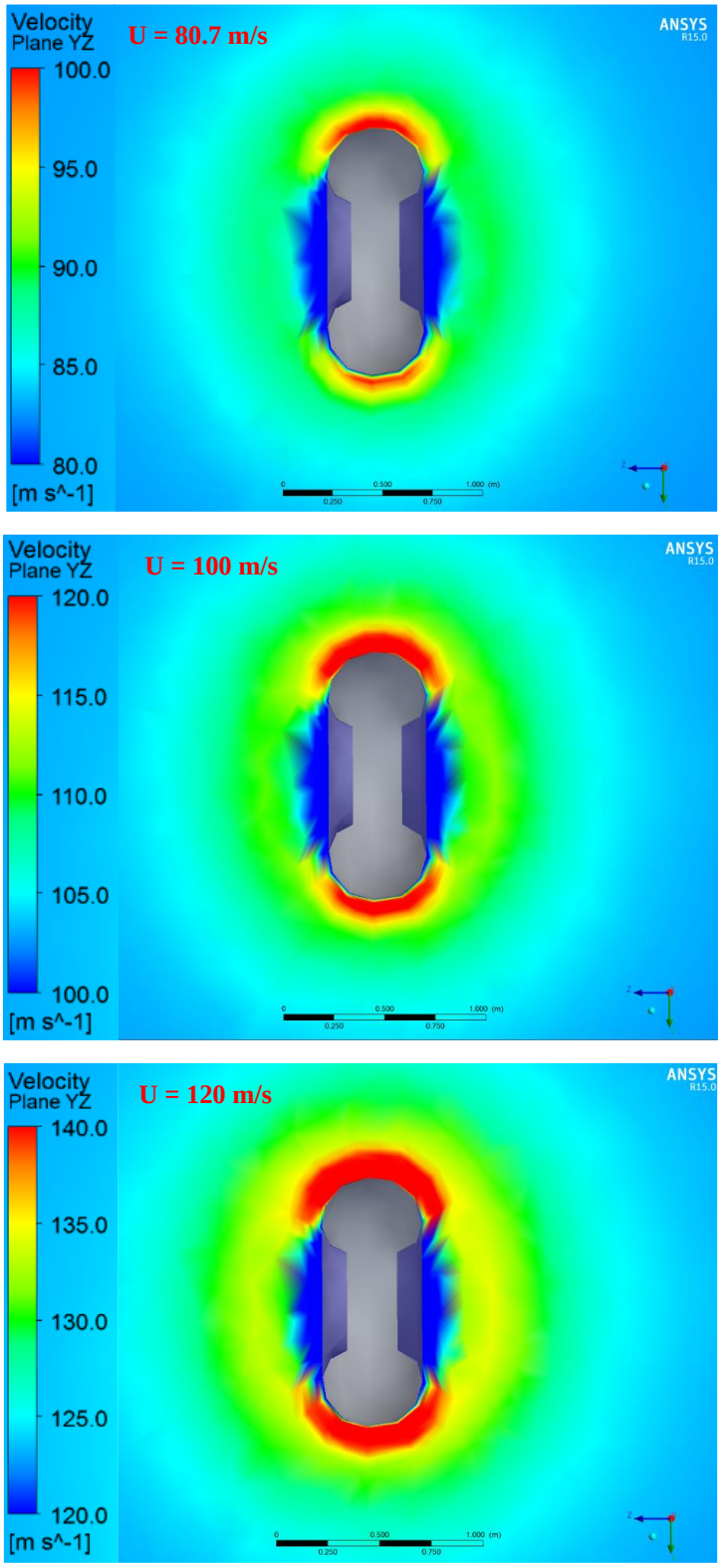

Figure 5.10 A comparison of different velocity flow profiles around the wheel at different wind speeds (plane Y-Z).

5.4.1 Translational Drag Force

The impact of wind flow on the wheel shows different characteristic force behaviour, which is speed dependant. The translational drag force at high wind speeds (100 and 120 m/s) increases over its steady state value immediately to settled down shortly afterwards. This impact force has the effect of increasing the resistance on the wheel shaft.

The translational drag force (net force in x axis) at the three different wind speeds all show steady values after a period of one second, even while the wheel accelerates. This may be because the wheel acceleration is constant.

A Comparison of the force curves and distribution profiles are presented in Figure 5.11 and Figure 5.12 respectively.

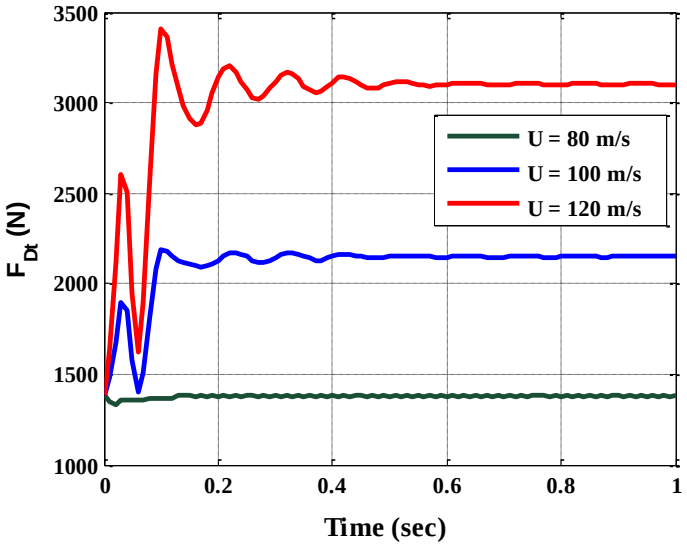

Figure 5.11 A comparison of translation drag forces vs. time with different wind speeds.

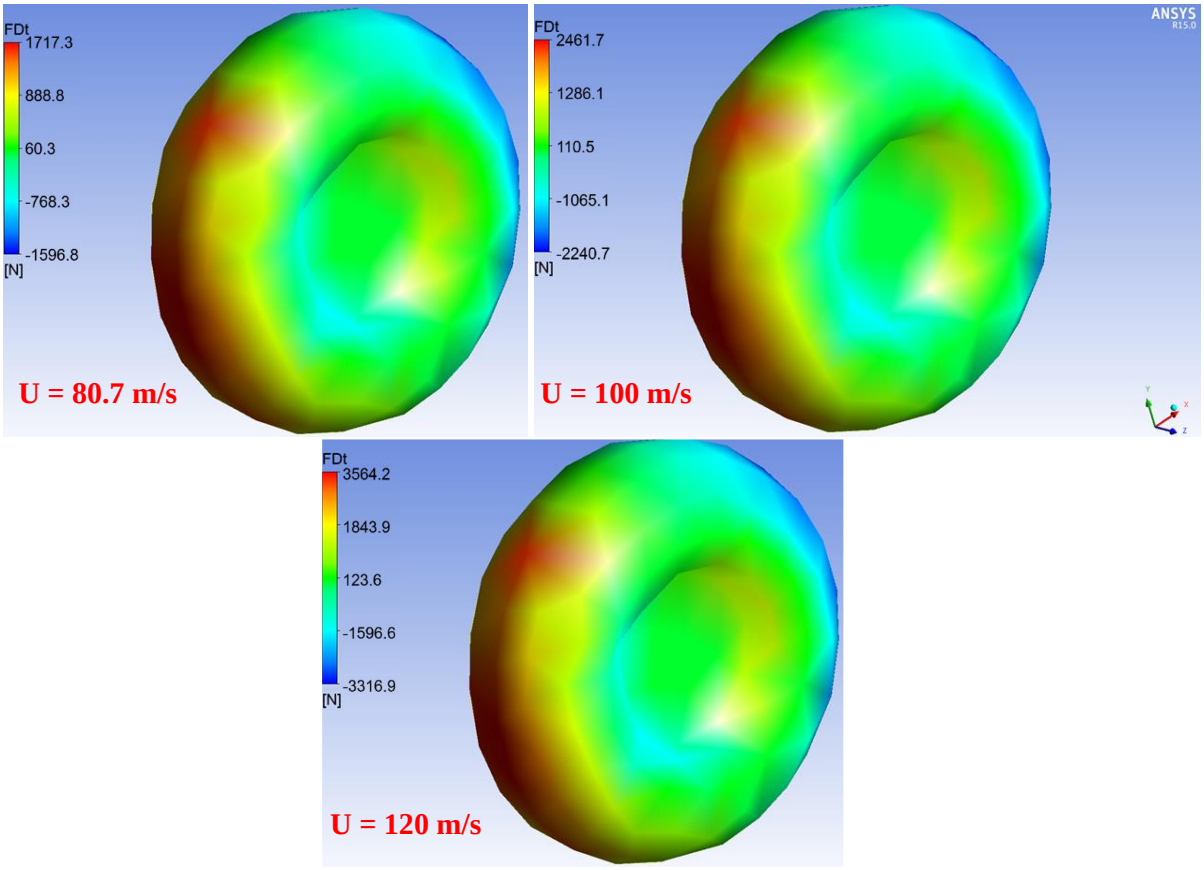

Figure 5.12 Contours of translational drag force with different wind speeds.

At a wind speed of 80.7 m/s, a drag force of 1383 N is generated by the air flow, which impinges the wheel frontal area at the moment of impact.

Once the wheel starts to rotate, it is seen that the force drops to 1331 N only to increase to 1370 N within 0.09 sec before reaching a steady state value of 1380 N, which is close to the value of a stationary wheel.

At a wind speed of 100 m/s, the force increases immediately from 1383 N to 1900 N within 0.03 seconds. After a further 0.06 seconds it has decreased to 1400 N only to

recover and increase again, reaching a steady state value of 2150 N within 0.89 seconds following some slight undulations.

At a wind speed of 120 m/s, the force behaviour is similar to that generated by the 100 m/s wind speed except with higher values. The peak value being 3410 N within 0.1 seconds which settled down to steady state value of 3100 N after 0.97 seconds.

5.4.2 Side Force - Including Rotational Drag

The rotational and side drag force (net force in z axis) increases from 64.8 N during wheel acceleration to reach a steady state at ultimate wheel rotation velocity. The resultant rotational drag force acts in the (-z) direction that because the flow acts on the rim side to push the wheel as it larger side area than the other part.

According to rotational drag force formula, it is created during wheel rotation, but as the wheel aerodynamic force is determined by experimental science, this simulation shows that the flow is producing drag force on the wheel side area because of the tyre shape, which includes breadth.

Moreover, the flow is pulled inside the hub and then re-circulated. This re-circulated flow impinges on the free air flow straight past the wheel. Therefore, the force of rotational drag here is inclusive of translation drag on the wheel sides, which is affected by wind speeds.

However, Figure 5.13 and Figure 5.14 show force curves generated during wheel acceleration and a comparison of wheel profiles at different wind speeds respectively. For all wind speeds, the force starts with the same value of 64.8 N.

At 80.7 m/s wind speed, the force increased to 105 N within 0.98 seconds before to decreasing to 99.5 N after 1.65 seconds and then rose gradually during the wheel acceleration to attain a steady state at 106 N.

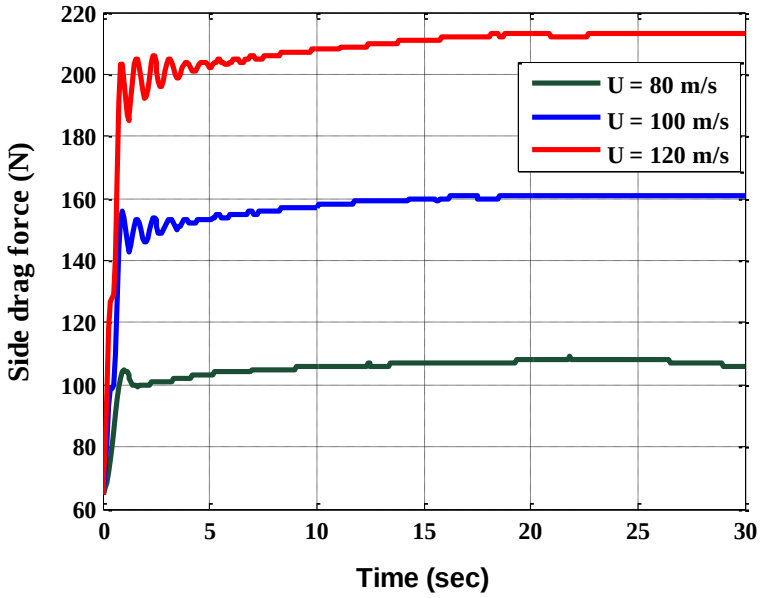

Figure 5.13 A comparison of side drag forces vs. time with different wind speeds.

At 100 m/s wind speed, the force increased to its peak value of 156 N within 0.9 seconds, which is faster and higher than the corresponding force at 80.7 m/s wind speed. The force is seen to undulate slightly whilst still increasing overall to reach 161 N toward the end of the wheel acceleration.

At 120 m/s wind speed, the associated peak value was 203 N within 0.82 seconds, which is the fastest of the three, and has relatively large waves. The steady state value at the end of acceleration was 213 N.

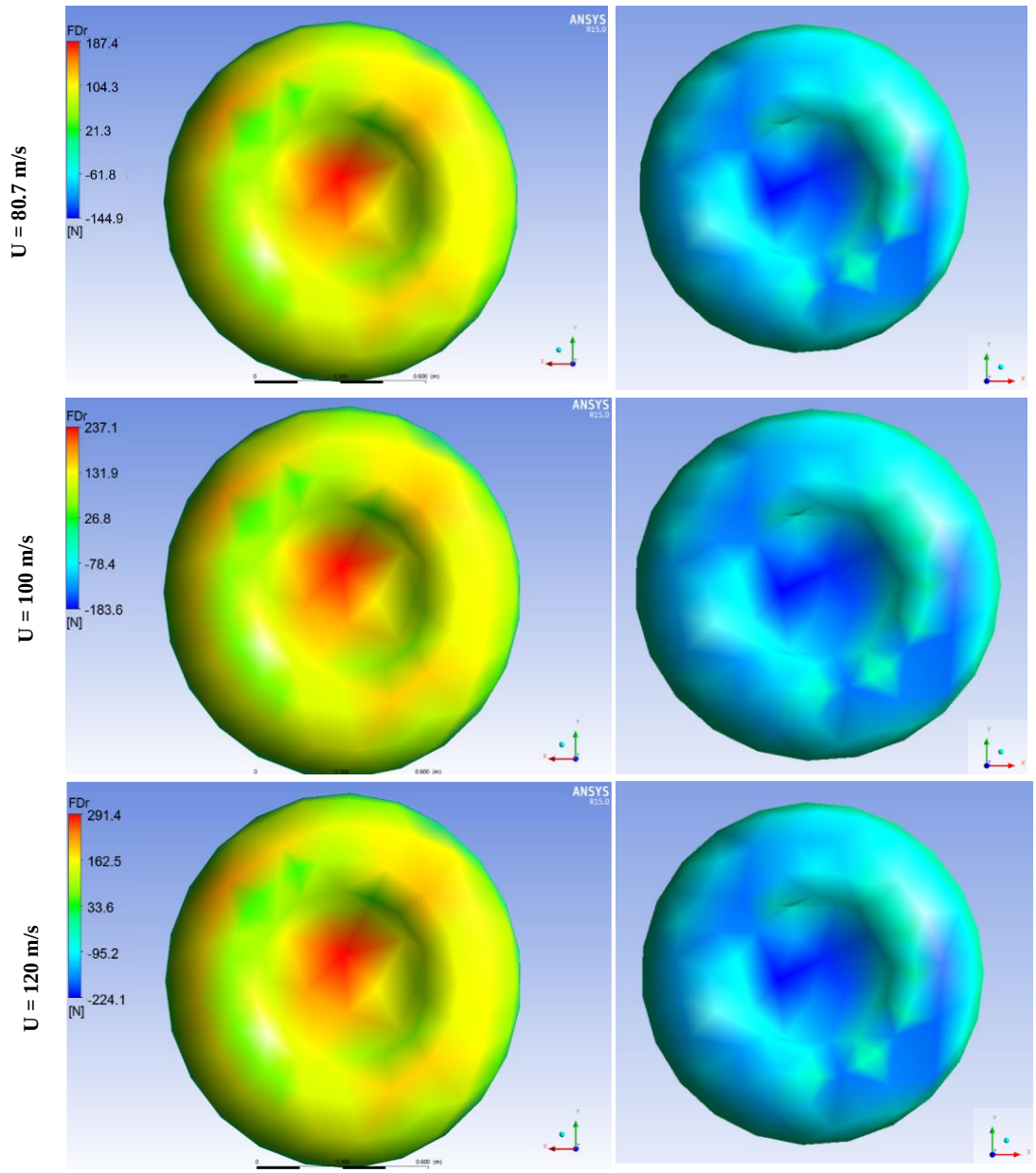

Figure 5.14 Contours of side drag force with different wind speeds.

5.3.2 Lift Force

The perpendicular pressure on the upper area of the wheel is higher than the lower pressure during the wheel rotation. As the pressure times the area creates the force, the

downward force is higher than the upward force, therefore, the lift force (net force in y axis) is downward.

The downward lift force of 90 N for all wind speeds is created immediately at wind impact, and occurs just as the wheel starts to rotate. As rotation progresses different force profiles are produced which depend on the wind speed.

Figure 5.15 shows a comparison of the lift forces for different wind speeds and Figure 5.16 shows the associated forces and pressure profiles.

In each case the force increases during the wheel acceleration stage before reaching a steady state.

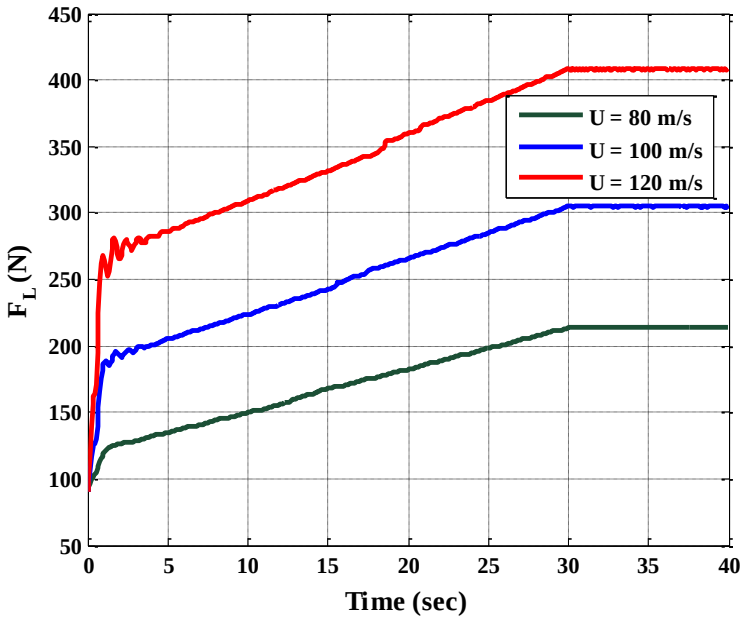

Figure 5.15 A comparison of lift forces vs. time with different wind speeds.

At 80.7 m/s wind speed, the force increases to 214 N and the maximum vortex value occurs at 16.6 sec. At 100 m/s, and 120 m/s wind speeds, the steady state value of lift

forces are 305 N and 408 N respectively, and the maximum vortexes occur at 19.05 sec and 21.22 sec respectively. However, the lift force as well as the side drag force is small compared to the translational drag and wheel weight forces; therefore, they can be ignored.

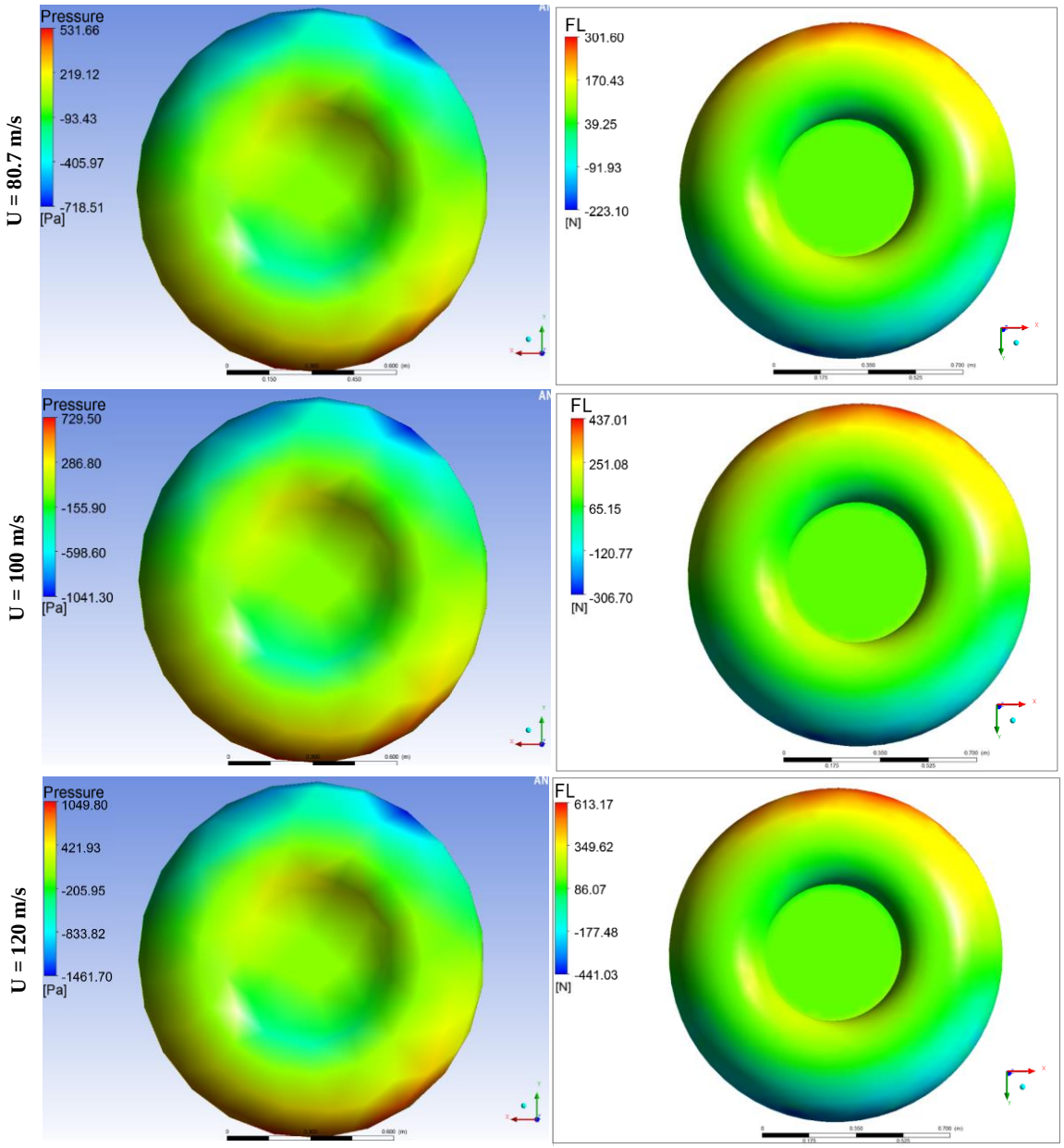

(a) Pressure **(b) Lift force**

Figure 5.16 Contours of (a) pressure and (b) lift force at different wind speeds.

5.4.5 Required Torque

The shaft rolling resistance force is required in order to calculate the total required force and hence to find the required torque. Figure 5.17 shows the rolling resistance forces for the three wind speeds considered. These forces are calculated by determining the total forces acting on the wheel shaft (Eq. 5.10) which are: wheel weight force, lift force, and translational drag force, and then applying the shaft friction coefficient (Eq. 5.11) to present the shaft rolling resistance force.

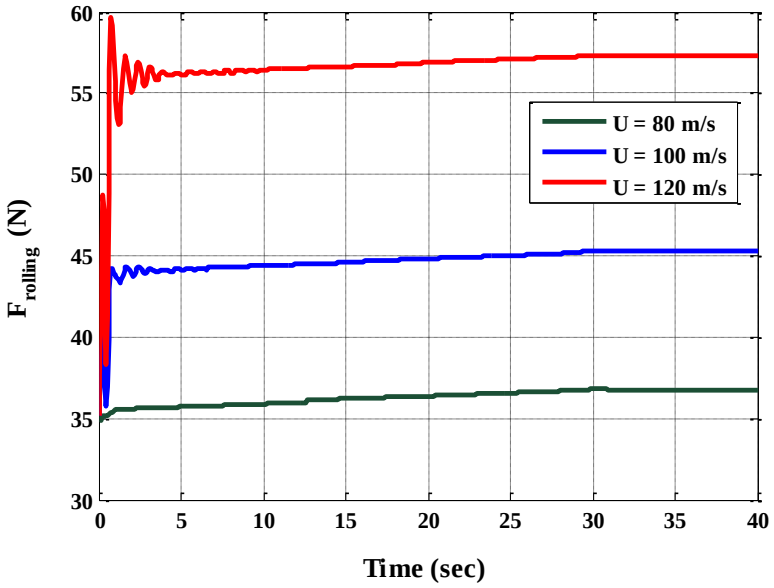

Figure 5.17 Shaft rolling resistance vs. time for different wind speeds.

Using the formula in Eq. (5.4), with 0.8 of rim radius, the required torque curves for different wind speeds are presented in Figure 5.18. However, in designing the wind turbine, it is necessary to assume a minimum wind speed to be sure the turbine has the capacity to spin the wheel in the worst-case scenario.

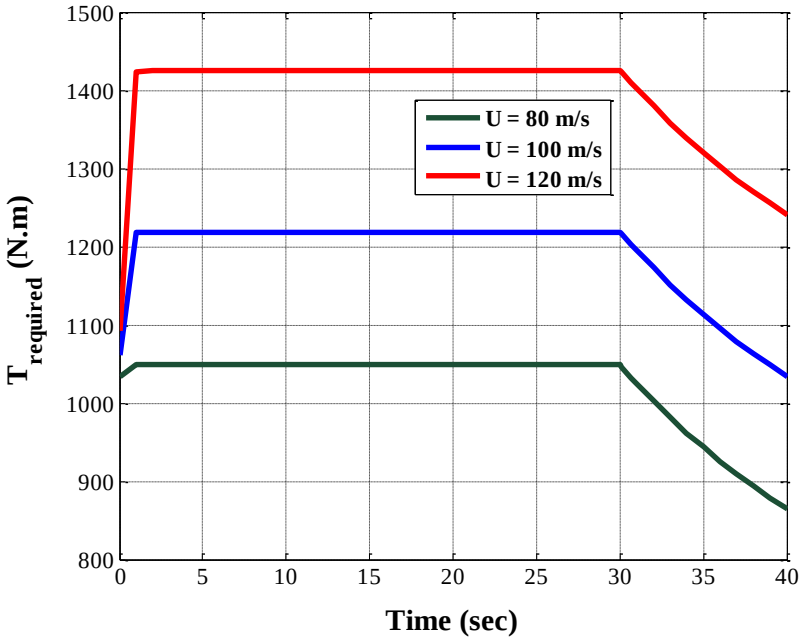

Figure 5.18 Required torque vs. time for different wind speeds.

For our case study, a torque of 1048.7 N.m is sufficient to spin the wheel to 60.5 rad/sec within 30 seconds against a wind speed of 80.7 m/s.

Increasing the wind speeds increases the wheel's resistance, and thus the required torque. On other hand, the wind turbine will produce more torque. Therefore, the wind turbine designed is based on lowest possibility wind speed able to spin the wheel to the target wheel rotation against higher wind speeds.

Chapter 6

6. Pre-rotation Wind Turbine Design and Optimization

6.1. Introduction

Based on the findings from previous chapters, the aircraft wheel should be rotated to a certain speed before landing to avoid tyre wear and smoke. The proposed solution is to pre-spin the wheel using wind turbines, as the wind speed is high when the aircraft approaches landing.

The wind power output increases significantly with the increase in wind speed; this is because the wind turbine power increases proportionally to wind speed by the power of three [135]. Moreover, the present work investigates spinning the aircraft wheel at approach by means of wind turbines. The wheels of a large aircraft are heavy and the turbines must be small to be fit into the aircraft undercarriage; on other hand, high wind speed gives the wind turbine an opportunity to produce a high output power.

There are two types of wind turbines: drag turbines, like the Savonius turbine and lift wind turbines, like the Darrieus turbine [136]. The literature shows that the Savonius turbine has many advantages compared to other wind turbines; as it can receive the wind from any direction and has a high start torque [68]. The Savonius rotor has a simple design and can be used in steady or turbulent wind. Also, it produces a continuous torque as the force on the rotor is generated immediately the wind blows [71].

In this chapter, different types of Savonius turbine have been simulated against high wind speed using ANSYS CFX in order to ascertain the means of obtaining optimal rotation speed in relation to a turbine size and shape that would be acceptable in aviation. Moreover, one of the Savonius turbines has been improved by adding an obstacle, which eliminates the negative force on the returning blade so as to improve the turbine efficiency.

6.1.1 The Savonius Rotor Principle

The Savonius wind rotor was patented by the Finnish engineer, S. J. Savonius in 1922 and it is usually used to drive a pump or generator. Figure 6.1 shows the basic Savonius vertical axis wind turbine. The principle of this turbine is that a drum has been divided into two sections in opposite directions and fixed onto a shaft [137].

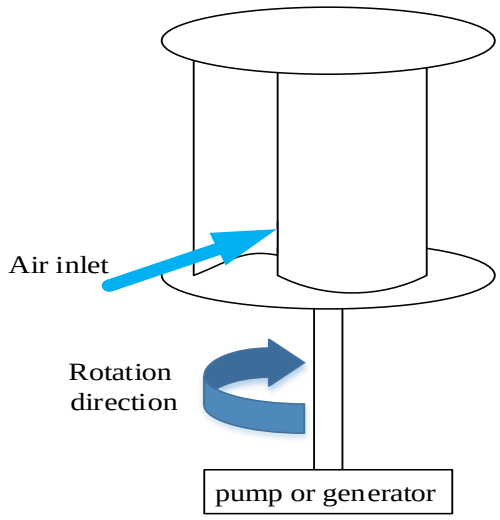

Figure 6.1 Basic Savonius vertical axis wind turbine.

Figure 6.2 shows the Savonius rotor principle. Each drum (bucket/blade) catches the wind flow on its concave surface which produces force which rotates the rotor, at the same time, the other drum half is facing the wind with its convex surface and produces less force than the other drum half. The wind splits over the convex surface in some rotation positions, part of the wind goes to the other blade (concave surface) to add extra positive force for the rotation. However, the drag force at the concave surface is higher than at the convex surface, the difference between these drag forces (net drag force) causes the rotor to rotate continuously as the process repeats.

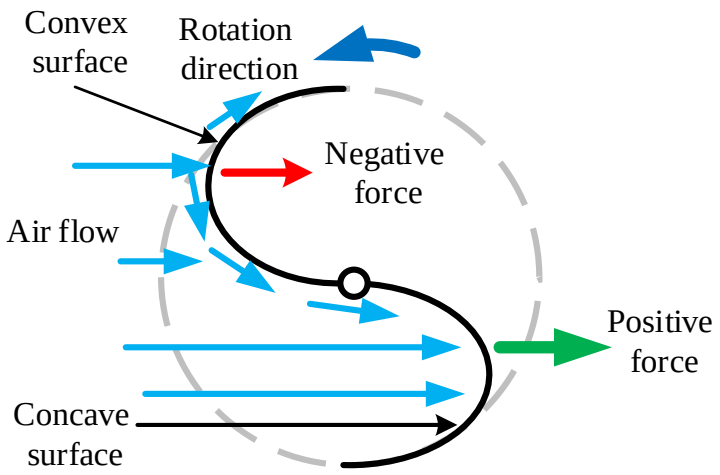

Figure 6.2 The Savonius Rotor Principle.

There are many versions of the Savonius rotor with many stages and more than two blades, as shown by Figure 6.3. Usually, the two-stage Savonius rotors are perpendicular to each other by 90 degrees to obtain a smoother rotation. In addition, using many blades at every stage also requires the symmetry for the same reason [68].

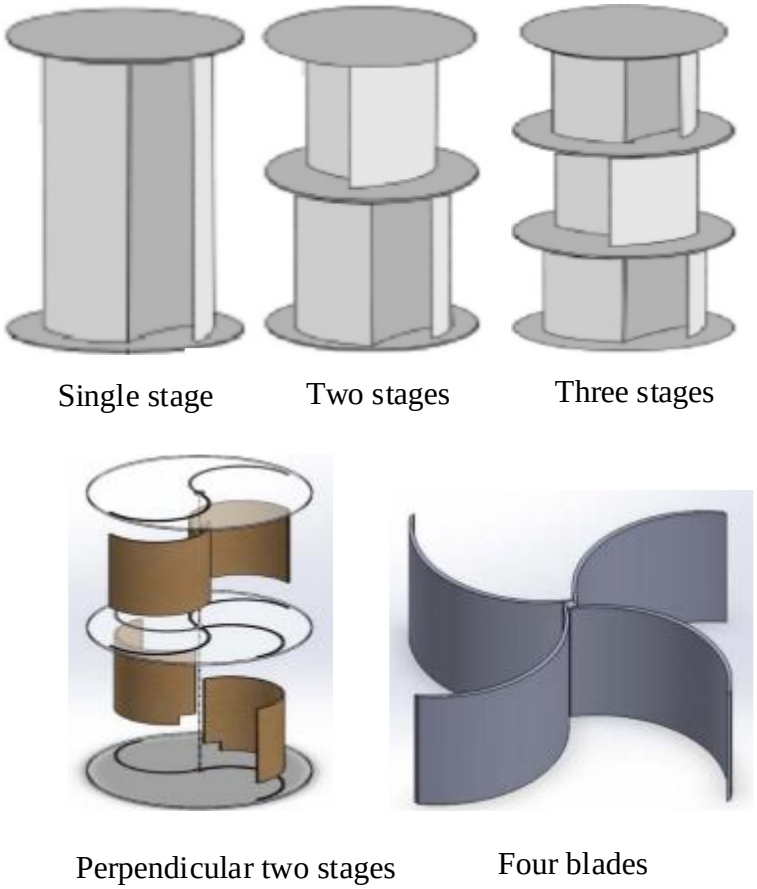

Figure 6.3 Savonius rotors with many stages and blades [138, 139].

The literature shows that two stage rotors are more efficient than a single stage; and two-blade rotor efficiency is higher than with three and four-blade rotors. Mahmoud et al. (2012) [74] conclude that the efficiency of three blade rotors is about 60%, compared to the two blades; and doubling the stages increases the efficiency by about 10% compared to a single stage rotor.

6.2. The Mathematical Model

To design the wind turbine, it is essential to know the input data and the required output. In our case, the target rotational speed is the main requirement. In addition, the aircraft wheel is heavy and it requires high torque to rotate. However, as stated in the previous chapter, we do know the required torque to spin the wheel and the turbine must exceed this when it starts to rotate the wheel, and we know the target rotational speed. These requirements simplify the design calculations for the turbine. Figure 6.4 shows the basic parameters required to calculate power, torque and required rotational speed for the Savonius rotor.

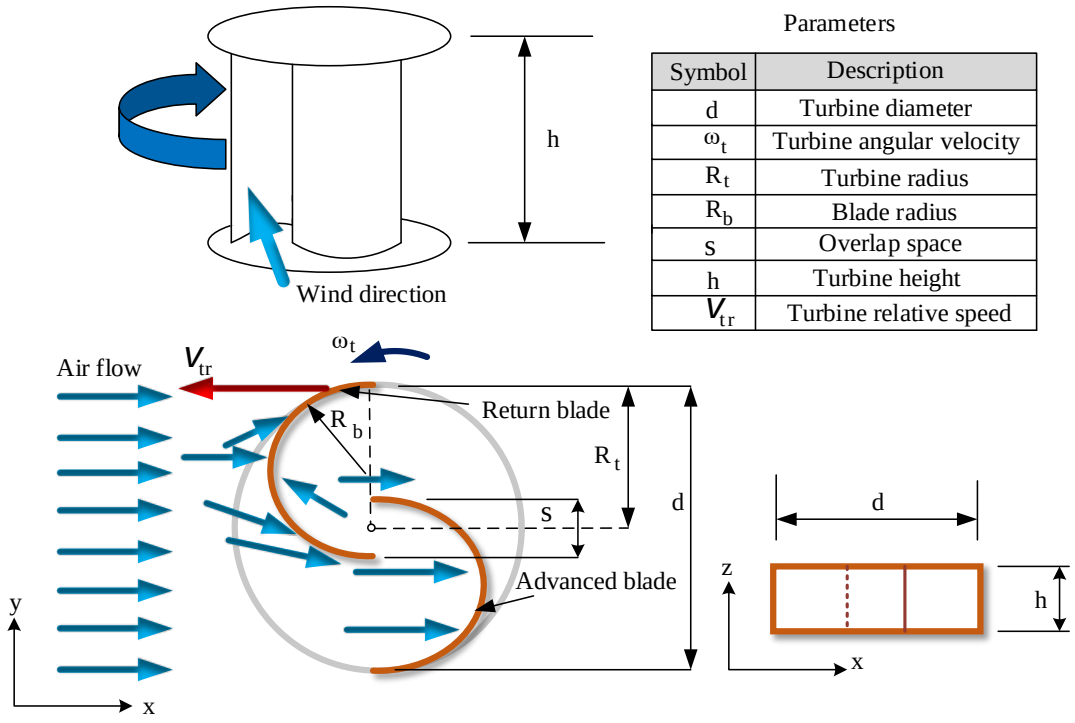

Parameters

Symbol	Description
d	Turbine diameter
ω_t	Turbine angular velocity
R_t	Turbine radius
R_b	Blade radius
s	Overlap space
h	Turbine height
V_{tr}	Turbine relative speed

Figure 6.4 Design parameters of two bucket Savonius rotors.

The rotor has a diameter, d, which is along the wheel rim (in our case, $d =$ rim diameter), this is so as to use the full acceptable dimension to produce more torque. The rotor diameter may be slightly higher than the rim but not equal to the whole wheel diameter in order to avoid any contact with the runway when the tyre deflects at touchdown.

All blades are semi-circular with a radius R_b. The distance of the gap between adjacent blades, s, allows the airflow to reflect from the concave surface of the advanced blade to the concave surface of the return blade to push it to the required rotation direction, which will reduce the negative drag force. Nevertheless, increasing the gap will decrease the concave area of the blades; therefore, it should be small as possible. The experiments show that overlap ratio ($e = \frac{s}{d}$) increases the turbine efficiency when it is in a range of 0 to 0.15 [74, 82, 83]

6.2.1 Wind Turbine Power

A wind turbine converts some of the kinetic air energy to mechanical energy, which is in the form of rotation. According to Betz's law, the maximum power of a wind turbine is only 0.593 of the power available from the wind. That is because the wind speed decreases when it passes through the turbine blades [140]. The percentage of turbine power to wind power is called the turbine power coefficient (wind turbine efficiency) and its limit varies from one wind turbine to another. The Savonius rotor's maximum power efficiency reaches to above 0.3 of the available wind power [141]. The power coefficient is expressed by:

$$C_p = \frac{P_t}{P_w} \qquad 6.1$$

where C_p is the power coefficient, and P_w and P_t are the power of the wind and turbine respectively (watt).

The wind power passing through the turbine can be calculated as:

$$P_w = \frac{1}{2}\rho_A A_s U^3 \qquad 6.2$$

where, ρ_A is the air density (kg/m^3), U is the wind speed (m/sec), and A_s is the rotor swept area (m^2). Here, $A_s = dh$, where, d is the turbine diameter (m), and h is the turbine height (m). The vertical-axis wind turbine (VAWT) swept area is the frontage area that is facing the wind (square area) while the horizontal-axis wind turbine (HAWT) swept area is the circle area not including the blade width. Figure 6.5 shows the difference between the swept areas for horizontal-axis and vertical-axis wind turbines.

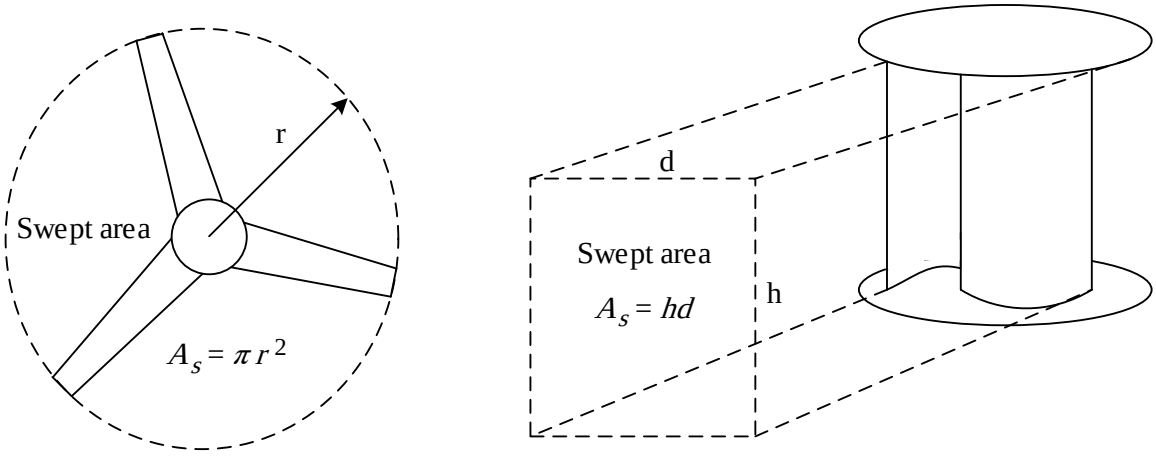

Horizontal-axis wind turbine

Vertical-axis wind turbine

Figure 6.5 Swept areas for horizontal-axis and vertical-axis wind turbines.

The wind power formula shows that the wind power will increase significantly in line with increases of wind speed (Eq.6.2).

Substituting Eq. (6.2) in Eq. (6.1), the turbine power formula will be as follows:

$$P_t = \frac{1}{2}\rho_A C_p A_s U^3 \tag{6.3}$$

The turbine power coefficient C_p depends on the blade angle of attack, the type of gas flow, the turbine tip speed ratio (TSR), and the blade shape. Moreover, a study by Glauert (1935) [142] shows that increasing the number of wind turbine blades leads to a decrease of the wind passing through it, thus producing less power. For this reason, the maximum number of blades in this model is three. However, the Savonius turbine has a zero angle of attack, and in this model, half-circular blades of different sizes have been used, therefore, only the TSR is considered for the primary design.

The turbine tip speed ratio (TSR) can be found by this formula:

$$TSR = \frac{R_t \omega_t}{U} \tag{6.4}$$

where, ω_t is the turbine rotational speed (rad/sec). Figure 6.6 shows the relation between the power coefficient and the tip speed ratio of different wind turbines [141]. The reason for using TSR to optimize the wind turbine efficiency is that when the rotational speed of the rotor increases, the amount of the air passing through the turbine will lessen, resulting in less power, therefore, every wind turbine has an optimum TSR. As shown by the figure below, the Savonius has the best efficiency at about $TSR = 0.8$; unfortunately, the required TSR in our model is low, which means less power.

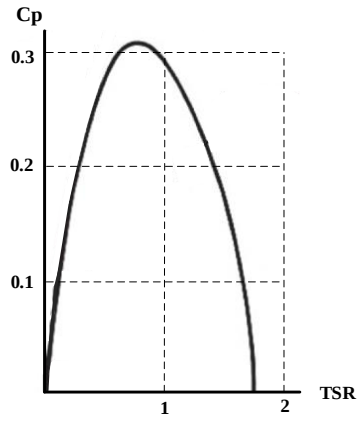

Figure 6.6 Savonius turbine power coefficient (C_p) as a function of tip speed ratio (TSR).

6.2.2 Wind Turbine Torque

The Savonius turbine's torque is the result of pressure drop on each blade surface. The blade's concave surface has the higher pressure. Another perspective is that the Savonius is a drag turbine, where the higher drag force acts on the blade's concave surface. The return blade also has drag force on the convex surface, but this is less. The difference between the forces rotates the rotor around its centre (shaft). Figure 6.7 shows a simple diagram of the drag and lift forces on the turbine. However, the turbine's mechanical torque can be calculated as:

$$T_t = (F_{ad} - F_{rt})\ \frac{R_t}{2} \tag{6.5}$$

where T_t is the mechanical torque produced by the turbine (N.m),and F_{ad} and F_{rt} are the blade's drag forces for the concave and convex surfaces respectively (N). F_{ad} represents the positive force and F_{rt} is the negative force. Therefore, there are two components of

the torque: the advanced blade torque, which drives the turbine; and the return blade torque, which is the resistance. The total torque is the sum of the two torque components.

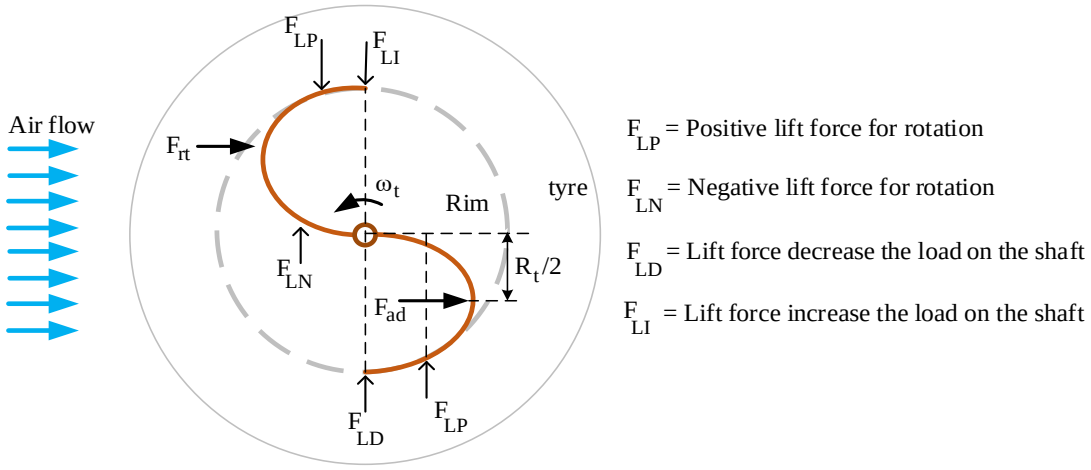

Figure 6.7 Drag and lift forces on the Savonius rotor.

There are also little lift forces created on the blades which can be positive or negative for turbine rotation depending on the position of the force on the blade and the distance from the rotation shaft (force arm), and which produce a small positive or negative torque. If the force arm is zero, the lift will decrease the load on the shaft (wheel weight) if it is going up and vice versa [143].

Rewriting Eq. (6.5) with respect to the drag force formula and using the mechanical torque coefficient instead of two drag coefficients for the advance and return blades is as follows:

$$T_t = \frac{1}{4}\rho_A C_t A_s U^2 R_t \tag{6.6}$$

where, C_t is the turbine's mechanical torque coefficient; and, in relation to the turbine's TSR and power coefficient can be expressed as:

$$C_t = \frac{C_p}{TSR} \tag{6.7}$$

However, the main requirement in this design is the wheel's rotational speed. The torque, rotational speed and the output power of the turbine is governed by this formula [140]:

$$\omega_t = \frac{P_t}{T_t} \tag{6.8}$$

From this formula, we can know the required turbine torque as the angular velocity at steady state is known and the turbine power at this rolling level can be calculated as C_p and can be assumed from the curve of the relation between C_p and TSR. However, as the wind turbine is connected to a heavy wheel, the turbine will not start to rotate until it produces sufficient torque, which must be higher than the required torque to spin the wheel from rest. For this, Eq. (6.8) will be rewritten and consider the required torque to spin the wheel (friction torque) to be as follows:

$$\omega_t = \begin{cases} \frac{P_t}{T_t - T_w} & if \quad (T_t - T_w) > 0 \\ 0 & if \quad (T_t - T_w) \leq 0 \end{cases} \tag{6.9}$$

where, T_w is the required torque to spin the wheel (N.m). There are two ways to find T_w; by the method described in the previous chapter; and the other method is by simulating the turbine with and without the wheel to find the turbine's angular velocity for both cases and then use Newton's second law as follows:

$$T_{net} = I\dot{\omega} \tag{6.10}$$

where, T_{net} is the net torque that causes the wheel rotation (N.m). Here, ($T_{net} = T_t - T_w$). I is the wheel's moment of inertia (kg.m^2) and in cases where the turbine is not connected to the wheel it can be used to calculate the turbine torque. $\dot{\omega}$ is the angular acceleration for the turbine or the wheel (rad/s^2). The Eq. (6.10) can be used to calculate the generated torque from the turbine when the turbine is not loaded on the wheel; in this case, $T_w = 0$, and $I\dot{\omega}$ are for the turbine only.

However, in our model the wind speed is assumed to be constant, therefore, only the turbine's swept area increases the turbine output power. Moreover, the turbine diameter is controlled by the wheel size. For this reason, the main factor for our design is the turbine height (h), as it should be small enough to fit into the aircraft undercarriage.

Substituting Eq. (6.3) and Eq. (6.4) in Eq. (6.9), with regard to the turbine height is as follows:

$$h = \left[\frac{(T_t - T_w)\,\omega_t}{\frac{1}{2}\rho_A C_p U^3}\right] / 2R_t \tag{6.11}$$

This formula will only give the primary turbine height in the simulation because the formula includes the wheel friction torque, which is a function of the wheel's moment of inertia and angular acceleration time, and that means less torque is required after sufficient time.

6.2.3 Improving Drag Turbine Efficiency

The principle of the drag turbine is based on the net force (positive force minus negative force) which is rotating the blades. Therefore, minimizing or eliminating the negative

force will improve turbine efficiency. Moreover, increasing the wind speed on the blade's concave surface by using a concentrator will further increase the efficiency.

Figure 6.8 shows the Savonius turbine with an obstacle to avoid negative force and concentrate the wind on the blade's concave surface. One of the vertical Savonius turbine's advantages is that it can receive the wind from any direction, but with an obstacle it will lose this advantage, as it can only receive the wind from one direction [144].

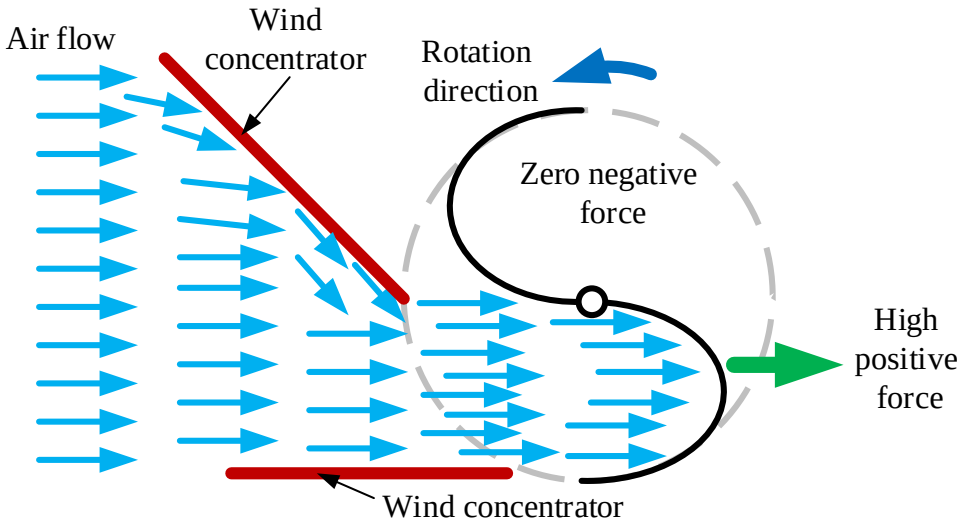

Figure 6.8 Savonius turbine with wind concentrator.

Some previous experiments show that the turbine efficiency can be improved by adding an obstacle. The efficiency varied, depending on angle of the obstacle/position of the obstacle. Rus (2012) [144] simulated the Savonius turbine with an obstacle and

concluded that the turbine efficiency increased up to 20% while Mohamed et al. (2011) [145] found that the efficiency increased up to 40%.

In our case study, the drag turbine can be improved with an obstacle, but not if the shape is bulky as an aerodynamic shape is important in aviation field. In our opinion, the acceptable shape is shown by Figure 6.9.

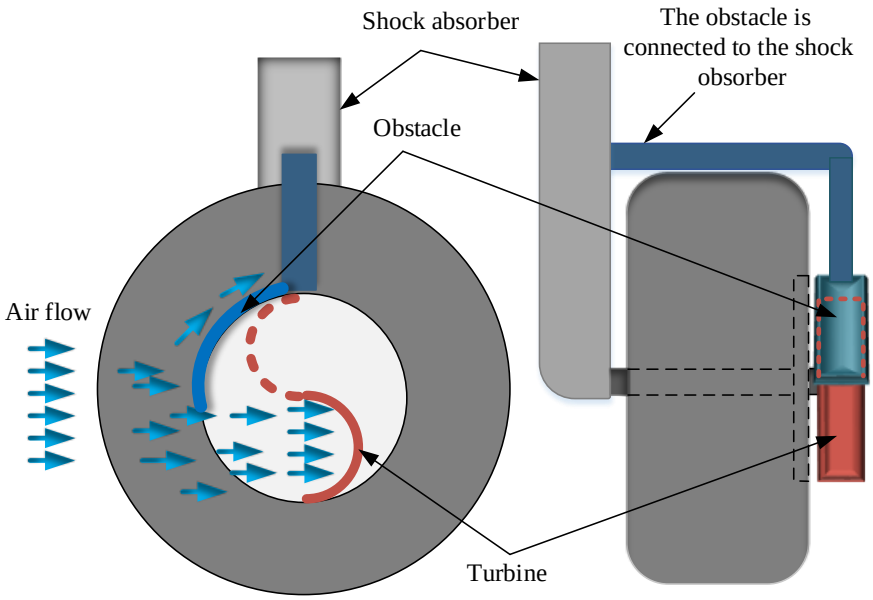

Figure 6.9 The proposed use of the turbine with obstacle for aircraft wheel.

The obstacle is connected to the shock absorber and not in contact with the wheel or drag turbine. The obstacle has an aerodynamic shape to produce less drag on the landing gear, at the same time preventing the negative force on the turbine blade. The obstacle can be semi-circular with an endplate to cover the upper part of the turbine. Here, we preferred the obstacle shown, which is a quarter circle, to avoid extra weight.

6.3. Simulation Model

6.3.1 Simulation Overview

The overview of the simulation model is shown by Figure 6.10. The wind speed is assumed to be constant for all simulations at 80.7 m/s which equals to the approach speed of a Boeing 747-400 [92]. The wind speed assumption is based on zero wind heading the aircraft, which means it is less than any possible wind speed. Also, it is assumed that the aircraft wheel extended 45 seconds before touchdown on the runway. In this case, the wheel angular velocity should reach the required speed during this time, even if it is still accelerating. The target rotational speed is 60.5 rad/sec. The wheel will rotate freely to find out its angular velocity and other related outputs. The simulation has been run five times for five wind turbine models with the same boundary conditions.

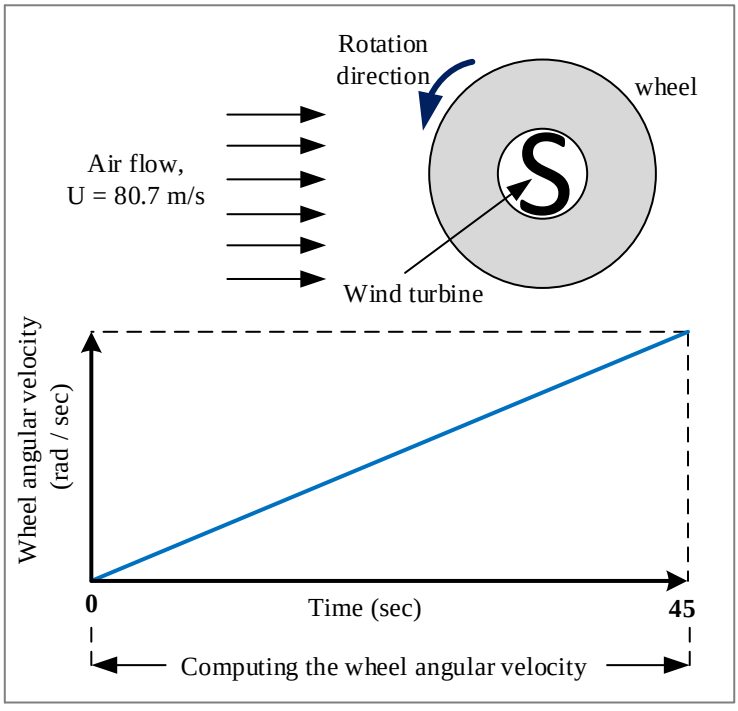

Figure 6.10 Simulation model overview.

6.3.2 Geometry Modelling

Five wind turbines and wheel 3D geometries have been modeled using an ANSYS modeler design, as shown in Figure 6.11. Every turbine has been connected to the wheel and simulated at the same boundary conditions using ANSYS CFX. In a real operation, the turbine should be attached to the wheel rim; but in this model, the turbine is connected by a shaft to the rim for simplicity.

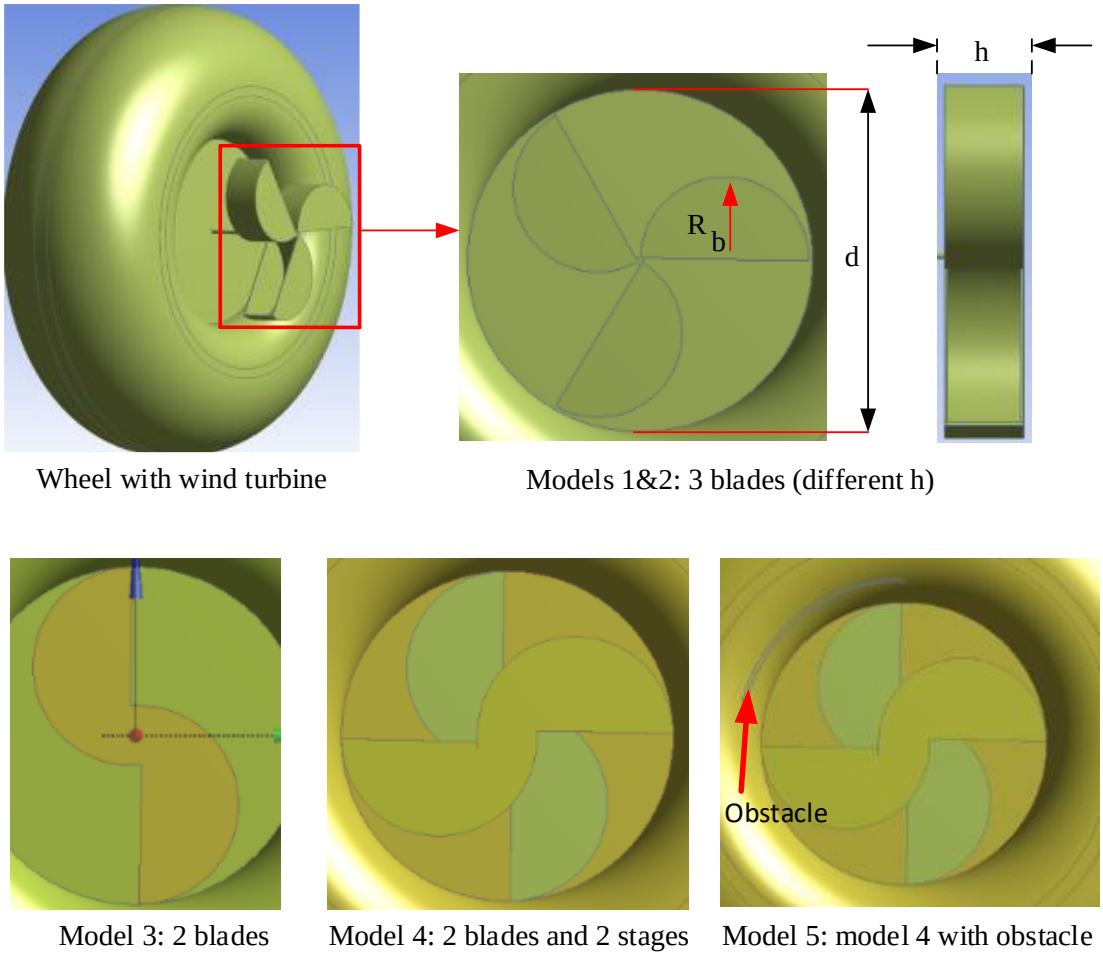

Wheel with wind turbine

Models 1&2: 3 blades (different h)

Model 3: 2 blades

Model 4: 2 blades and 2 stages

Model 5: model 4 with obstacle

Figure 6.11 Geometry of five wind turbine models and wheels.

Model 1 consists of three blades without a gap, and Model 2 is half the height of Model 1 but with other dimensions the same. This is so as to discover the percentage of turbine efficiency reduced in relation to its height, and then to choose the optimum height for every turbine that allows for the required rotation speed.

Model 3 consists of two blades with a gap to increase turbine efficiency. This model will be compared to those with three blades to check the effect of increasing the turbine blades. Model 4 has two blades and double stages perpendicular to each other. However, although the total height of Model 4 is equal to that of Model 3, model 4 has two stages, compared to only one stage in model 3. Model 5 is the same as model 4; however, an obstacle has been added to eliminate the negative drag forces. From Model 5, results will check the effect of adding an obstacle on turbine efficiency. Table 6.1 below shows the turbine model dimensions (mm), all the blades are semi-circular in shape and all the turbines have the same diameter and thickness which are 510 mm and 3 mm respectively.

Table 6.1 Wind turbine dimensions.

	Model 1	**Model 2**	**Model 3**	**Model 4**	**Model 5**
Total height, h	100	200	200	200*	200*
Blade radius, R_b	127.5	150	150	150	150
chord length ($2R_b$)	225	300	300	300	300
Overlap space, s	0	0	8	8	8
Overlap ratio, e	0	0	0.0156	0.0156	0.0156

*every stage 100 mm.

6.3.3 Mesh Generating

To find the forces and momentum acting on the wind turbine and then the required output, a fully integrated six-degree-of-freedom rigid body solver in ANSYS CFX has been used in this simulation model, giving wheel mass and a defined moment of inertia. The turbine mass has been ignored as it is assumed to be very small compared to the wheel mass (184.4 kg) [106]. However, all the models contain two domains as shown by Figure 6.12, except Model Five which has the additional domain of an immersed solid (the obstacle).

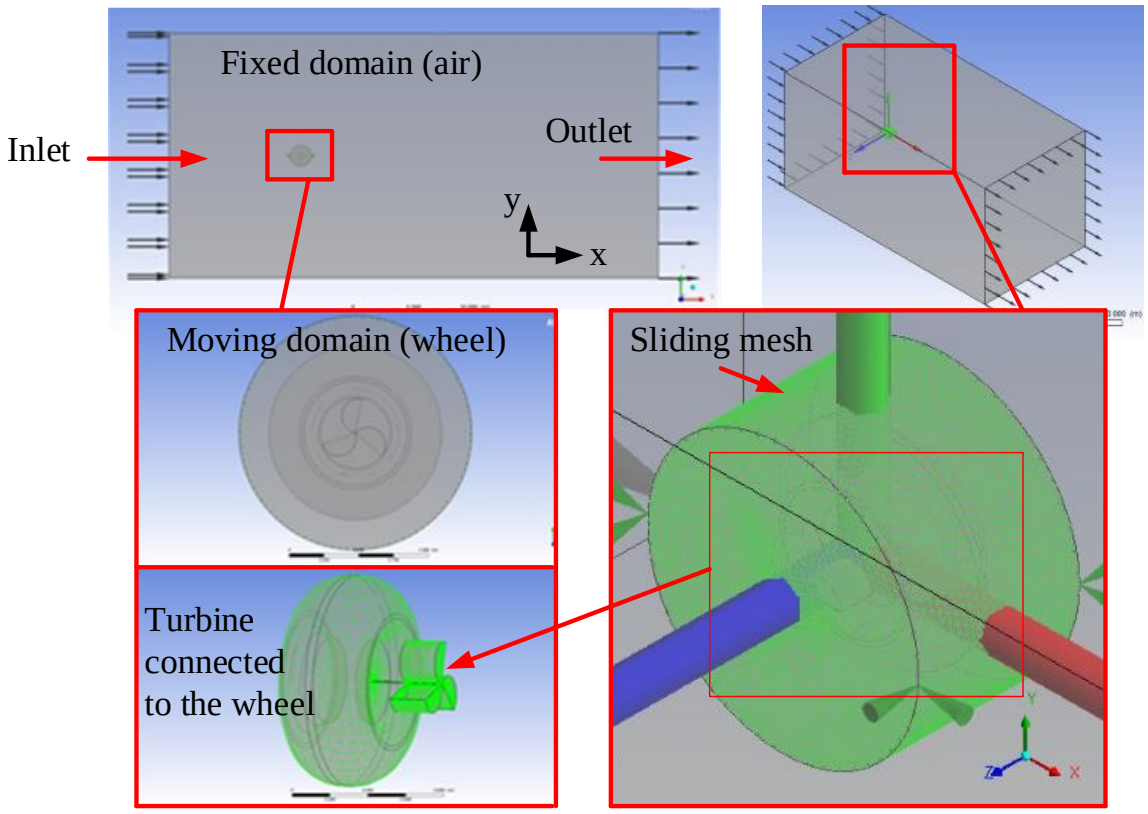

Figure 6.12 Fixed and moving domains.

The mesh strategy uses two different meshes; rotating and far field; the far field is the air domain which has the dimensions of a 20 m x 20 m inlet area which is 40 m long. The wheel is the other domain (or 'sub-domain') which has dimensions of 1.6 m diameter and 1m width.

The two domains (air and wheel) were combined using interfaces which are used to connect different types of domains (fluid and solid). Figure 6.13 shows the mesh model and Table 6.2 shows the mesh statistics.

The sub-domain (air domain) is simulated using the 'Rigid Body Solution', which means a solid object (wheel and turbine) rotates through the airflow influence with its own coordinate system without any deformation [146].

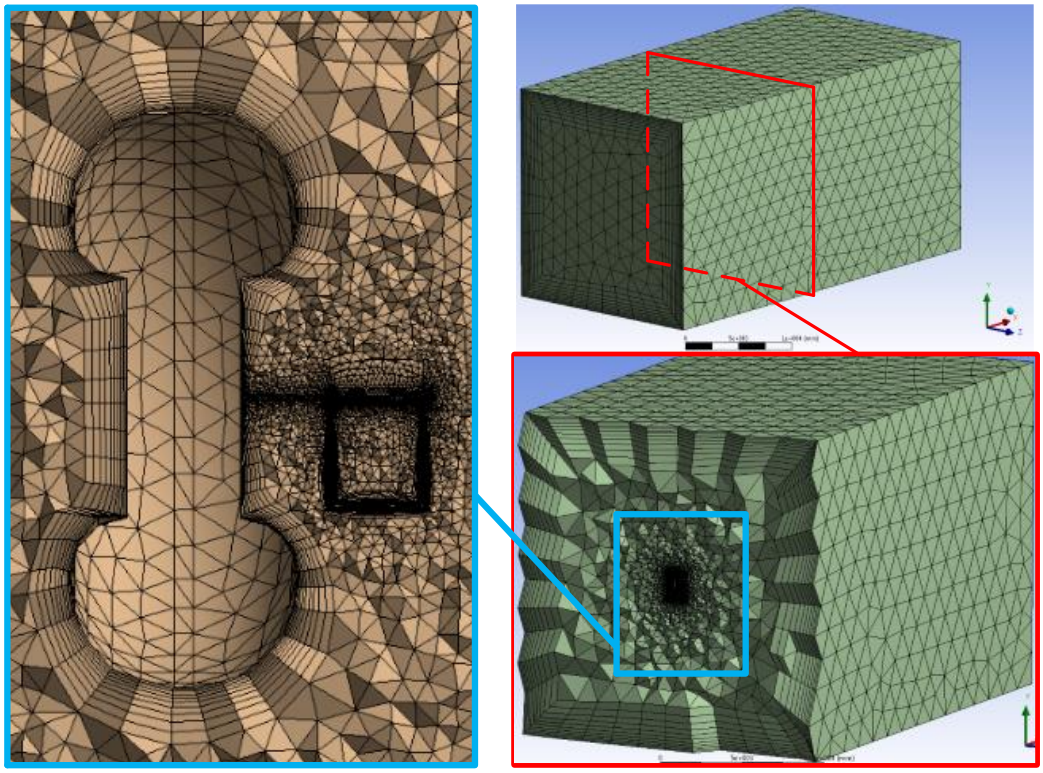

Figure 6.13 Mesh model of the domains.

Table 6.2 Mesh statistics (Models 1, 2 & 3).

	Model 1		Model 2		Model 3	
	Air	Wheel	Air	Wheel	Air	Wheel
Nodes	46256	160888	46256	134184	39023	145004
Elements	220451	511250	220451	428949	178759	497469
Tetrahedrons	201731	307270	201731	260849	159739	329809
Prisms	18720	203980	18720	168100	19020	167660
Faces	11916	30100	11916	26092	10494	24526
Min. Orthogonality Angle [131]	37.8	24.3	37.8	23.4	41.4	29.2
Max. Expansion factor	15	18	15	13	13	16
Max. Aspect Ratio	29	98	20	88	27	123

Table 6.2 Mesh statistics (Models 4 & 5).

	Model 4		Model 5		
	Air	Wheel	Air	Wheel	Obstacle
Nodes	39023	218282	39023	251674	1735
Elements	178759	708014	178759	891642	4718
Tetrahedrons	159739	433754	159739	610142	4718
Prisms	19020	274260	19020	281500	----
Faces	10494	35184	10494	35916	3452
Min. Orthogonality Angle	41.4	30.1	41.4	29.7	42.2
Max. Expansion factor	13	18	13	14	9
Max. Aspect Ratio	27	346	27	378	7

The physical model of the flow is specified as a transient state with zero turbulence conditions using Reynolds-Averaged Navier-Stokes equations. The turbulence model is shear stress transport (SST), which is generally suitable for many applications. In this model, the total energy technique has been used, which is suitable for high speed energy, therefore, it should also be suitable for the high speed flow [130, 131].

A method of 'Patch Conforming' has been used to generate the mesh with elements in the form of tetrahedrons. For more accuracy, the flow prismatic layers are constructed near the surfaces 'walls, wheel and turbine' using the 'smooth transition' option [129]. In addition, the wall surfaces are rough that because the SST gives accurate results when the

flow separates on soft surfaces [130]. The regime of the flow is subsonic and the static temperature is set at 288 K. The reference and relative pressures are set at $1.013x10^5$ and 1 Pa respectively.

6.3.4 Solution Convergence

The results are carefully checked by tracking the convergence of the solution. Figure 6.14 shows the residual values for the first simulation. The solutions are considered converged as the residuals are decreased to lower than 1E-3 with a low imbalance for all the simulations.

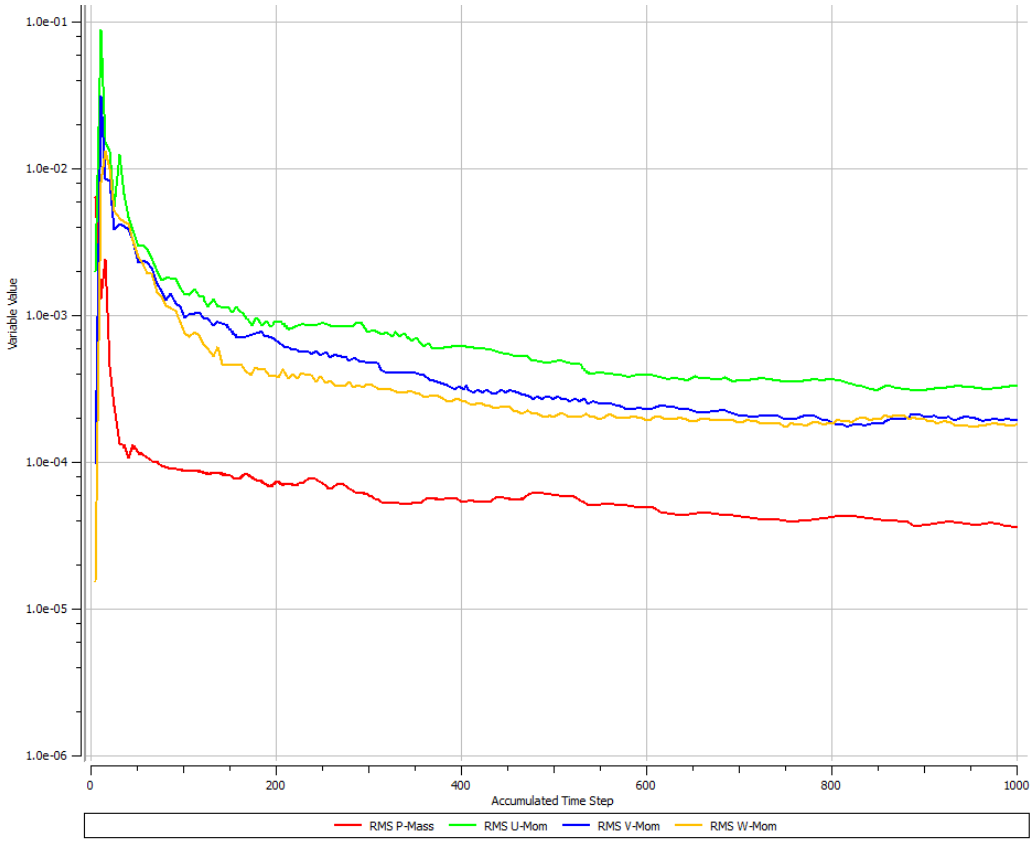

Figure 6.14 Variations of the residual for the pressure and the velocity components vs. accumulated time step.

6.4. Results and Discussion

The available wind power for all models is 32861 watts (Eq. 6.2), except Model 2, which is 16430.5 watts, as it has half a swept area. In general, the turbine efficiencies are low because they relate to tip speed ratios which are also low; and this is because the turbines are loaded by the heavy wheel.

Figure 6.15 shows the wind velocity profiles and the resulting pressure distribution as the wind passes through all the turbines. Figure 6.16 shows the top view of the wind velocity profile on the wheel and turbines.

At the moment of wind impact on the turbine blades, high forces are generated within fraction of seconds, which lead to a related acceleration of the wheel. Figure 6.17 shows the enhancement of the wheel acceleration and the turbines' generated torque. However, a high wind impact on the turbine will occur in real operations when the aircraft extends the landing gear to land; this impact is useful as it accelerates the wheel thus reducing the total acceleration time.

The two-blade turbine (Model 3) has the best acceleration in the first second; that is because the blades' concave areas are facing the wind at impact for the total height of the turbine, while the other models do not have this advantage. The three-blade model (Model 1) captured only part of the wind, because when the second blade is up, the third blade is in a horizontal position, which reduces the wind flow passing through the turbine, thus reducing the efficiency.

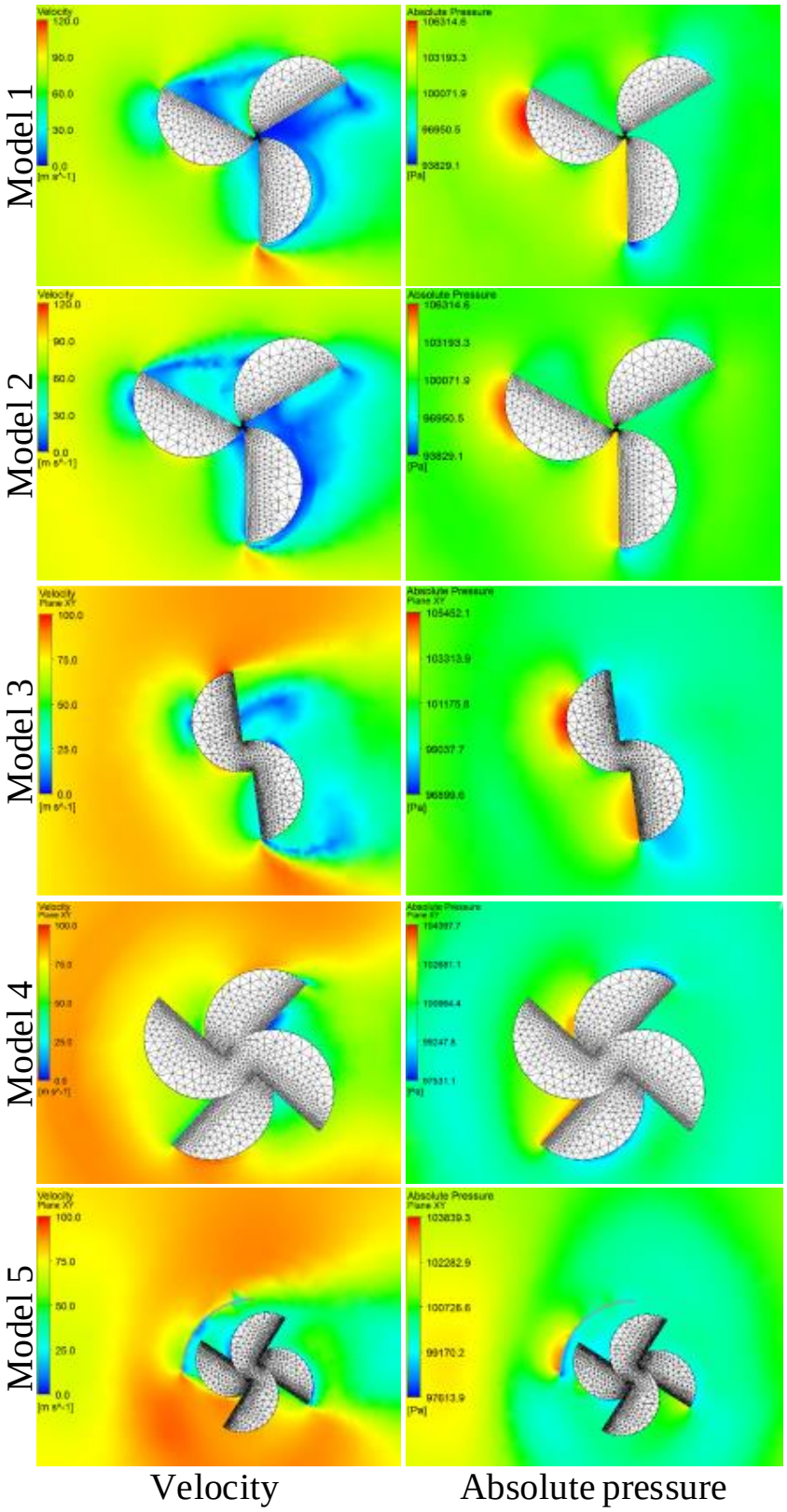

Figure 6.15 Contours of velocity and absolute pressure.

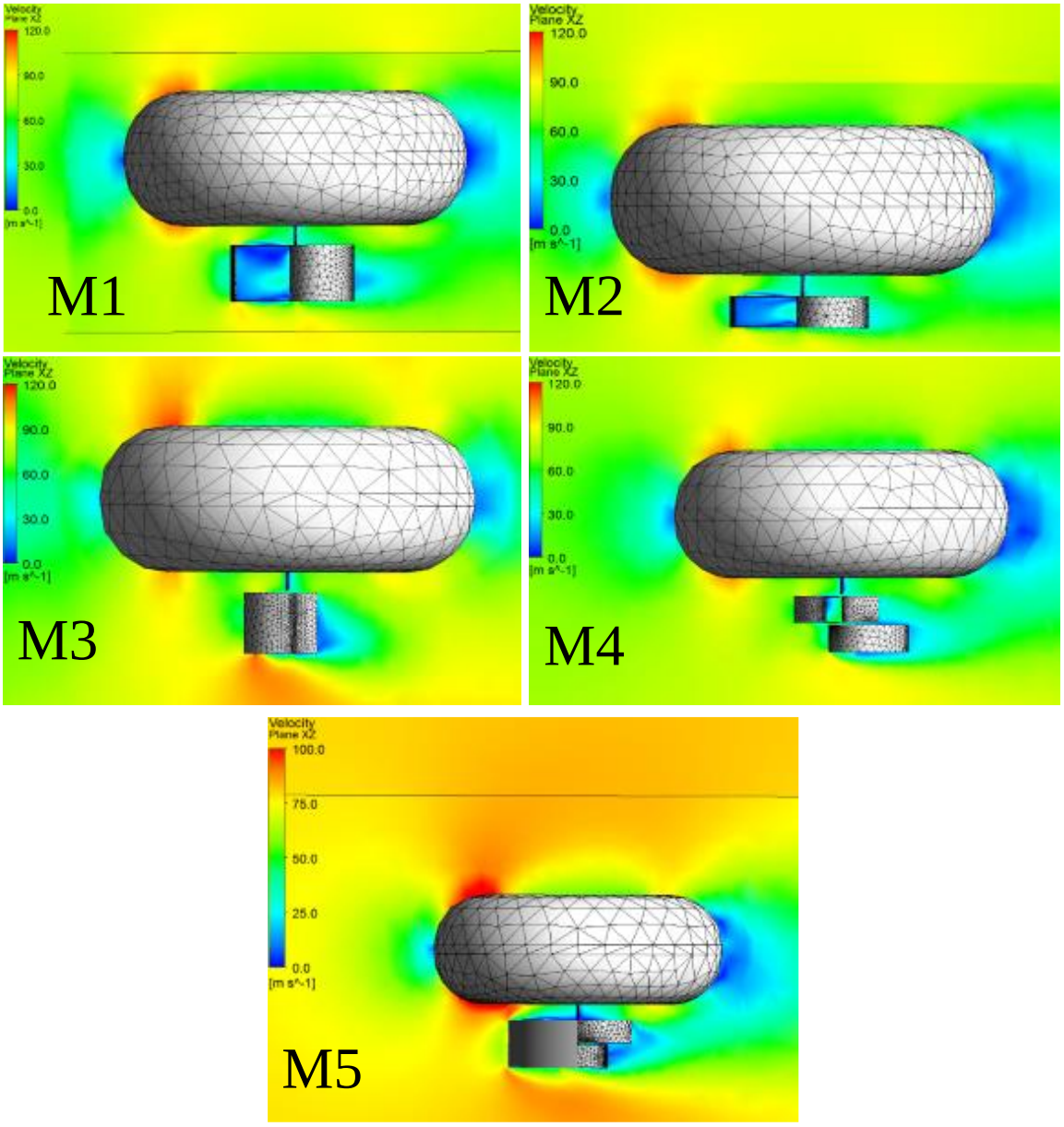

Figure 6.16 Top view of the wind velocity profile on the wheel with different turbines.

The models divided into two stages (Model 4 and Model 5) are facing the wind with half the area compared to Model 3, therefore, they have less acceleration at the moment of impact; but after sufficient time, they accelerate better than Model 3 as they produce a positive force at any rotation angle.

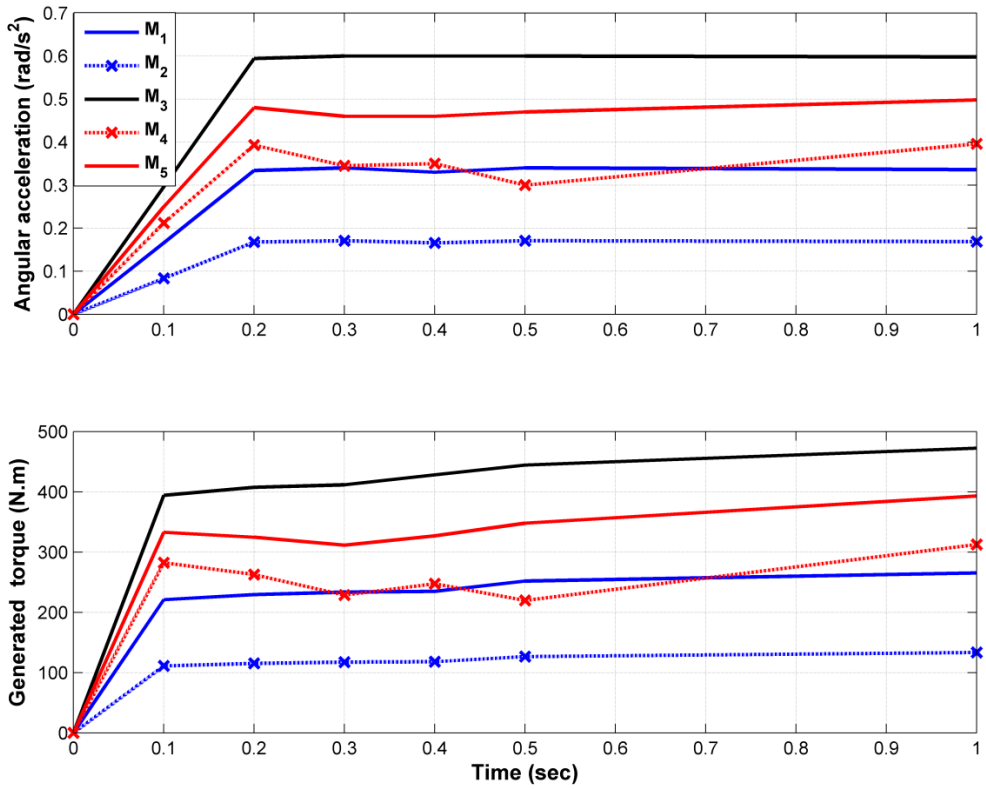

Figure 6.17 Enhancement of the turbines' generated torque and acceleration within the first second.

Figure 6.18 shows a comparison of the turbines' generated torques. The turbine with an obstacle (Model 5) has the best generated torque as the negative force is eliminated.

The torque curves show that the wheel's angular velocity doesn't reach a steady state rotation with any attached wind turbine after 45 seconds. The wheel angular velocities for different wind turbines are shown by Figure 6.19.

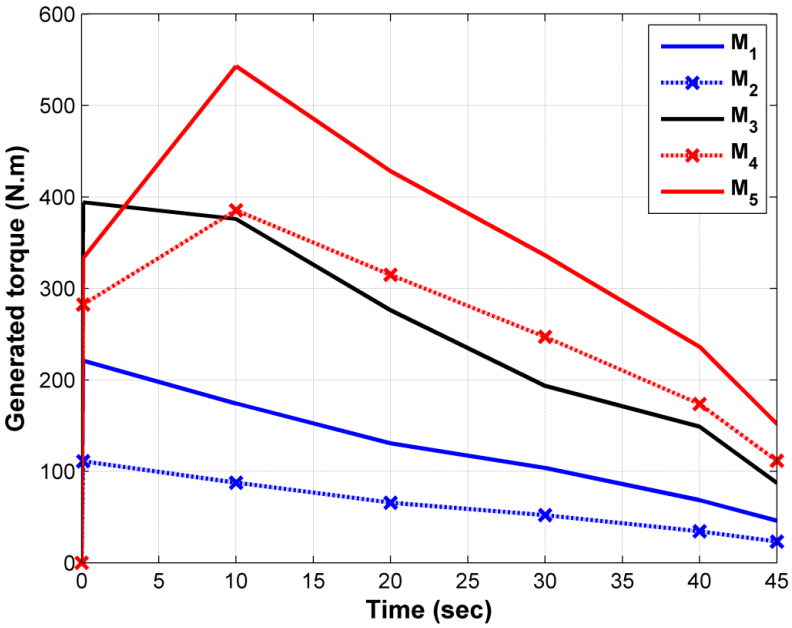

Figure 6.18 A comparison of turbines' generated torque vs. time.

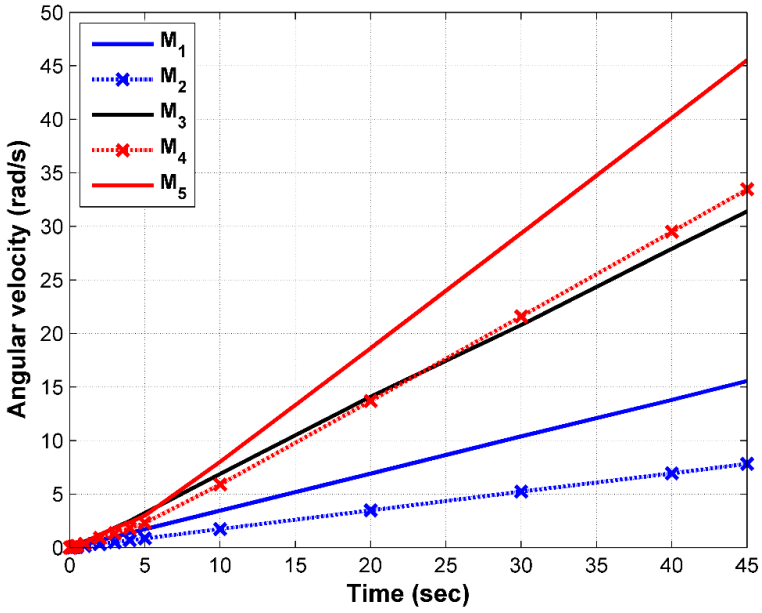

Figure 6.19 Wheel angular velocities vs. time for different wind turbine models.

In general, the angular velocities are low and none of the turbines was able to spin the wheel to the required rotation speed. This is because the wheel is heavy and the turbines' swept areas are small. However, these speeds are result of low net torque. The net torque is the result of the torque generated by the turbine minus the wheel friction torque. The net torque curves are shown by Figure 6.20.

The low values of the net torque describe the low rotation speed of the wheel. Moreover, low rotational speed leads to low turbine tip speed ratios which means low captured wind thus low power and torque coefficients, as shown by Figures 6.21 and 6.22 respectively. Figure 6.23 shows the comparison of turbines' power.

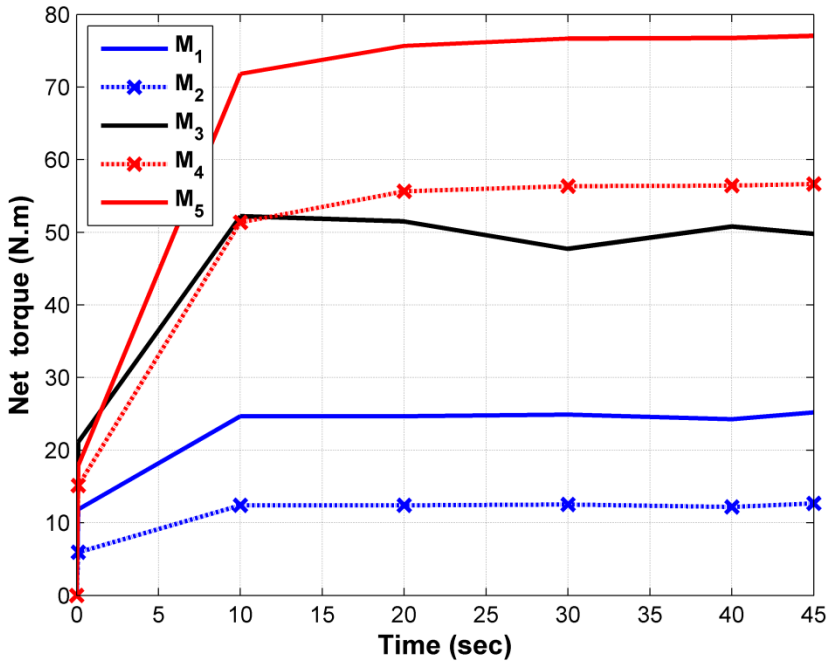

Figure 6.20 A comparison of turbine net torque vs. time.

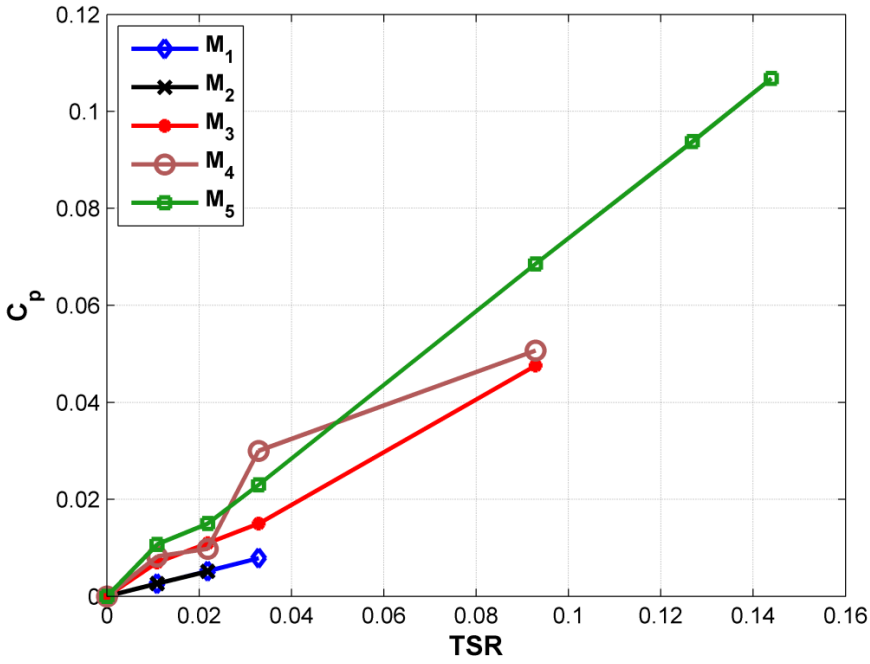

Figure 6.21 A comparison of wind turbines' power coefficients vs. tip speed ratio.

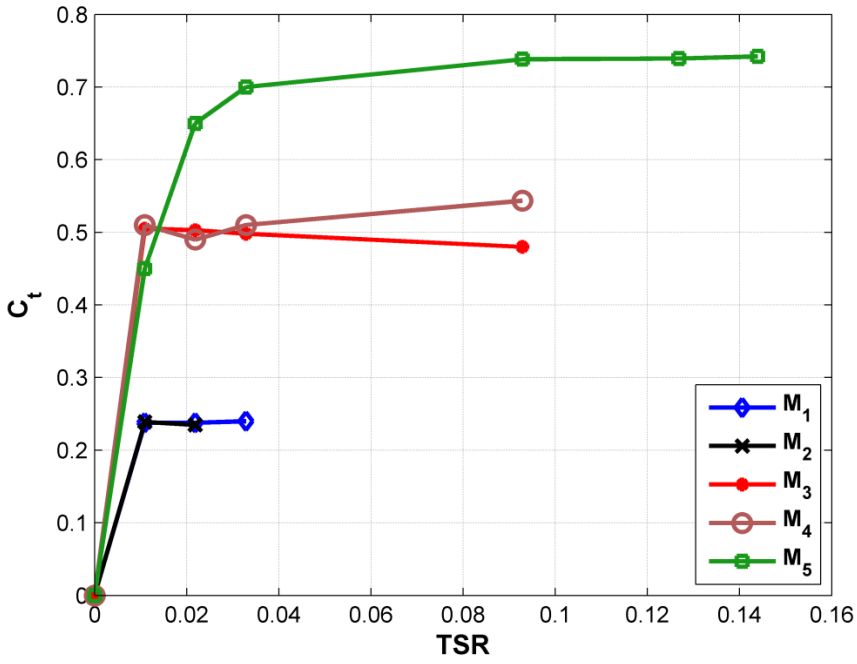

Figure 6.22 A comparison of wind turbines' torque coefficients vs. tip speed ratio.

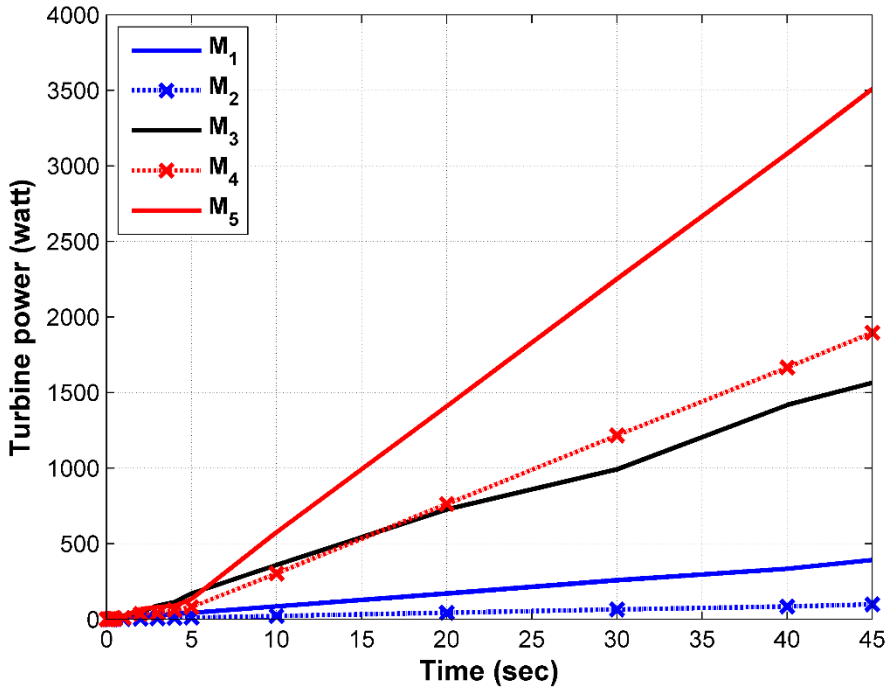

Figure 6.23 A comparison of wind turbine power vs. time.

The power and torque coefficients of Models 1 and 2 are the same, as they have the same shape, albeit with different swept areas, therefore, the same percentage of wind power is captured.

The turbine with two blades (Model 3) is more efficient than that with three blades (Model 1) by 70%. This percentage is not too far from Mahmoud et al. (2012) [74] result which was 60%. Maybe the reason is that the performance of the two blades (Model 3) is improved by the overlapping space (15%), and the difference in boundary conditions. The wheel's angular velocity in Model 1 is 49.5% that of Model 3, which is low because the power coefficient of Model 1 is low at this tip speed ratio (TSR) as the three blades decrease the amount of wind captured by the turbine.

The two-stage turbine (Model 4) has a better performance than two blades (Model 3) by18% after 45 seconds, which is higher than cited in the available literature by 10% [74]. In the first few seconds, the two blades (Model 3) start with a higher performance than the double stage model by 49% which is too high. This may result from the high wind and impact as described above. The wheel angular velocity with Model 4 is higher than Model 3 by only 7%.

Using an obstacle increased the turbine power coefficient up to 46%, which is higher than Mohamed et al. (2011) [145] results by 12%. However, the major requirement in this model is the wheel rotational speed which increased by 26% when using an obstacle.

From the Model 1 and 2 results; doubling the turbine height for the same diameter and boundary conditions will double the output; torque, power and rotational speed. Therefore, based on this outcome and the current angular velocities, the turbine height can be adjusted to reach the required rotational speed within the required time by multiplying the current height by an 'adjustment factor'. The adjustment factor is simply the number required to be multiplied by the current wheel velocity to reach the target rotational speed. Table 6.3 shows the required height for every turbine to reach the required rotational speed (60.5 rad/sec) within 45 seconds. Model 2 is omitteded from the table because it has the same shape as Model 1.

The turbine heights presented in the above table assumes that every turbine will reach the target rotation speed at this height within the required time. The best turbine with regard to size is Model 5 (two stages with an obstacle), but it is complicated to fit on the wheel. Moreover, a 26% increase in the wheel's rotational speed by adding an obstacle is not

worth the effort. Therefore, the double stage model (Model 4) is most suitable and easy to manufacture.

Table 6.3 Required heights for the turbines.

	Current wheel angular velocity (rad/sec)	Adjustment factor	Required height for the turbine (mm)
Model 1	15.56	3.88	776
Model 3	31.41	1.93	386
Model 4	33.48	1.81	362
Model 5	45.54	1.33	266

Chapter 7

7. Conclusions and Future Work

7.1. Conclusions

The purpose of this work was to study the effect of the technique of pre-spinning the wheel to eliminate aircraft landing smoke, as suggested by many patents. The available literature shows that smoke is the result of burnt tyre rubber created by the skidding wheel. When the aircraft wheel is fully sliding on the runway, this immediately increases the tyre tread temperature to a level over the critical temperature of the rubber. The heated rubber became weak, which increases the tyre wear rate. For this reason, the tyre temperature, wear and the possibility of spinning the aircraft wheel by wind power have all been investigated.

In chapter three, a single wheel of an aircraft's main landing gear has been modeled using ANSYS transient coupled structural- thermal to calculate the reduction of tyre tread temperature that can be achieved by pre-rolling the wheel before touchdown. The model shows results of the tyre tread temperature immediately after touchdown for a typical landing (where the wheel is initially static), 50% and 100% pre-rotated wheel, the sensitivity to the horizontal landing speeds and the sensitivity to sink rates.

We conclude that rotating the aircraft wheel before landing to 50% of its free rolling velocity on the runway could reduce the tyre tread temperature at touchdown to be below the rubber's critical temperature.

The angular velocity of the pre-rotated wheel decreases immediately after touchdown, but full skid is avoided and the tyre produces heat as the slip occurs, even with a fully pre-rotated wheel.

Increasing the horizontal landing speed increases the tyre tread temperature and vice versa. A hard landing increases the load on the wheel at touchdown, which leads the wheel to spin-up faster, due to a higher level of friction between the tyre and runway compared with the level for a typical landing; thus, the less the skidding distance and time, the lower the tyre tread temperature.

The model shows that the pre-spinning wheel will not increase the aircraft landing distance because even with an overshoot level, the wheel's angular velocity will not increase the aircraft's forward speed as the kinetic energy of the wheel is small compared to the aircraft body's kinetic energy. In other words, the aircraft body is towing the wheel, rather than driving with it as a car does. Moreover, the pre-spinning wheel will not affect the brake as it reaches its free rolling level before the pilot applies the brake.

However, the simulation model initially used only rotation for wheel velocity without the use of torque, as the wind turbine (or any such method) will spin the aircraft wheel at approach. Using the torque will reduce the drop in the wheel angular velocity at touchdown. In this case pre-spinning the wheel at less than 50% may avoid a high tyre tread temperature at touchdown and thus reduce landing smoke. However, the model shows the worst possibility for tyre heat, as there is no torque applied on the wheel. On other hand, it rested on certain assumptions as the runway temperature at the beginning of the simulations was set to be only 22 ˚C, while in reality this depends on the weather

conditions; dry, wet, hot or cold. In some airports, the runway temperature reaches over 50^{o}C in the summer. In this case, it may require more pre-spinning speed for the wheel.

The model in chapter four was the continuation of the chapter three to compare between the tyre wear in a typical landing and when the wheel was pre-rotated before touchdown. The wear calculation was based on the Archard theory. The tyre tread wear rate increases with a rise in the temperature as the material hardness lessens. However, the results show that tyre wear still occurred even with a 100% pre-rotated wheel, because the wheel angular velocity drops immediately after touchdown, which increases the slip thus incurred. When the wheel is initially rotated at 50% and 100% of its free-rolling; the total tyre rubber wear is reduced by 37% and 51% respectively, which could improve the tyre's life.

The hard landing records a lower tyre wear because of the lower skid time and distance travelled that occurred due to higher friction between the tyre and runway.

In chapter five, an isolated wheel has been tested using ANSYS CFX against different wind speeds. The wheel was accelerated from zero to steady state rolling in order to investigate the aerodynamic forces generated during rotation, from this the torque required to spin the wheel was then determined.

We conclude that the lift force depends on the rotation direction. In the aircraft approach condition, the lift force is negative (downwards) and is additive to the load on the wheel. Also, the shape of the tyre has the effect of increasing the drag force in the rotational axis.

In chapter six, a heavy aircraft wheel was rotated by five different wind turbines at approach speed using an ANSYS CFX simulation in order to identify the most efficient

wind turbine of acceptable size and simple design, with regard to reaching the target rotational speed. The wind turbines were loaded by the heavy wheel weight which led to a low tip speed ratio thus less power.

The first turbine had three blades and the second turbine was half its height to find the effect of decreasing or increasing the height on the turbine angular velocity. The results show that increasing or decreasing the height has the same percentage effect on the angular velocity if the same boundary conditions are applied.

The third model has two blades with an overlap ratio 15.6%. The modified two-blade model was better than that with three blades because increasing the wind turbine blades will decrease the amount of wind passing through, thus being less efficient.

Doubling the stages increased the efficiency and angular velocity slightly. Furthermore, adding an obstacle to eliminate the negative drag forces increased turbine efficiency up to 46% and increased the angular velocity of the wheel by 26%. However, the turbine models were simply to check their ability to spin aircraft wheels; and more professional wind turbines should be investigated for the same purpose.

7.2. Future Work

Only longitudinal slip was included in the case study presented in Chapters three and four. A further study could include the tyre heat and wear induced with initial lateral slip as well as longitudinal slip for cross-wind landings, although quantifying the distribution of crosswind components over a large number of landing events would be difficult. The lateral force acting on the tyre at contact with the runway in crosswind landings would be

interesting to add to the model, although it is expected that the tyre heat and wear component from this would be small.

The Archard wear theory used to compare tyre wear in Chapter four is a very simple linear approximation, and it would be advisable to compare it with other wear models to confirm the relative wear prediction from simulations between un-spun and pre-spun tyres.

The runway in this model is assumed to be dry and its temperature was set at 22 ˚C at the beginning of the simulations, therefore, it is advisable to also simulate for different runway conditions, such as wet, icy, and very hot.

In Chapter six, only simple drag turbines were investigated to spin the aircraft wheel at approach. More professional drag turbine models, that are able to produce power at a low tip speed ratio, should be specially investigated. Furthermore, the simulated wind turbines in this chapter were for the covered the wheel rim only. However, there is opportunity to use a higher diameter when considering the tyre deflection at touchdown. Increasing the turbine diameter will seriously increase the torque produced; and thus the wheel's angular velocity, as the torque arm increases.

The wind tunnel experiments should be considered for different drag turbines and it is strongly recommended that the turbines be connected to a wheel, as drag forces are created on the wheel when it rotates against the wind (as described in Chapter five).

Finally, a real landing test will be necessary before any commercial operation takes place.

References

[1] J. PADOVAN, A. KAZEMPOUR, and Y. H. KIM, “Aircraft Landing-Induced Tire Spinup”, Journal of Aircraft, Vol. 28, No. 12, 1991, pp. 849–854. doi:10.2514/3.46108.

[2] E. A. Saibel and C. Tsai, “Tire Wear by Ablation” Wear, Vol. 24, No. 2, 1973, pp. 161–176. doi:10.1016/0043-1648(73)90229-9.

[3] McCarty, J. L., “Wear and related characteristics of an aircraft tire during braking” NASA, TN D-6963, 1972.

[4] Hunter, J. R., “Simple Things Won't Save The Earth”, 1st ed., *University of Texas Press*, Texas, 1997, pp.1.

[5] H. Sakai and K. Araki, “Thermal Engineering Analysis of Rubber Vulcanization and Tread Temperatures During Severe Sliding of a Tire” Tire Science and Technology Vol. 27, No. 1, 1999, pp. 22–47. doi:10.2346/1.2135973.

[6] M. Bennett et al., “Composition of Smoke Generated by Landing Aircraft”, Environ. Sci. Technol., Vol. 45, No. 8, 2011,pp. 3533–3538. doi:10.1021/es1027585.

[7] D. F. Hays and A. L. Browne, (Eds.), “The Physics of Tire Traction”, Springer Science + Business Media, New York, 1974, pp.162-163.

[8] M. Tooley et al., “Aerospace Engineering e-Mega Reference”, 1st ed., *Elsevier: Butterworth-Heinemann*, 2009, pp.133.

[9] Beazley, R. H., U.S. Patent Application for a “Aircraft wheel spinner and control”, Publication No. US2414849 A. Washington, DC: U.S. Patent and Trademark Office. 28 Jan 1947.

[10] Abbasszadeh, M., T., and Abbasszadeh, M., U.S. Patent Application for a “Apparatus for causing an aircraft wheel to rotate”, Publication No. US20150021435 A1. Washington, DC: U.S. Patent and Trademark Office. 22 Jan 2015.

[11] Sweet, R. M., Gilleran, N., Edelson, J. S., Cox, I. W., Cox, R. T., U.S. Patent Application for a "Integrated electric motor and gear in an aircraft wheel", Publication No. US8714481 B2. Washington, DC: U.S. Patent and Trademark Office. 6 May 2014.

[12] Didey, A., U.S. Patent Application for a "Landing gear drive systems", Publication No. WO2014023939 A1. Washington, DC: U.S. Patent and Trademark Office. 13 Feb 2014.

[13] Karl, W., U.S. Patent Application for a "Free Spinning Wheel for Airplanes", Publication No. US20140048648 A1. Washington, DC: U.S. Patent and Trademark Office. 20 Feb 2014.

[14] Sami, K., and Anis, K., U.S. Patent Application for a "Apparatus for Pre-Rotating Aircraft Tires", Publication No. US20130112809 A1. Washington, DC: U.S. Patent and Trademark Office. 9 May 2013.

[15] Ushiyama, I., and Tawara, A., U.S. Patent Application for a" Driving device for wheel of airplane", Publication No. US20130256452 A1. Washington, DC: U.S. Patent and Trademark Office. 3 Oct 2013.

[16] Gooding, D., Singh, K., and Wilson, S., "Development of a Windmill Machine Pre-Rotation Device for an Aircraft Nose wheel." The Journal of the Association of Professional Engineers of Trinidad and Tobago Vol. 40, No.2, 2011, pp.49-56.

[17] W. Liu, W. Shi, and H. Ya, "Semi-Active Vibration Control of Landing Gear Using Magneto-Rhelological Dampers," SAE International Journal of Aerospace, vol. 4, No. 2, pp. 958–964, 2011. doi:10.4271/2011-01-2583.

[18] Broitzman, T., "Self-Rotating Aircraft Tire that Spins up Prior to Landing." 2009, [online database], URL: http://broit.com/idea/158/ [cited 25 25April 2014].

[19] Soderberg, R. F., U.S. Patent Application for a "Magnetically Induced Aircraft Landing Wheel Rotation." Publication No. US7594626 B2 Washington, DC: U.S. Patent and Trademark Office. 29 Sept 2009.

[20] Schmitz, R. H., U.S. Patent Application for a "Method and System to Accelerate Aircraft Wheels Before Touch-Down." Publication No. US20090182462 A1. Washington, DC: U.S. Patent and Trademark Office. 16 July 2009.

[21] Zha, G., U.S. Patent Application for a "Landing Gear Wheels with Side-Mounted Air Foils." Publication No. WO2007114803 A1. Washington, DC: U.S. Patent and Trademark Office. 11 Oct 2007.

[22] Horvath, V., and Szoke, B., U.S. Patent Application for a "Airplane tire saver by protrusion airfoils", Publication No. WO2006130944 A1. Washington, DC: U.S. Patent and Trademark Office. 14 Dec 2006.

[23] K. Yoshioka, A. Sone, A. Masuda, and H. Yamashita, "Smoothing Runway Travel to Improve Safety and Lower Maintenance Costs -A New Type of Aircraft Landing Gear Promises Safer and More Comfortable Travel-," SAE Technical Paper Series, Oct. 2005. doi:10.4271/2005-01-3416.

[24] Suzuki, T., U.S. Patent Application for a "Airplane Wheel Unit." Publication No. US6450448 B1. Washington, DC: U.S. Patent and Trademark Office. 17 Sept 2002.

[25] Lyons, D. E., U.S. Patent Application for a "Method of Rotating Aircraft Wheels." Publication No. US6499691 B1. Washington, DC: U.S. Patent and Trademark Office. 31 Dec. 2002.

[26] J. M. Opitz, Sr., U.S. Patent Application for a "Airplane Wheel Rotator." Publication No. US3866860 A. Washington, DC: U.S. Patent and Trademark Office. 18 Feb 1975.

[27] Almen, Michael D., U.S. Patent Application for a "Wheel Rotation Device." Publication No. US6390415 B1. Washington, DC: U.S. Patent and Trademark Office. 21 May 2002.

[28] Gannatal, J. P., U.S. Patent Application for a "Space Shuttle Wheel Acceleration System." Publication No. US5251848 A. Washington, DC: U.S. Patent and Trademark Office. 12 Oct 1993.

[29] I. Rosu, H. Elias-Birembaux, F. Lebon, H. Lind, and M. Wangenheim, "Experimental and Numerical Simulation of the Dynamic Frictional Contact between an Aircraft Tire Rubber and a Rough Surface," Lubricants, Vol. 4, No. 3, p. 29, 2016, doi:10.3390/lubricants4030029.

[30] Linke, T., et al., “Experimental Friction and Temperature Investigation on Aircraft Tires,” Tire Science and Technology, Vol. 42, No. 3, pp. 116-144, 2014.

[31] Y.-J. Lin and S.-J. Hwang, “Temperature prediction of rolling tires by computer simulation,” Mathematics and Computers in Simulation, Vol. 67, No. 3, pp. 235–249, 2004, doi:10.1016/j.matcom.2004.07.002.

[32] J. McAllen, A. M. Cuitiño, and V. Sernas, “Numerical investigation of the deformation characteristics and heat generation in pneumatic aircraft tires,” Finite Elements in Analysis and Design, Vol. 23, No. 2–4, pp. 241–263, 1996, doi:10.1016/s0168-874x(96)80010-2.

[33] A. W. Mair, and D. L. Birdsall, “Aircraft performance”, *Cambridge Aerospace Series 5*, 1st ed., Cambridge University Press, UK, 1992, pp.147.

[34] FAA, “Airplane Flying Handbook,” U.S Department of Transportation, Federal Aviation Administration, FAA-H-8083-3A, 2004.

[35] Van Sickle, Neil D., et al., "Van Sickle's modern airmanship," McGraw-Hill, 1999. pp. 125.

[36] Boeing 747 Landing Gear, “Flickr”, [online database], URL: https://www.flickr.com/photos/timdegroot/sets/72157627378055183/ [cited 16 Nov 2014].

[37] M. Gafvert, “Comparisons of two dynamic friction models,” Proceedings of the 1997 IEEE International Conference on Control Applications, pp. 386-391. doi:10.1109/cca.1997.627584.

[38] MICHELIN AIRCRAFT TIRE Co., “CARE AND SERVICE MANUAL,” Revision D, 15 December 2011, p. 105.

[39] Comanche Flyer Europe, “*Aircraft Tyres-Construction and Maintenance*,” 2012. [online database], URL: http://www.comancheflyer-eur.com/public/Tyres.pdf [cited 08 May 2013].

[40] Water blasting Technologies Inc., “How Often Should Runway Friction Level Testing Take Place?,” 2013. [online database], URL: https://www.copybook.com/companies/waterblasting-technologies/articles/how-often-should-runway-friction-level-testing-take-place [cited 13 Mar.2015].

[41] Dutton-Smith, J.," America's 35 Busiest Airports," [online database], URL: https://morethanroute66.com/2015/01/24/americas-35-busiest-airports-can-you-guess-number-one/ [cited 13 Mar. 2015].

[42] Smets, S., "RUBBER & PAINT MARKER REMOVAL OPERATION CONTROLLER," 21st ACI Africa Regional Assembly, Conference and Exhibition, Livingston – Zambia 27-29 August 2012.

[43] Jetting Systems Ltd., "Runway Rubber Removal in Kandahar," [online database], URL:https://www.copybook.com/companies/jetting-systems-ltd/articles/runway-rubber-removal-in-kandahar [cited 13 Mar. 2015].

[44] Morrow, T. H., "Reliability and Performance of Friction Measuring Tires and Friction Equipment Correlation," Federal Aviation Administration, Washington DC office of airport safety and standards, NASA Accession Number: ADA223694, 1990.

[45] FAA, "Measurement, Construction, and Maintenance of Skid-resistant Airport Pavement Surfaces," Advisory Circular 150/5320-12C, March 1997.

[46] Donna Miller., "Aircraft Tire Care and Maintenance," The Goodyear Tire & Rubber Company, 2004, pp. 25-26.

[47] Lahti, J., Tmi, JL. (Ed.),"Retreading Tyres: Quality, Economy and Eco-efficiency," Tyre Specialists of Finland, Eteläranta 10, 00130 Helsinki, Finland, 2012, pp. 2-3.

[48] Heerens, N.C., "Landing gear design in an automated design environment," Master of Science Thesis in Aerospace Engineering , Delft University of Technology, 2014.

[49] Iain McCreary, "The economic cost of FOD to airlines," Insight SRI Ltd. March 2008. [online database], URL: http://fod-detection.com/wp-content/uploads/2009/12/the-economic-cost-of-fod.PDF [cited 12 March 2015].

[50] Aviation Environment Federation. "Airport Planning Guide: What are an Airports Impacts?," 2008. [online database], URL: http://www.aef.org.uk/uploads/PlanningGuide2.pdf [cited 13 Mar. 2015].

[51] S. Sahrir, S. Bachok, and M. M. Osman, “Environmental and Health Impacts of Airport Infrastructure Upgrading: Kuala Lumpur International Airport 2,” Procedia - Social and Behavioral Sciences, Vol. 153, pp. 520–530, Oct. 2014. doi:10.1016/j.sbspro.2014.10.085.

[52] P. Lobo, P. D. Whitefield, and D. E. Hagen, “Measuring PM Emissions from Aircraft Auxiliary Power Units, Tires, and Brakes,” Transportation Research Board; 2013. doi:10.17226/22457.

[53] UNECE, “Particulate Matter Emissions by Tyres,” Transmitted by the expert from the Russian Federation, Informal Document GRPE-65-20, 65th GRPE, 15-18 January 2013, [online database], URL: https://www.unece.org/fileadmin/DAM/trans/doc/2013/wp29grpe/GRPE-65-20e.pdf [cited 13 March 2015].

[54] Montague, P., “Tire Dust,” Rachel´s Environment & Health Weekly, No. 439, 27 April 1995. [online database], URL: http://www.ejnet.org/rachel/rehw439.htm [cited 13 March 2015].

[55] Tekasakul, P., and Tekasakul, S., “Environmental Problems Related to Natural Rubber Production in Thailand,” Journal of Aerosol Research, Vol. 2, No. 2, pp. 122-129, 2006.

[56] W. Jawjit, C. Kroeze, and S. Rattanapan, “Greenhouse gas emissions from rubber industry in Thailand,” Journal of Cleaner Production, Vol. 18, No. 5, pp. 403–411, 2010. doi:10.1016/j.jclepro.2009.12.003.

[57] M. Bennett, S. Christie, A. Graham, and D. Raper, “Lidar Observations of Aircraft Exhaust Plumes,” Journal of Atmospheric and Oceanic Technology, Vol. 27, No. 10, pp. 1638–1651, 2010. doi:10.1175/2010jtecha1412.1.

[58] B. N. J. Persson, “Rubber Friction: Role of the Flash Temperature”, J. Phys.: Condens. Matter, Vol. 18, No. 32, 2006, pp. 7789–7823. doi:10.1088/0953-8984/18/32/025.

[59] M. T. P. van Slagmaat, “TIRE MODELS IN AIRCRAFT LANDING GEAR SIMULATION,” Vehicle System Dynamics, Vol. 21, No. sup001, pp. 108–115, 1992. doi:10.1080/00423119208970002.

[60] Besselink, I.J.M., “Shimmy of aircraft main landing gears”, PhD dissertation, Technische Universiteit Delft, Delft, 2000.

[61] P. D. Khapane, “Gear Walk Instability Studies Using Flexible Multibody Dynamics Simulation Methods in SIMPACK,” Aerospace Science and Technology, Vol. 10, No. 1, 2006, pp. 19–25. doi:10.1016/j.ast.2005.07.009.

[62] J. Padovan and P. Padovan, “Modelling Wear at Intermittently Slipping High Speed Interfaces,” Computers & Structures, Vol. 52, No. 4, 1994, pp. 795–812. doi:10.1016/0045-7949(94)90361-1.

[63] A. Kondé, I. Rosu, F. Lebon, O. Brardo, and B. Devésa, “Thermomechanical Analysis of an Aircraft Tire in Cornering Using Coupled Ale and Lagrangian Formulations,” Open Engineering, Vol. 3, No. 2, 2013, doi:10.2478/s13531-012-0049-6.

[64] J. C. Houbolt and S. Batterson, “Some landing studies pertinent to glider-reentry vehicles”, NASA, Technical Note D-448, 1960.

[65] S. K. Clark, G. H. Nybakken, and R. J. Staples, “Laboratory Experiments on Reverted Rubber Friction”, NASA, CR-1398, 1969.

[66] Nelson, V., “Wind Energy: Renewable Energy and the Environment.”, Second Edition. Boca Raton, FL: CRC Press. pp. 74-75.

[67] Savonius Turbines, [Online database] URL: http://www.reuk.co.uk/Savonius-Wind-Turbines.htm [cited 3rd November 2014]

[68] Tong, W. (ed.), “Fundamentals of Wind Energy,” *Wind Power Generation and Wind Turbine Design*. Southampton: WIT Press, 2010, pp.1-44.

[69] Dobrev, I. and Massouh, F., “Exploring the Flow around a Savonius Wind Turbine,” 16th International Symposium on Applications of Laser Techniques to Fluid Mechanics Lisbon, Portugal, 09-12 July, 2012, pp.1-9.

[70] B. D. Altan and M. Atılgan, "A study on increasing the performance of Savonius wind rotors," J Mech Sci Technol, Vol. 26, No. 5, pp. 1493–1499, 2012. doi:10.1007/s12206-012-0313-y.

[71] Dincer, I. and Zamfirescu, C., "Sustainable Energy Systems and Applications," Berlin: Springer Press. 2011, pp. 344-345.

[72] Rajbongshi, D., Dutta, S., Malakar, G., Swargiary, R., Kalita, M., and Sharma, K., "Comparison in Rotational Speed of Savonius Rotor Having Deflectors around it and Savonius Rotors Having No Deflectors," *International Journal of Applied Engineering Research,* Vol. 9 No.8, pp. 877-882, 2014.

[73] Paraschivoiu, I., "Wind Turbine Design: With Emphasis on Darrieus Concept," Montreal: Polytechnic international Presses, 2002, pp. 1-17.

[74] N. H. Mahmoud, A. A. El-Haroun, E. Wahba, and M. H. Nasef, "An experimental study on improvement of Savonius rotor performance," Alexandria Engineering Journal, Vol. 51, No. 1, pp. 19–25, 2012. doi:10.1016/j.aej.2012.07.003.

[75] Staudt, L., "Wind Power Generation and Wind Turbine Design: Design and development of small wind turbines," Southampton: WIT Press, pp.257-276, 2010.

[76] Ragheb, G.M., "Vertical Axis Wind Turbines." [online database]. URL: http://mragheb.com/NPRE%20475%20Wind%20Power%20Systems/Vertical%20Axis%20Wind%20Turbines.pdf [cited 4th November 2014].

[77] V. J. Modi and M. S. U. K. Fernando, "On the Performance of the Savonius Wind Turbine," J. Sol. Energy Eng., Vol. 111, No. 1, pp. 71-81, 1989. doi:10.1115/1.3268289.

[78] Ushiyama, I., and Nagai, H., "Optimum design configurations and performance of Savonius rotors," Wind Engineering, Vol. 12, No. 1, pp. 59–75, 1988.

[79] N. Fujisawa and F. Gotoh, "Experimental Study on the Aerodynamic Performance of a Savonius Rotor," Journal of Solar Energy Engineering, Vol. 116, No. 3, p. 148-152, 1994. doi:10.1115/1.2930074.

[80] M. NAKAJIMA, S. IIO, and T. IKEDA, “Performance of Double-step Savonius Rotor for Environmentally Friendly Hydraulic Turbine,” Journal of Fluid Science and Technology, Vol. 3, No. 3, pp. 410–419, 2008. doi:10.1299/jfst.3.410.

[81] McWilliam, M. and Johnson, D.A., “Velocity Measurement of Flow Around Model Vertical Axis Wind Turbines,” International Journal of Green Energy, Vol. 5, No. 1–2, pp. 55–68, Feb. 2008. doi:10.1080/15435070701845691.

[82] K. Morshed, M. Rahman, G. Molina, and M. Ahmed, “Wind tunnel testing and numerical simulation on aerodynamic performance of a three-bladed Savonius wind turbine,” International Journal of Energy and Environmental Engineering, Vol. 4, No. 1, Article: 18, pp. 1-14, 2013. doi:10.1186/2251-6832-4-18.

[83] N. Fujisawa, “On the torque mechanism of Savonius rotors,” Journal of Wind Engineering and Industrial Aerodynamics, Vol. 40, No. 3, pp. 277–292, 1992. doi:10.1016/0167-6105(92)90380-s.

[84] Blackwell, B.F., Sheldahl, R.E. and Feltz, L.V., “Wind Tunnel Performance Data for Two- and Three-Blade Savonius Rotors.” New Mexico: Sandia Laboratories Publications, pp. 13-33, 1977.

[85] M. H. Nasef, W. A. El-Askary, A. A. AbdEL-hamid, and H. E. Gad, “Evaluation of Savonius rotor performance: Static and dynamic studies,” Journal of Wind Engineering and Industrial Aerodynamics, Vol. 123, pp. 1–11, 2013. doi:10.1016/j.jweia.2013.09.009.

[86] T. D. Kothalawala, A. Gatto, and L. Wrobel,”Computational Investigation of the Combined Effects of Yaw, Rotation & Ground Proximity on the Aerodynamics of an Isolated Wheel,” International Journal of Mechanical, Aerospace, Industrial, Mechatronic and Manufacturing Engineering, Vol. 7, No. 9, 2013, pp. 1789-1795.

[87] Morelli, A., "Aerodynamic Actions on an Automobile Wheel," Fifth Paper at the First Symposium on Road Vehicle Aerodynamics, City University London, 1969.

[88] Abu Sadek Saifur Rahman,”Computational study on flow around a rotating short cylinder in order to study the effect of rotation on the aerodynamics of a vehicle”, Master’s Thesis, Texas Tech University, 1996.

[89] United States Air Force," Republic F-84 Thunderjet pilot's flight operating manual", Periscope Film, Los Angeles, 2007, chap.7, pp. 10-11.

[90] Jingzhe, J., "A mixed mode function – Boundary element method for very large floating structure – Water interaction systems excited by airplane landing impacts", PhD dissertation, Southampton University, Southampton, 2007.

[91] N. E. Daidzic and J. Shrestha, "Airplane Landing Performance on Contaminated Runways in Adverse Conditions", Journal of Aircraft, Vol. 45, No. 6, 2008, pp. 2131–2144. doi:10.2514/1.38056.

[92] Boeing Commercial Airplane Co., "Approach speeds for Boeing airplanes", 2011, [online database], URL: http://www.boeing.com/assets/pdf/commercial/airports/faqs/arcandapproachspeeds.pdf [cited 21 March 2015].

[93] R. Lernbeiss, "Simulation of the dynamic behavior of an aircraft landing gear during landing", Simpack User Meeting, Vienna University of Technology, 2004, URL: http://www.simpack.com/fileadmin/simpack/doc/usermeeting04/um04_tu-wien-lernb.pdf [cited 3 April 2015].

[94] Tanyolaç T., and Yasarcan H., "A soft landing model and a mass spring damper based control heuristic", Proceedings of The 29th International System Dynamics Conference, Washington, DC. 2011, URL: http://www.systemdynamics.org/conferences/2011/proceed/papers/P1119.pdf [cited 17 April 2015].

[95] A. Sinha, "Vibration of Mechanical Systems", 1st ed., *Cambridge University Press*, Cambridge, MA, 2010, pp. 25-39.

[96] A. Rao, "Realistic Simulation of a Flexible Mechanism using ANSYS Solutions", *NAFEMS World Congress*, Vancouver, Canada, May 22nd- 25th, 2007, URL: http://www.nafems.org/events/congress/2007/vendor/ [cited 21 April 2015].

[97] Benjamin. M, Dean C., and Dexter M., "An experiment study of applied ground loads in landing", NASA Report1248, 1954.

[98] R. H. Daugherty, “A study of the mechanical properties of modern radial aircraft tires”, NASA TM-212415, 2003.

[99] S. L. Lawrence, “Physics for scientists and engineers”, 1st ed., Jones *and Bartlett* Publishers, 1996, pp.272-299.

[100] H. Tomita, “Tire-Pavement Friction Coefficient”, Technical Report, Naval Civil Engineering Lab Port Hueneme, California, 1970.

[101] Y. Qiu, X. Liang, and Z. Dai, “Back stepping Dynamic Surface Control for an Anti-Skid Braking System,” Control Engineering Practice, Vol. 42, Sep. 2015, pp. 140–152. doi:10.1016/j.conengprac.2015.05.013.

[102] F. Farroni, D. Giordano, M. Russo, and F. Timpone, “TRT: Thermo Racing Tyre a Physical Model to Predict the Tyre Temperature Distribution,” Meccanica, Vol. 49, No. 3, 2013, pp. 707–723. doi:10.1007/s11012-013-9821-9.

[103] Boeing Commercial Airplane Co., “Calculating Tire Contact Area”, [online database], URL: http://www.boeing.com/assets/pdf/commercial/airports/faqs/calctirecontactarea.pdf [cited 17 Dec 2015].

[104] ANSYS® Training Manual, “Contact Technology Guide,” ANSYS Inc. Release 12.0, April 2009, pp. 86-87.

[105] Goodyear Co., “Aircraft data tire book”, The Goodyear Tire & Rubber Co., Akron, 2002, pp. 11, 33.

[106] Lufthansa Technik., “Aircraft tires: more than just rubber on steel”, [online database], URL: http://www.lufthansa-technik.com/aircraft-tires. [cited 23 Dec 2015].

[107] ANSYS® Training Manual, “Chapter 2, Nonlinear Structural”, ANSYS, Inc., 2005, [online database], URL: http://www-eng.lbl.gov/~als/FEA/ANSYS_V9_INFO/Workbench_Simulation_9.0_Nonlin/ppt/AWS90_Structural_Nonlin_Ch02_Nonlinear.ppt. [cited 11 Jan 2016].

[108] J. F. Archard, “Contact and Rubbing of Flat Surfaces,” Journal of Applied Physics, Vol. 24, No. 8, pp. 981-988, 1953. doi:10.1063/1.1721448.

[109] A. Magnée, “Modelization of damage by abrasion,” Wear, Vol. 162–164, pp. 848–855, 1993. doi:10.1016/0043-1648(93)90086-2.

[110] Hiyake, T., “Automative Design: Advanced Nonlinear Simulation”, ANSYS Advantage, ANSYS, Inc. 2015, Vol. IX, Issue 2, pp. 41-45.

[111] Z. Mané, J.-L. Loubet, C. Guerret, L. Guy, O. Sanseau, L. Odoni, L. Vanel, D. R. Long, and P. Sotta, “A new rotary tribometer to study the wear of reinforced rubber materials,” Wear, Vol. 306, No. 1–2, pp. 149–160, 2013. doi:10.1016/j.wear.2013.07.012.

[112] S. A.- Roncancio, D. F. Arias-Mateus, M. M. Gómez-Hermida, J. C. Riaño-Rojas, and E. Restrepo-Parra, “Molecular dynamics simulations of the temperature effect in the hardness on Cr and CrN films,” Applied Surface Science, Vol. 258, No. 10, pp. 4473–4477, 2012. doi:10.1016/j.apsusc.2012.01.009.

[113] M. Pottinger and T. Yager, (Eds.), “The Tire Pavement Interface,” ASTM International, 1986. doi:10.1520/stp929-eb.

[114] N. Janicijevic, “Tyre wear during braking,” Istrazivanja i projektovanja za privredu, Vol. 13, No. 3, pp. 137–140, 2015. doi:10.5937/jaes13-8700.

[115] Veen, J., “An analytical approach to dynamic irregular tyre wear,” Master’s thesis, Technische Universiteit Eindhoven, Mechanical Engineering Department, 2007.

[116] Saibel, E., & Tsai, C., “Tire wear model,” Interim Report, Issue 2, Carnegie Mellon University. New York: Clearing house, 1969.

[117] F. Braghin, F. Cheli, S. Melzi, and F. Resta, “Tyre Wear Model: Validation and Sensitivity Analysis,” Meccanica, Vol. 41, No. 2, pp. 143–156, Apr. 2006. doi:10.1007/s11012-005-1058-9.

[118] Stibler, A., Herrmann, K., and Susteric, Z., “LONG-TERM STABILITY OF RUBBER HARDNESS REFERENCE BLOCKS”, HARDMEKO, Hardness Measurements Theory and Application in Laboratories and Industries, 11-12 November, 2004, Washington, D.C.,USA.

[119] All seals Inc., “The physics of rubber,” [online database], URL: http://www.allsealsinc.com/allseals/Orings/or13.htm [cited 14 Nov 2015].

[120] Carbide Depot., “Hardness Conversion Chart,” [online database], URL: http://www.carbidedepot.com/formulas-hardness.htm [cited 14 Nov 2015].

[121] A. Houari, “Determining the drag coefficient of rotational symmetric objects falling through liquids,” European Journal of Physics, vol. 33, No. 4, pp. 947–954, 2012. doi:10.1088/0143-0807/33/4/947.

[122] J. K. Moore, "Aerodynamics of High Performance Bicycle Wheels", Master’s Thesis, University of Canterbury, 2008.

[123] NASA, “Lift of Rotating Cylinder,” [online database], URL: https://www.grc.nasa.gov/www/k-12/airplane/cyl.html [cited 02 Feb. 2016].

[124] Carstensen, S., Mandviwalla, X., Vita, L., and Paulsen, U., “Lift of a Rotating Circular Cylinder in Unsteady Flows”, Journal of Ocean and Wind Energy, Vol. 1, No. 1, 2014, pp. 41–49.

[125] Burns, John A., and Ou, Yuh-Roung, “Effect of Rotation Rate on the Force of a Rotating Cylinder: Simulation and Control” NASA Contractor Report 191442, ICASE Report No. 93-11, 1993, URL: http://ntrs.nasa.gov/search.jsp?R=19930017819 [Cited 17 April 2016].

[126] D. Zhang, A. Ivanco, and Z. Filipi, “Model-Based Estimation of Vehicle Aerodynamic Drag and Rolling Resistance,” SAE International Journal of Commercial Vehicles, Vol. 8, No. 2, pp. 433–439, 2015. doi:10.4271/2015-01-2776.

[127] Bernard J. Hamrock and William J. Anderson, “Rolling-Element Bearings,” NASA Reference Publication 1105, 1983.

[128] Huminic, A. and Huminic, G., “CFD Investigations of an Open-Wheel Race Car,” 4th European Automotive Simulation Conference (EASC2009), Munich, Germany 6-7 July 2009.

[129] K. Okumura, “CFD Simulation by Automatically Generated Tetrahedral and Prismatic Cells for Engine Intake Duct and Coolant Flow in Three Days,” SAE Technical Paper Series, Mar. 2000. doi:10.4271/2000-01-0294.

[130] F. R. Menter, “Two-equation eddy-viscosity turbulence models for engineering applications,” AIAA Journal, vol. 32, no. 8, pp. 1598–1605, 1994. doi:10.2514/3.12149.

[131] ANSYS® Academic Research, Release 15.7, Help System, CFX-Pre Guide, ANSYS, Inc.

[132] F. R. Menter, “Review of the shear-stress transport turbulence model experience from an industrial perspective,” International Journal of Computational Fluid Dynamics, Vol. 23, No. 4, pp. 305–316, 2009. doi:10.1080/10618560902773387.

[133] Wilcox, D.C., “Turbulence modeling for CFD,” 1st ed, La Canada, CA: DCW Industries Inc., 1998.

[134] Danks, R., Smeaton, W., Bigelow, B., and Burgett, W., “Initial computational fluid dynamics modeling of the Giant Magellan Telescope site and enclosure,” Proc SPIE 9911, 9911-41 (2016), doi:10.1117/12.2233288.

[135] W. Tong, “Fundamentals of wind energy,” WIT Transactions on State of the Art in Science and Engineering, pp. 3–48, Jun. 2010, doi:10.2495/978-1-84564-205-1/01.

[136] Wenehenubun, F., Saputra, A. and Sutanto, H., “An Experimental Study on the Performance of Savonius Wind Turbines Related With The Number Of Blades,” Energy Procedia, Vol. 68, pp. 297–304, 2015.doi:10.1016/j.egypro.2015.03.259.

[137] S. ERIKSSON, H. BERNHOFF, and M. LEIJON, “Evaluation of different turbine concepts for wind power,” Renewable and Sustainable Energy Reviews, Vol. 12, No. 5, pp. 1419–1434, 2008.doi:10.1016/j.rser.2006.05.017.

[138] U. K. Saha, S. Thotla, and D. Maity, “Optimum design configuration of Savonius rotor through wind tunnel experiments,” Journal of Wind Engineering and Industrial Aerodynamics, Vol. 96, No. 8–9, pp. 1359–1375, Aug. 2008. doi:10.1016/j.jweia.2008.03.005.

[139] Archinal, P., Jefferson, L., Pollin, R., and Shooter, M., "Partially Enclosed Vertical Axis Wind Turbine," Worcester Polytechnic Institute, project ID: BJS-WS14, 2014

[140] V. Reyes, J. J. Rodriguez, O. Carranza, and R. Ortega, "Review of mathematical models of both the power coefficient and the torque coefficient in wind turbines," IEEE 24th International Symposium on Industrial Electronics (ISIE), Jun. 2015. doi:10.1109/isie.2015.7281688.

[141] M. Ragheb and A. M., "Wind Turbines Theory - The Betz Equation and Optimal Rotor Tip Speed Ratio," Fundamental and Advanced Topics in Wind Power, Jun. 2011. doi:10.5772/21398.

[142] H. Glauert, "Airplane Propellers," Aerodynamic Theory, pp. 169–360, 1935. doi:10.1007/978-3-642-91487-4_3.

[143] Dhote, A. and Bankar, V., "Design, Analysis and Fabrication of Savonius Vertical Axis Wind Turbine," International Research Journal of Engineering and Technology, Vol. 2 No. 3, pp. 2048- 2054, 2015.

[144] L.F. Rus, "Experimental Study on the Increase of the Efficiency of Vertical Axis Wind Turbines by Equipping them with Concentrators," Journal of Sustainable Energy, Vol. 3, No. 1, pp.30-35, 2012.

[145] M. H. Mohamed, G. Janiga, E. Pap, and D. Thévenin, "Optimal blade shape of a modified Savonius turbine using an obstacle shielding the returning blade," Energy Conversion and Management, Vol. 52, No. 1, pp. 236–242, 2011. doi:10.1016/j.enconman.2010.06.070.

[146] ANSYS®, "Lecture 8, Non-Conformal Interfaces & Moving Zones," © 2011 ANSYS, Inc. January 19, 2012.

Appendix A

A Theoretical Model for Tyre Heat Flux Generated at Contact with the Runway

In this appendix, the heat flux generate between the aircraft tyre at contact with the runway is investigated. Considering, q_t the source term of the diffusion equation, and its function of time, the diffusion equation in the cylindrical polar coordinate is given by:

$$\frac{\partial T}{\partial t} - \frac{\alpha}{r}\frac{\partial}{\partial r}\left(r\frac{\partial T}{\partial r}\right) - \alpha\frac{\partial^2 T}{\partial y^2} - \frac{\alpha}{r^2}\frac{\partial^2 T}{\partial \theta^2} = q_t(t)$$

Figure A.1 shows the cylindrical polar coordinate system for the tyre tread contact with the runway, which is unchangeable at full skid wheel and changeable during spin-up or rotation. In spin-up case, the cold tread material is coming in, and the heated tread is going out for some time step.

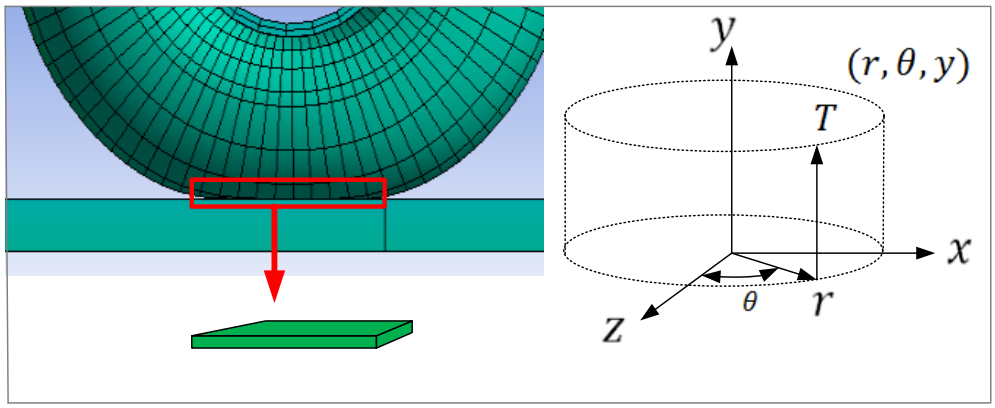

Figure A.1 Cylindrical polar coordinate system for tyre tread contact with the runway.

However, for every sub-region we assume element wise angular symmetry around every material point of the contact tread. This assumption helps us to solve the problem on a 2-D domain. The 2-D schematic representation of tread is given by Figure A.2. We let T donate the temperature inside the tread at any given point in the tread at time t.

The temperature is modeled to satisfy the diffusion equation on the 2-D schematic representation of the domain as follows: r is the radial variable in the cylindrical polar coordinates, y is the vertical space variable in the cylindrical polar coordinates, q_t is the source term, which donates the generated amount of heat that results from the work done by friction.

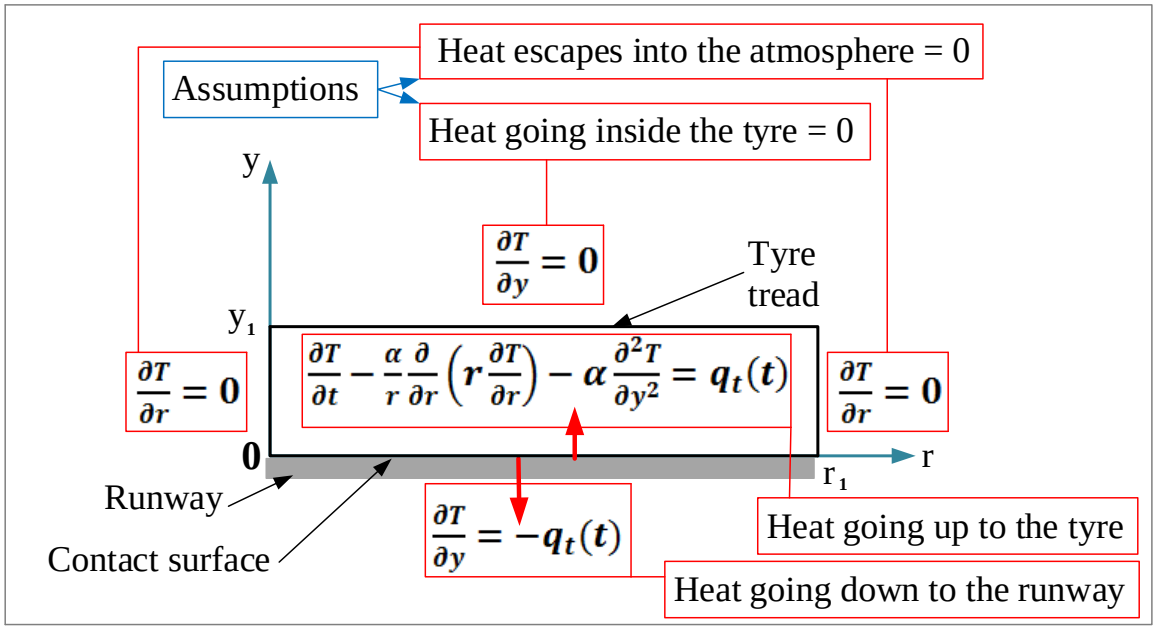

Figure A.2 2-D schematic of tread contact with the runway.

The initial condition for which we assume a certain uniform temperature at the beginning of touchdown is:

$$T(r, y, 0) = T_0(r, y) \qquad 0 < r < r_1, \qquad 0 < y < y_1$$

We use the finite element method to solve this equation. In order to compute the weak formulation, we introduce the solution and test the function spaces by: $H_E(\Omega) = \{v_t : v_t \in H^1(\Omega)$ and v_t satisfies the boundary conditions posed by the problem$\}$, and $H_{E_0}(\Omega) = \{v_t : v_t \in H^1(\Omega), v_t$ is zero on all boundaries$\}$ respectively, where $H^1(\Omega)$ is the set of all functions whose norm and the norm of its first derivative is bounded. We multiply both sides of the equation by a test function $v_t \in H_{E_0}(\Omega)$ and integrate over r and y:

$$\int_\Omega \frac{\partial T}{\partial t} v_t \, dr \, dy - \alpha \int_\Omega \left(\frac{1}{r}\frac{\partial}{\partial r}\left(r\frac{\partial T}{\partial r}\right) + \frac{\partial^2 T}{\partial y^2}\right) v_t \, r \, dr \, dy = \int_\Omega q_t \, v_t \, r \, dr \, dy$$

Using integration by parts we get:

$$\int_\Omega \frac{\partial T}{\partial t} \, v_t \, r \, dr \, dy$$

$$- \alpha \int_\Omega \left(\frac{\partial T}{\partial r}\frac{\partial v_t}{\partial r} + \frac{\partial T}{\partial y}\frac{\partial v_t}{\partial y}\right) r \, dr \, dy + \alpha \int_{\partial\Omega} v_t \, \frac{\partial T}{\partial n} \, dS$$

$$= \int_\Omega q_t \, v_t \, r \, dr \, dy$$

where, S is the stiffness and n is the outward normal vector to the boundary. The boundary term will vanish because either v_t is zero on the boundary or $\frac{\partial T}{\partial n}$ is zero, therefore we have:

$$\int_{\Omega} \frac{\partial T}{\partial t} v_t \, r \, dr \, dy - \alpha \int_{\Omega} \nabla T . \nabla v_t \; r \, dr \, dy = \int_{\Omega} q_t \, v_t \, r \, dr \, dy$$

Which can be written as:

$$\int_{\Omega} \left[\frac{\partial T}{\partial t} \, v_t - \alpha \, \nabla T . \nabla v_t - q_t \, v_t \right] r \, dr \, dy = 0$$

The weak formulation of the problem is to find $T \in H_E(\Omega)$ such that:

$$\int_{\Omega} \left[\frac{\partial T}{\partial t} v_t - \alpha \nabla T . \nabla v_t - q_t \, v_t \right] r \, dr \, dy = 0$$

For all $v_t \in H_{E_0}(\Omega)$. We define the finite element spaces by:

$V_E^h(\Omega) = \{v_h : v_h \in$

$V^h(\Omega)$ and v_h satisfies the boundary conditions posed by the problem },

$$V_{E_0}^h(\Omega) = \{v_h : \; v_h \in \; {V_E}^h(\Omega) \; and \; v_h \text{ is zero on the boundaries}\}$$

The corresponding finite element formulation is to find $v_h \in V_E^h(\Omega)$ such that

$$\int_{\Omega} \left[\frac{\partial T_h}{\partial t} \, v_h - \alpha \nabla T_h . \nabla v_h - q_t v_h \right] r \, dr \, dy = 0$$

For all $v_h \in V_{E_0}^h(\Omega)$, we express T_h and v_h in terms of linear combinations of basis functions of the finite element spaces in the form of:

$T_h = \sum_{i=1}^{N} T_i \emptyset_i$ and $v_h = \sum_{j=1}^{N} \emptyset_j$

Where, T_i is the temperature at the ith node. This will be the vector of unknowns to be computed by the resulted algebraic system. $\emptyset_i$ and $\emptyset_j$ are the basis functions, which

from $i,j=1$ to $i,j=N$ collectively span the finite element space $V_E^h(\Omega)$. Substituting the expressions for T_h and v_h in the finite element formulation we get:

$$\frac{d}{dt}\int_\Omega \sum_{i=1}^{N} T_i \emptyset_i \sum_{j=1}^{N} \emptyset_j \; r\, dr\, dy$$

$$-\alpha \int_\Omega \sum_{i=1}^{N} T_i \nabla\emptyset_i \sum_{j=1}^{N} \nabla\emptyset_j \, r\, dr\, dy - \int_\Omega \; q_t \sum_{j=1}^{N} \emptyset_j \; r\, dr\, dy = 0$$

Assuming sufficient smoothness of $\emptyset_i$ and $\emptyset_j$, we may interchange the summation with integration, so we have:

$$\sum_{i,j=1}^{N} T_i' \int_\Omega \emptyset_i \emptyset_j r\, dr\, dy - \alpha \sum_{i,j=1}^{N} T_i \int_\Omega \; \nabla\emptyset_i . \nabla\emptyset_j . r\, dr\, dy = \sum_{j=1}^{N} q_t \int_\Omega \; \emptyset_j r\, dr\, dy$$

where, T_i' is $\frac{dT_i}{dt}$. Here the time derivative only hits the coefficient because $\emptyset_i$ is not dependent on time. We may write this as a system of an algebraic equation for each time step. We use the finite difference method to step up in time, and as such, we define the following vectors and matrices:

$S =$ the stiffness matrix and its entries are defined by:

$$[S]_{i,j} = \int_\Omega \; \alpha \nabla\emptyset_i . \nabla\emptyset_j r\, dr\, dy$$

$M =$ the mass matrix and its entries are given by:

$$[M]_{i,j} = \int_\Omega \; \emptyset_i . \emptyset_j r\, dr\, dy$$

$L =$ the load vector and its column entries are given by:

$$[L]_j = \int_{\Omega} q_t \emptyset_j r \, dr \, dy$$

We use backward Euler's scheme to step up in time so we have:

$$T_i' = \frac{T_i^{m+1} - T_i^m}{\Delta t}$$

$$M \frac{T^{m+1} - T^m}{\Delta t} - ST^{m+1} = L^{m+1}$$

$$MT^{m+1} - MT^m - \Delta t S T^{m+1} = \Delta t \, L^{m+1}$$

$$(M - \Delta t S) T^{m+1} = MT^m + \Delta t \, L^{m+1}$$

This is a discrete system of N algebraic equations with N unknown for each time step. When the solution to this system is obtained for every time step, the temperature at every node in the discretized domain of the tread will be known, and one will be able to take into account the consequences of high and low temperatures in different regions within the tread material.

Appendix B

Reynolds-Averaged Navier-Stokes (RANS) Model

The RANS model allows us to simulate turbulent flow as a steady state. Figure B.1 shows a simple definition for flow velocities in the RANS model.

The flow velocity is calculated as:

$$U(\vec{x},t) = \bar{U}(\vec{x}) + u'(\vec{x})$$

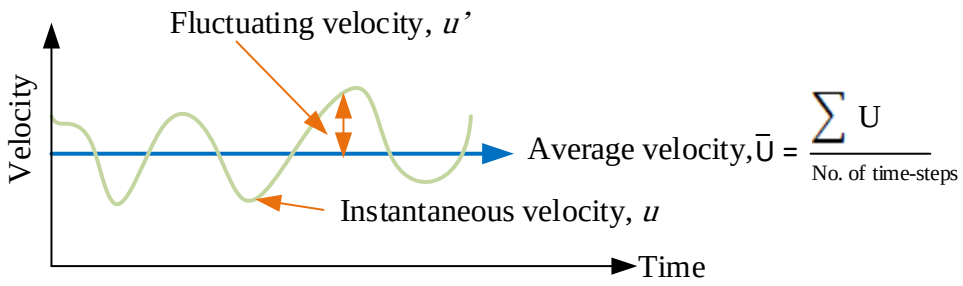

Figure B.1 Velocities definition in RANS model.

Applying the time average procedure to the governing equation which gives the Reynolds-Averaged Navier-Stokes (RANS) equations to be as:

$$\frac{\partial(\rho\overline{u_i})}{\partial t} + \frac{\partial(\overline{u_i}\,\overline{u_j})}{\partial x_j} = -\frac{\partial \bar{P}}{\partial x_i} + \frac{\partial}{\partial x_j}\left[\mu\left(\frac{\partial \overline{u_i}}{\partial x_j} + \frac{\partial \overline{u_j}}{\partial x_i} - \frac{2}{3}\delta_{ij}\frac{\partial \overline{u_m}}{\partial x_m}\right)\right] + \frac{\partial}{\partial x_j}\left(-\rho\,\overline{u_i{}'u_j{}'}\right)$$

here, $-\rho\,\overline{u_i{}'u_j{}'} = R_{ij}$ which is Reynolds stress tensor.

Shear Stress Transport (SST) model:

$$\frac{\partial(\rho k)}{\partial t}+\frac{\partial(\rho U_i k)}{\partial x_i}=\bar{P}_k-\beta^*\rho k\omega+\frac{\partial}{\partial x_i}\left[(\mu+\rho_k\mu_t)\frac{\partial k}{\partial x_i}\right]$$

$$\frac{\partial(\rho\omega)}{\partial t}+\frac{\partial(\rho U_i\omega)}{\partial x_i}=\alpha\frac{1}{v_t}\tilde{P}_k-\beta\rho\omega^2+\frac{\partial}{\partial x_i}\left[(\mu+\sigma_\omega\mu_t)\frac{\partial\omega}{\partial x_i}\right]+2(1-F_1)\rho\sigma_{\omega2}\frac{1}{\omega}\frac{\partial k}{\partial x_i}\frac{\partial\omega}{\partial x_i}$$

$$v_t=\frac{a_1 k}{\max(a_1\omega,SF_2)};\quad S=\sqrt{2S_{ij}}\,S_{ij}$$

$$P_k=\mu_t\frac{\partial U_i}{\partial x_j}(\frac{\partial U_i}{\partial x_j}+\frac{\partial U_j}{\partial x_j}),$$

$$\tilde{P}_k=\min(P_k,10.\beta^*\rho k\omega),$$

$$\mu_t=\rho\frac{k}{\omega},$$

$$F_1=tanh\left\{\left\{\min[max\left(\frac{\sqrt{k}}{\beta^*\omega Y},\frac{500v}{Y^2\omega}\right),\frac{4\rho\sigma_{\omega2}k}{CD_{k\omega}Y^2}\right\}^4\right\},$$

$$F_2=\tanh\left[\left[\max\left(\frac{2\sqrt{k}}{\beta^*wY},\frac{500v}{Y^2\omega}\right)\right]^2\right],$$

$$CD_{k\omega}=\max\left(2\rho\sigma_{\omega2}\frac{1\partial k\partial\omega}{\omega\partial x_i\partial x_i},10^{-10}\right)$$

where, k and ω are the turbulence kinetic energy and frequency respectively, Y is the distance to the wall boundary, S is the mean strain tensor rate, $F_{1,2}$ are blending function, which is equal to one. The constants are defined as: $\alpha=\alpha_1F_1+\alpha_2(1-F_1)$… etc., $\beta^*=0.09$, $\alpha_1=5/9$, $\beta_1=3/4$, $\sigma_{k1}=0.85$, $\sigma_{\omega1}=0.5$, $\alpha_2=0.44$, $\beta_2=0.0828$, $\sigma_{k2}=1$, $\sigma_{\omega2}=0.856$ [129, 130].